Design and Realization of Widely Tunable Sampled Grating Distributed Bragg Reflector Lasers for Communication and Terahertz Applications

vorgelegt von
M. Sc.
Moon-Hyeok Lee

von der Fakultät II – Mathematik und Naturwissenschaften
der Technischen Universität Berlin
zur Erlangung des akademischen Grades

Doktor der Naturwissenschaften
- Dr. rer. nat. -

genehmigte Dissertation

Promotionsausschuss:

Vorsitzende:	Prof. Dr. Ulrike Woggon
Gutachter:	Prof. Dr. Martin Schell
Gutachter:	Prof. Dr. Martijn Heck

Tag der wissenschaftlichen Aussprache: 21. Oktober 2022

Berlin 2022

Abstract

This thesis proposes novel sampled grating distributed Bragg reflector (SG DBR) lasers for communication and terahertz (THz) applications. The lasers are designed to provide a wide tuning range for increasing optical bandwidth and narrow optical linewidth for coherent applications.

For the first time, SG DBR lasers are realized based on an InP generic foundry platform. The foundry platform supports integrated optoelectronic components for customers to manufacture photonic integrated circuits (PICs). Due to the difficulty of optimizing tuning sections, it is challenging to optimize widely tunable lasers without the performance degradation of other components. The SG DBR lasers compatible with the foundry process are demonstrated to cover C band. From this work, the SG DBR is a part of a process design kit (PDK) in the foundry platform.

SG DBR lasers with an integrated ring resonator (SG DBR RR) are investigated to realize predetermined wavelength channels and improve optical linewidth. It comprises the four section SG DBR laser and the integrated ring resonator (RR), extending the cavity length to reduce the optical linewidth. Moreover, the RR provides predetermined wavelength channels, which can be used for DWDM applications. The lasers are designed with a broadband gain structure and low loss waveguides. Optimized SG DBR lasers are realized to cover a 98 nm tuning range based on the same wafer.

A novel fully integrated PIC for continuous wave (CW) THz generation is proposed, consisting of two SG DBR lasers and passive components fabricated by the foundry platform. The two SG DBR lasers offer different tuning ranges with slight overlap, the highest bandwidth obtained with any integrated tunable laser source based on InP platform. The PIC can be an important component of the CW THz system with a small footprint and volume production at a low cost.

Zusammenfassung

In dieser Arbeit werden neuartige Sampled Grating Distributed Bragg Reflector (SG DBR) Laser für Kommunikations- und Terahertz (THz)-Anwendungen vorgestellt und untersucht. Die Laser sind so konzipiert, dass sie einen großen Wellenlängen-Abstimmbereich zur Erhöhung der optischen Bandbreite und eine schmale optische Linienbreite für kohärente Anwendungen bieten.

Erstmalig werden SG DBR Laser auf der generischen InP-Foundry-Plattform realisiert. Diese Plattform bietet integrierte optoelektronische Komponenten für Kunden zur Herstellung photonisch integrierter Schaltungen (PICs). Ziel ist die Optimierung des abstimmbaren Wellenlängenbereichs ohne dass gleichzeitig die Leistung anderer Komponenten beeinträchtigt wird. Es wird gezeigt, dass die für diese Arbeit entwickelten SG DBR-Laser das vollständige C-Band abdecken. Sie sind inzwischen ein fester Bestandteil des Prozessdesign-Kits (PDK) der Foundry-Plattform.

Des weiteren werden SG DBR-Laser mit einem integrierten Ringresonator (SG DBR RR) untersucht. Die Ringstruktur als zusätzlicher Filter erlaubt eine insgesamt größere Resonatorlänge und somit eine verringerte Linienbreite. Außerdem bietet der RR vorbestimmte Wellenlängenkanäle, die für DWDM-Anwendungen genutzt werden können. Die Laser sind mit einer breitbandigen Verstärkungsstruktur und verlustarmen Wellenleitern konzipiert. Optimierte SG DBR-Laser ohne RR werden auf demselben Wafer realisiert, um einen Abstimmbereich von 98 nm abzudecken.

Es wird zudem ein neuartiger, voll integrierter PIC für die Erzeugung von THz-Wellen (CW) vorgestellt, der aus zwei SG DBR-Lasern und passiven Komponenten besteht, die auf Basis der Foundry-Plattform hergestellt werden. Die Abstimmbereiche der beiden enthaltenen SG DBR-Laser sind leicht überlappend, sodass sich eine abgedeckte Bandbreite ergibt, die auf Basis einer InP-Plattform bisher unerreicht ist. Der PIC kann eine wichtige Komponente des CW-THz-Systems sein, das eine kleine Grundfläche hat und zu geringen Kosten in Serie produziert werden kann.

Table of Contents

1. Introduction 1
   1.1. Motivation 1
   1.2. Objectives 3
   1.3. Structure of the Thesis 4
2. Fundamentals of tunable lasers 5
   2.1. Fundamental concept of tunable lasers 5
   2.2. Wavelength tuning methods 7
      2.2.1. Current injection 7
      2.2.2. Reverse voltage 9
      2.2.3. Thermal tuning 10
   2.3. Tunable DBR lasers 12
   2.4. Widely tunable lasers 15
      2.4.1. The Vernier effect 15
      2.4.2. Tunable lasers based on reflection filters 15
      2.4.3. Tunable lasers based on transmission filters 16
3. Sampled Grating DBR lasers 18
   3.1. SG DBR laser for the generic foundry platform 18
   3.2. Design and modeling 18
      3.2.1. Optical waveguide 18
      3.2.2. SG DBR 21
      3.2.3. Laser structure 23
   3.3. Experiment 28
      3.3.1. Pulsed PI measurement 29
      3.3.2. Tunable wavelength performance 29
      3.3.3. Linewidth measurement 32
4. SG DBR lasers with an integrated RR for predetermined channels 35
   4.1. Tunable lasers for prefixed wavelength channels 35

4.2. Concept of SG DBR RR lasers 36
4.3. Design and modeling 39
4.3.1. Waveguide 39
4.3.2. Waveguide transition 41
4.3.3. MMI 44
4.3.4. Ring resonator 46
4.3.5. SG DBRs and a RR 49
4.4. Experiment 50
4.4.1. Pulsed PI measurement 52
4.4.2. Wavelength tuning performance 53
4.4.3. Linewidth measurement 59
4.5. Widely tunable SG DBR laser for 98 nm tuning range 61
5. Tunable lasers for a THz PIC 65
5.1. Fundamentals 65
5.2. Design and Simulation 66
5.3. Experimental measurement 69
6. Conclusion and outlook 75
6.1. Conclusion 75
6.2. Outlook 77
7. Acknowledgments 78
8. Published work 79
9. Reference 80

1. Introduction

1.1. Motivation

Optical communication has played an essential role in the development of information and communication technology (ICT). The advancement of optical components, represented by the invention of a laser, enables exchanging data quickly and accurately by optical fibers. The impact of ICT on society is significant, from personal lifestyle to business models, because it enables users to process much information quickly and accurately.

Despite the remarkable success, optical communication is facing new demands. ICT drives to expand global internet data traffic over the decade, which has increased 15 times since 2010 with double the total number of internet users [1], [2]. Increasing use of the internet calls for more advanced optical network systems. While the data traffic is expanded, data exchange in data centers has grown, and the global data center's energy consumption accounts for 1.1% to 1.5% of worldwide electricity usage [3]. Improved optical communication for a short distance inside the data center is expected to reduce the enormous energy consumption of data centers.

To increase the amount of data in the optical network, researchers have continued to study to utilize all optical properties. Wavelength-division multiplexing (WDM) has been a highly successful technique that expands the network's capacity by using different wavelengths [4]. WDM transmits optical carriers with different data streams at different wavelengths over a single optical fiber, multiplying the system's bandwidth by the number of wavelengths. Optical bandwidths widely used are O (1260-1360 nm) and C band (1530-1565 nm), which are the areas of loss and low dispersion of the optical fiber [5]. Furthermore, dense wavelength-division multiplexing (DWDM) has offered more effective use of the vast fiber bandwidth and dimension with numerous channels separated by a nm or less [6]. In the recent past, interest in extending to L band (1565-1625 nm) has been increased [7]. The technological advances in the traditional bandwidth have expanded the data capacity. However, the increase is limited because of the fundamental limit on fiber capacity, i.e., Shannon Limit. C+L band (1530-1625 nm) is a cost-effective approach to improve the capacity because most existing fiber systems can be compatible with L band.

Coherent communication technique, which additionally uses the phase information of transmitted data, has been a promising approach to increasing the network's capacity [8]. Instead of directly using on-off intensity modulation of the light, the coherent technique extracts the phase information in the signal with a local oscillator. It is referred to as a coherent receiver represented by heterodyne and homodyne receivers. It has many advantages, such as improved signal-to-noise, increased network capacity, and polarization. Moreover, a combination with the WDM technique (i.e., so-called coherent WDM technology) is a commercialized method to maximize the advantages of the WDM and coherent technique [9]. However, the coherent technique is sensitive to phase noise from the laser source, which relates to the optical linewidth of the source. The specific linewidth requirement for coherent communication depends on the modulation format. Modern data format require values below 250 kHz [10], [11].

Laser diodes represent key components in optical communication as transmitters. The first report of a laser diode was in 1962, and double-heterostructure lasers were discovered in 1969, widely used as commercial lasers [12]. These advantages include several advantages of highly compact size, power efficiency, reliability, direct modulation, and wavelength flexibility. Tunable laser diodes have been spotlighted as a novel component for optical communications [13]. The primary role of the tunable lasers has been to replace defective single laser sources in WDM systems. Conventional WDM systems use fixed lasers, e.g., distributed feedback (DFB) lasers with different wavelengths for each channel. The replacement of defective DFB lasers with tunable lasers significantly simplifies the system's management because they can be easily switched to different wavelength channels. Furthermore, in novel optical network systems, tunable lasers are used for all channels [11]. Instead of fixed DFB lasers, the WDM includes tunable lasers set to different wavelengths. This system offers the primary advantage of flexible and sliceable channels, which means that the system can meet the required wavelengths of any channel.

For coherent WDM networks, tunable lasers with a wide tuning range and narrower linewidth are required. The tuning range exceeding 95 nm (over C + L band) is being developed and investigated currently [14]. Also, the linewidth requirement for complex modulation formats is significantly narrower, e.g., 120 kHz and 1.2 kHz for square 16 quadrature amplitude modulation (QAM) and square 64 QAM [10].

Several approaches have been investigated for C band tunable lasers on InP substrates with a wide tuning range. Most commercially available tunable lasers use the Vernier effect, using two comb-like wavelength filters. The spectral overlap of these filters selects the resulting wavelength. Examples of this approach are SG DBRs or RRs. Reference [15] shows tunable lasers with a linewidth below 100 kHz, but the tuning range is limited to the C-band. Another commercial tunable laser using superposed reflections [16] demonstrated below 200 kHz linewidth and a tuning range of 40 nm. Recently, there has been a great interest in RRs because of their long effective length, allowing for high quality (Q) factor to achieve narrow linewidth and wide tuning range. However, the relatively large loss from III-V material obstructs the realization of the high Q factor. Thus none of these lasers allows for a wide tuning range and a narrow linewidth simultaneously. For example, reference [17] demonstrated a tunable laser with double RRs, which shows 110 kHz linewidth. However, the tuning range is limited to 34 nm, not covering the C-band.

Because of an extremely low propagation loss, tunable lasers using RRs are preferred based on silicon-related materials, e.g., silicon, silicon nitride, and silicon oxide [18], [19] for wavelength selection. Using such low loss RRs tunable lasers, which cover over 100 nm tuning range with linewidths in the hundred Hz range, could be demonstrated. However, these materials have an indirect bandgap only and thus require a hybrid integration with III-V active sections as a light source. The integration brings about extra fabrication processes for a wafer bonding or butt coupling and thus increases fabrication costs. Hence, the development of tunable lasers based on the InP substrate is important for the C+L band (95 nm) with narrow optical linewidth. This thesis addresses this issue by realizing monolithically integrated SG DBR – and SG DBR RR lasers.

CW THz technology has attracted much interest for variant applications, e.g., spectroscopy, sensing, and communication [20]. Typically, two laser sources are combined to generate THz signals, and their tuning ranges determine the bandwidth. To couple the two lasers, traditional CW THz systems require the packaging of discrete optical components, resulting in poor system reliability and a large footprint. The PIC is a promising approach for the system due to the integrated optical components on a single chip. It provides a small size and volume production at a low cost also. Several publications use tunable lasers as sources for the PIC, but most lasers show limited tuning ranges below a few nm [21], [22]. Therefore, the THz bandwidth is restricted. For example, with tuning ranges of 4 nm, the THz bandwidth is 1 THz. When the PIC can use a widely tunable laser, e.g., 95 nm tuning range mentioned above, the corresponding THz bandwidth is increased to 23 THz.

1.2. Objectives

The first target of this thesis is a demonstration of SG DBR lasers and SG DBR RR lasers. This work includes optimizing, fabricating, and characterizing SG DBRs and RRs for wide tuning range and narrow linewidth simultaneously.

The second objective is an application of SG DBR lasers for a THz emitter based on the PIC. Combining the two SG DBR lasers with passive components generates THz signal is designed and tested.

1.3. Structure of the Thesis

After this introduction, chapter 2 introduces the fundamentals of tunable lasers, and chapter 3 investigates SG DBR lasers. Chapter 4 describes the SG DBR laser with integrated a RR. This chapter consists of theoretical analysis of the lasers, fabrication, and experimental results. Chapter 5 reports THz PIC, including two SG DBR lasers.

2. Fundamentals of tunable lasers

This chapter introduces a basic concept of tunable lasers and tuning methods for wavelength selectivity based on current, voltage, and thermal tuning. In order to understand the tuning concept, chapter 2.3 explains distributed Bragg reflector (DBR) lasers. Various concepts to demonstrate widely tunable lasers are described in 2.4 to overcome DBR lasers.

2.1. Fundamental concept of tunable lasers

A fundamental concept of laser consists of two mirrors facing each other and gain medium, i.e., Fabry-Perot cavity (FP) laser, is in the middle [23]. In Figure 1 (a), the gain section supports optical gain for the laser cavity, which has a width of the optical wavelength range. The bandwidth is determined mainly by the gain medium. The most commonly used gain medium in such lasers are multi quantum well structures [24]. The gain bandwidth is essential for tunable lasers because it limits the range for wavelength tuning.

Secondly, a resonance cavity is one of the prime factors of the laser. Because of the standing wave in the cavity, a discrete set of wavelengths is propagating, namely longitudinal mode (or cavity mode). The standing wave is caused by interference from two mirrors: the cavity modes are from a phase-matched in the constructive interference, and the other wavelengths are suppressed by destructive interference. More than one of the cavity modes is excited in the gain bandwidth, expressly “multi-mode” operation as shown in Figure 1 (b). However, a “single mode” operation, which uses only one mode, is preferred for various applications due to the low mode distribution noise [5].

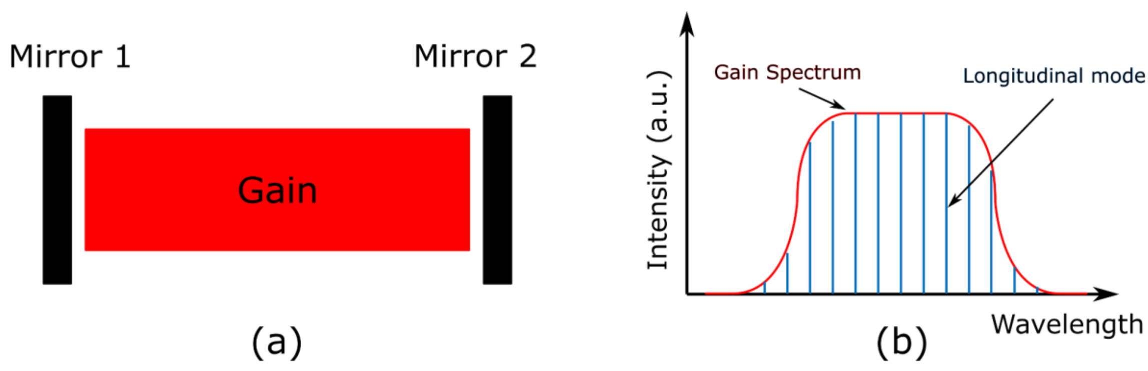

Figure 1 (a) Schematic image of FP laser, (b) Gain spectrum and longitudinal modes.

Figure 2 (a) illustrates a tunable laser structure for the "single mode" operation, including an additional tunable filter and a phase section from Figure 1 (a). The tunable filter selects a single mode from the cavity modes, which suppresses the cavity modes except for a single wavelength by the filter's narrow passband from FP's multi-mode, as shown in Figure 2 (b). For example, DBR [25] is a widely used tunable filter, combining the wavelength filter and the mirror. Narrow reflection bandwidth can leave one mode (or a few modes, but one mode has a dominant amplification) to operate single mode. Tuning of the filter can select a mode by changing the refractive index of the section. Current injection, applied reverse voltage, and thermal effect are usually used for the tunable filters, and chapter 2.2 will treat this topic. Figure 2 (c) illustrates the tuning of the filter, which selects an adjust mode from (b). Because the filter can select only discrete modes from FP, wavelengths between these modes are unselectable.

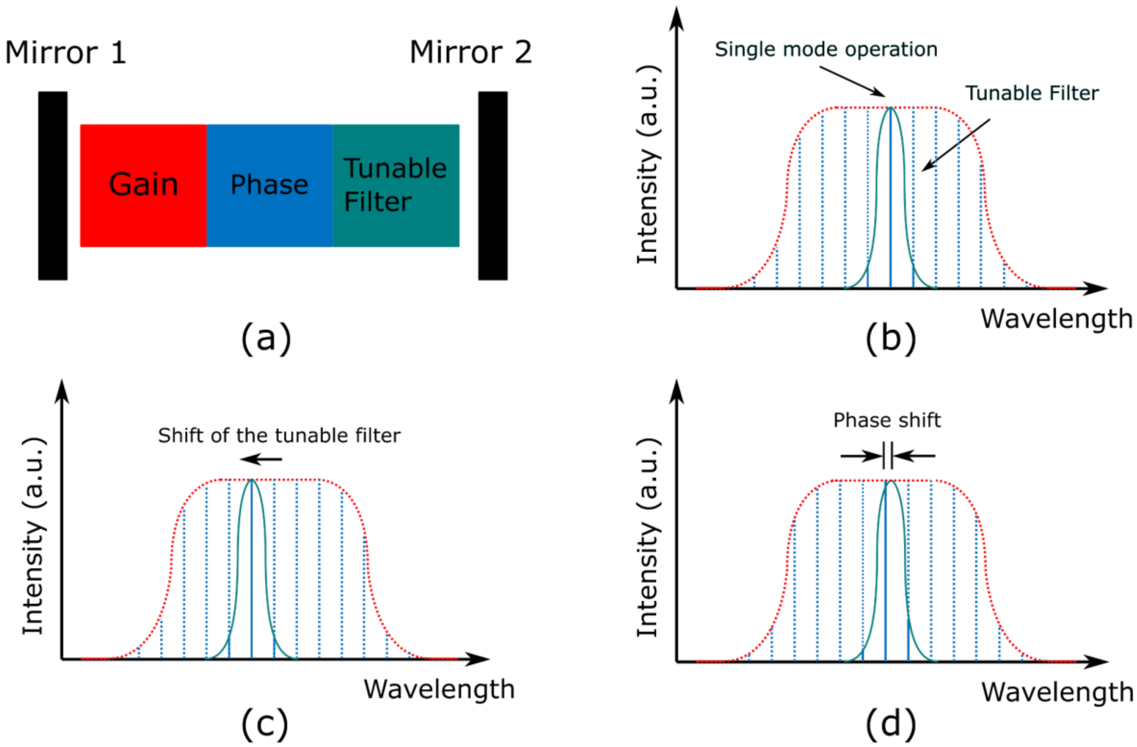

Figure 2 (a) Schematic image of the single mode tunable laser. (b) Mode selection by the tunable filter. (c) Phase section controls the cavity modes. (d) The tunable filter selects other wavelength.

The additional phase section aims to shift the cavity modes' spectral positions for wavelengths that the tunable filter cannot choose. Tuning on the phase section changes a refractive index, affecting the cavity's interference to move the constructive interference. Figure 2 (d) illustrates the shift in the phase section. Finally, all wavelengths within the gain bandwidth can be selected by tuning both the tunable filter and the phase. If the single mode has a narrow bandwidth, operated light is a single wavelength (or includes minimal bandwidth). Therefore, mode selection by the tunable filter means tuning the wavelength by controlling both the phase, and the filter for selecting continuous wavelengths in the tuning range, as seen in [25].

2.2. Wavelength tuning methods

Standard tuning methods to control tunable lasers are carrier injection (free carrier absorption), applied reverse voltage (quantum-confined Stark effect, QCSE), and thermal tuning by changing the refractive index. Following chapers are based on an investigation from Buus et al. [26], which compared three mechanisms concerning performance and limitations.

2.2.1. Current injection

Most laser diodes use multilayer structures with p-i-n junctions to use forward – or reverse bias on waveguides. The waveguide comprises layers, usually a quaternary InGaAsP layer in the middle and InP surrounding it, to obtain a propagating mode [27], [28]. Structural parameters and doping density of the multilayers determine the effective index of the propagation. When the forward bias is applied to the waveguide, it increases carrier concentration, which changes the refractive index. Physical aspects behind the changes are free-carrier absorption, band filling, and bandgap shrinkage. For InP and InGaAsP, Bennet [29] proposed models of the current effect from the theory, and Weber [30] investigated the change in the index from practical waveguides and DBRs.

The intraband transition of a free carrier, which absorbs a photon, is a function of the square of the wavelength and the concentration of electrons and holes. This free carrier absorption is also known as the plasma effect. The corresponding variation of the refractive index is given by

$$\Delta n = -\left(\frac{e^2\lambda^2}{8\pi^2 c^2 \epsilon_0 n}\right)\left(\frac{N}{m_e} + \frac{P}{m_h}\right), \tag{2-1}$$

where N and P denote the carrier density of the holes and the electrons respectively, and m_e and m_h mean the effective masses of the holes and the electrons. λ and n indicate a photon's wavelength and the refractive index, c is the speed of light, and ϵ_0 is the permittivity of free space.

The band filling and the bandgap shrinkage are explained by the interband transition between the valence and the conduction band, while the free carrier absorption is by the intraband transition. If a parabolic energy band is considered in a direct bandgap semiconductor, Equation (2) explains the optical absorption around the bandgap without current injection.

$$\alpha_0(E) = \frac{C}{E}\sqrt{E - E_g}, \qquad E \geq E_g,$$
$$\alpha_0(E) = 0, \qquad E < E_g. \tag{2-2}$$

E and E_g denote the photon energy and the bandgap energy, respectively. C is an absorption constant related to the material of the semiconductor, e.g., InGaAsP. Injected current provides carriers of electrons and holes, which occupy energy levels in valence and conduction bands. The interband transition occurs when the photon energy is matched to the energy gap from the valence band energy (E_v) to the conduction band energy (E_c). Therefore, equation (2-2) can be modified with the occupation probability of the energy states as

$$\alpha(E) = \alpha_0[(f_v(E_v) - f_c(E_c)], \qquad E \geq E_g,$$
$$\alpha_0(E) = 0, \qquad E < E_g, \tag{2-3}$$

f_v and f_c are given by the Fermi-Dirac distribution, which is a function of Fermi levels in the valence and conduction bands (E_{Fv} and E_{Fc}).

$$f_c(E_c) = \frac{1}{1 + e^{(\frac{E - E_{Fc}}{kT})}}, \quad f_v(E_c) = \frac{1}{1 + e^{(\frac{E - E_{Fv}}{kT})}}. \tag{2-4}$$

The bandgap shrinkage is an effect of repelling each carrier, e.g., electrons to electrons or holes to holes, due to the Coulomb force. Moreover, for statistical reasons, electrons with the same spin will avoid each other. The result is a screening of electrons and reduced energy from the repelling, which causes a lower conduction band edge. The modified bandgap energy from the effect is given by

$$\Delta E_g = -\frac{e}{2\pi\epsilon_0\epsilon}\left(\frac{3N}{\pi}\right)^{\frac{1}{3}}, \tag{2-5}$$

where ϵ indicates the relative static dielectric constant of the semiconductor.

The difference absorption between with and without current injection can be defined from the band filling and the band shrinkage as $\Delta\alpha(E) = \alpha(E) - \alpha_0(E)$. Finally, the change in the index is calculated over the whole wavelengths, derived from the Kramers-Kronig relation.

$$\Delta n(E_0) = \frac{2c\hbar}{e^2} P \int_0^\infty \frac{\Delta\alpha(E)}{E^2 - E_0^2} dE, \tag{2-6}$$

P denotes principal value of the integral, and E_0 is the operating energy.

A sum of the three effects causes the change in the refractive index, and the value Δn is negative. A typical value Δn from an experiment of the tuning is -0.04 at 1550 nm, which results in around 8 nm tuning by a tunable laser based on DBR structure [26]. Generated heat from the injected current limits the tuning range because a wavelength tuning by thermal effect has a positive Δn [30]. One of the main demerits is a considerable loss from the carriers. The index's variation is based on the difference in absorptions. Thus loss is high when the variation is enlarged.

2.2.2. Reverse voltage

The QCSE (Quantum Confined Stark Effect) is a field effect that changes the bandgap energy in multi-quantum wells by reversely biasing a p-n (or p-i-n) junction. Reference [31] first demonstrated the QCSE effect experimentally in 1984 and theoretically described this effect [32] in the same year. The band edges are tilted by the applied electric field with a reverse voltage, which modifies electron and hole wave functions. For electrons, the effect tends to move to the lower energy for position inside the well, whereas holes to the opposite way. Therefore, the valence and conduction band (effective bandgap energy) is slightly reduced. The energy variation leads to the photon's absorption, and thus changing the refractive index.

In contrast to the free carrier absorption, there is no current flow except the photon current, which means heat generation has not occurred. Moreover, tuning speed is much faster than the free carrier absorption because this is free from carrier lifetime limitation. However, the slight index variation requires long filters with low propagation losses. The absorption and the index variation are a function of a difference between the photon energy and the bandgap energy, as shown in equation (2-6). When the photon energy is close to the bandgap energy, the index variation is enlarged, but the absorption is also increased. High absorption during the wavelength tuning negatively influences the laser performance for tunable lasers, e.g., large threshold current and broad optical linewidth. The bandgap energy of the waveguide layer is typically larger than the photon energy to avoid absorption, and thus the refractive index changes are order 10^{-3} to 10^{-2}. Due to the small index variation, tunable lasers using QCSE generally have long filters to maximize the minor index changes by a phase accumulation, e.g., Mach-Zehnder interferometers (MZI) and RRs. The extended filter length increases the area of the entire laser and requires the low loss waveguide to reduce the cavity loss.

2.2.3. Thermal tuning

Additional heater structures on the top of waveguides or at the sides are widely used to change the temperature locally. Semiconductor materials have a temperature dependency on their refractive index [33]. To calculate the dependence, the empirical Sellmeier equation, the single oscillator model, and the Adachi model have been widely used [30], [34], [35]. Reference [35] proposed a model including temperature directly based on the modified single oscillator model, in contrast to [30], [34].

The modified single oscillator model is derived from a semi-empirical method for estimating the refractive index at the room temperature, focusing on InP-based alloys of the InGaAsP crystal [36], [37]:

$$n^2 = 1 + \frac{E_d}{E_0} + \frac{E_d}{E_0^3}E^2 + \frac{\eta}{\pi}E^4 ln\left(\frac{2E_0 - E_g^2 - E^2}{E_g^2 - E^2}\right), \tag{2-7}$$

where

$$\eta = \frac{\pi E_d}{2E_0^3(E_0^2 - E_g^2)}, \tag{2-8}$$

E_0 denotes the single-effective oscillator's energy in the absorption region, and E_g is the bandgap energy. E_d represents the dispersion energy of interband optical transitions, a combination of parameters of E_0 and the electric-dipole oscillator strength [38]. The three energy parameters are described by experimental data with an interpolation method, which is a function of the composition y in the quaternary material.

$$\begin{aligned} E_0(y) &= 3.391 - 1.652y + 0.863y^2 - 0.123y^3, \\ E_d(y) &= 28.91 - 9.278y + 5.626y^2, \\ E_g(y) &= 1.35 - 0.72y + 0.12y^2, \end{aligned} \tag{2-9}$$

under the temperature variation, (2-7) is expanded to take into account the modified Fermi distribution as a function of temperature, which is given by

$$E_g(T, y) = \left(1.421 - \frac{\alpha T^2}{T + \beta}\right) - 0.72y + 0.12y^2, \tag{2-10}$$

where α and β are fitting coefficients of the InP's energy bandgap, which results in 7.2 x 10^{-4} and 611, respectively. Figure 3 shows the refractive index dependence on temperature for different values y. Selected y values of 0, 0.262, and 0.613 represent InP, photoluminescence (PL) peak at 1.06 µm and 1.3 µm (Q1.06 and Q1.3). The figure shows that the thermal effect on the InGaAsP material increases the refractive index, and the direction is opposite to the free carrier absorption and the QCSE.

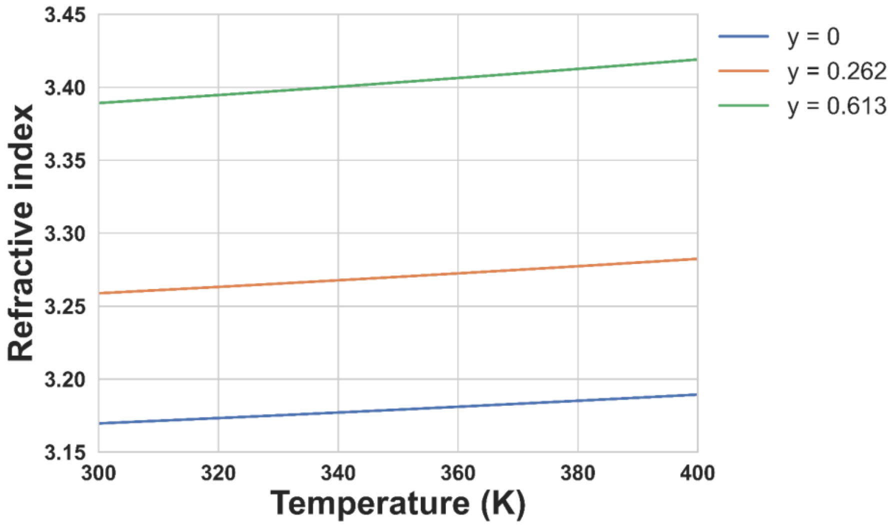

Figure 3 Calculated refractive indexes with variant y values depends on temperatures from equation (2-7) and (2-10).

Table 1 Overview of the physical mechanism for tunable lasers

	Free Carrier Absorption	QCSE	Thermal Tuning
Tuning range	-8 nm	-1 nm	+5 nm
Tuning speed (f_{3dB})	100 MHz	> 10GHz	< 1MHz
Heat generation	Middle	Negligible	Large
Loss	Large	Low	Low

The tuning value of a single mode laser is known as 0.1 nm/K for DFB and DBR lasers [39], and typical tuning range below 6 nm from 20 to 80°C. DBR lasers comprise a separated filter and a gain section, which leads to less thermal crosstalk between the gain and the filter sections. By placing the tuning section at a distance from the gain section, a tuning range of 15 nm can be demonstrated to minimize thermal crosstalk between the two sections. On the other hand, this tuning speed is relatively slow compared with the free carrier absorption and the QCSE because the thermal effect requires time to reach a stable condition.

Table 1 organizes comparison of the three physical mechanisms based on [26].

2.3. Tunable DBR lasers

The earlier work on tunable lasers was focused on the current injection with DBR in the 1980s. [40] A fundamental concept of a three-section DBR laser consists of gain, phase and DBR shown in Figure 4 (a). Injected current changes the refractive index of semiconductor materials, applying to the phase and the DBR section. As discussed in 2.2, the modified index causes a wavelength shift of the DBR's reflection spectrum and cavity modes from a cavity.

The gain section includes InGaAsP multi-quantum wells (MQWs), and the DBR section has a tunable reflection from periodic gratings. The phase section is the same waveguide design as the DBR but without gratings, tuned to control phase in the laser's cavity. A layer stack comprises a substrate of n doped InP, quaternary alloy of InGaAsP, MQWs for gain section, and p-doped InP. At the end of the device, coatings control reflection from the device to air. Usually, anti-reflection (AR) coating is used for the rear section and a few percentage reflections for the front. P-contacts are deposited on the top of the p-InP, and n-contact is formed on the bottom of the laser as a common ground.

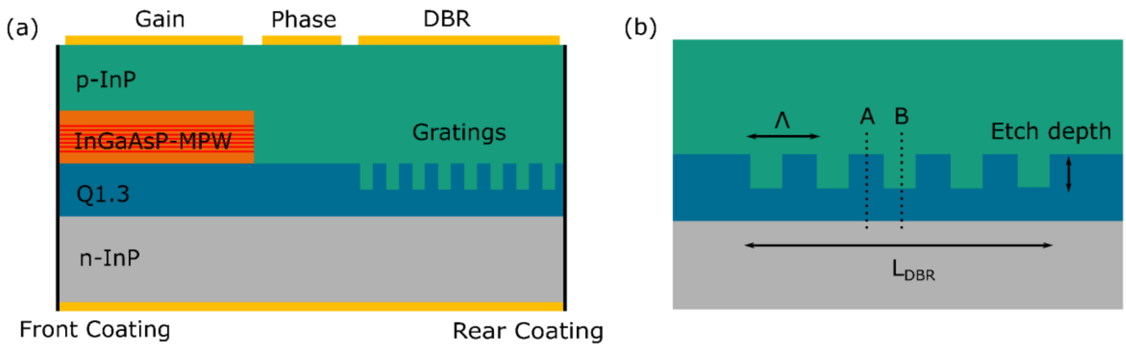

Figure 4 (a) Schematic image of three-section a DBR laser. (b) Detail parameters of the grating structure.

Figure 4 (b) illustrates the parameters of the DBR section, where Λ indicates a period of the gratings, A and B show areas with and without etched waveguide. L_{DBR} is the grating length, and the etch depth is also explained. Bragg condition is defined with the Bragg wavelength (λ_B) and the effective index (n_{eff}) of the waveguide from the grating parameters as

$$\Lambda = \frac{\lambda_B}{2n_{eff}}. \tag{2-11}$$

n_{eff} is determined by the design parameters of the waveguide and the grating structure. Etch depth of the gratings is 15 nm into the Q1.3 layer. Simulated n_{eff} are 3.211 and 3.207 for an etched and an un-etched area (A and B in Figure 4 (b)). Λ for λ_B of 1.55 µm is 241.5

nm. With L_{DBR} = 300 μm, the transfer matrix method (TMM) calculates the reflection spectrum of the DBR section, as shown in Figure 5. A coupling coefficient κ is used to define the grating reflectivity, having a unit of cm^{-1} for the reflectivity per unit length. κ is related to the ratio between n_{eff} (Δn_{eff}) and the wavelength given by

$$\kappa = \frac{2\Delta n_{eff}}{\lambda}. \tag{2-12}$$

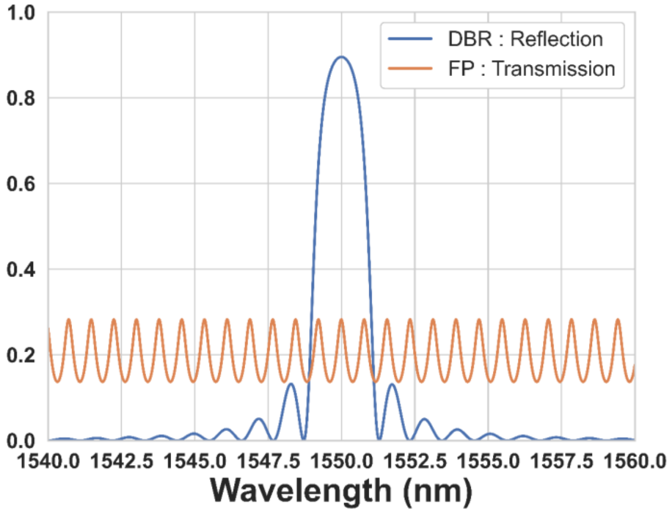

Figure 5 Reflection spectrum of DBR section and transmission spectrum of the DBR laser's cavity

As discussed in 2.1, the cavity mode in the cavity determines the single mode operation with the DBR reflection. The cavity effect from FP, which is a simple two-mirror structure with the front coating and the DBR, shows transmission with separated peaks of a free spectral range (FSR), which is given by

$$\mathrm{FSR} = \frac{\lambda^2}{2n_g L_{cavity}} \tag{2-13}$$

where n_g denotes the group index of the cavity, and L_{cavity} represents the cavity length, which consists of lengths of each section: gain (L_{gain}), phase (L_{phase}) and effective DBR length (L_{eff}). To consider the effective penetration in the DBR, the length of DBR must be replace by L_{eff}, which is a function of the L_{DBR} and the strength of the reflection as

$$L_{eff} = \frac{1}{2\kappa}\tanh(\kappa L_{DBR}). \tag{2-14}$$

In Figure 5, FP's transmission spectrum represents cavity modes of the laser cavity. The simulation uses parameters of the gain length = 300 μm, the phase length = 40 μm, front coating = 20%. The tuning range of the laser (Δλ) is limited by a wavelength shift of Bragg wavelength ($\Delta\lambda_{Bragg}$) and a cavity mode ($\Delta\lambda_{FP}$). From the equation (2-11), $\Delta\lambda_{Bragg}$ is determined by [30], as

$$\frac{\Delta\lambda_{Bragg}}{\lambda} = \frac{\Delta n_{eff}}{n_{eff}}. \tag{2-15}$$

When the waveguide's dispersion is considered, it is given more precise approximation, displacing n_{eff} to n_g by,

$$\frac{\Delta\lambda_{Bragg}}{\lambda} = \frac{\Delta n_{eff}}{n_g}. \tag{2-16}$$

The phase condition of the cavity matches the FP's standing wave, which represents the integer multiple of the wavelength is equal to the length of the cavity as

$$2\left(n_{eff,gain}L_{gain} + n_{eff,phase}L_{phase} + n_{eff}L_{eff}\right) = \ m\lambda, m\ is\ integer \tag{2-17}$$

$n_{eff,gain}$ and $n_{eff,phase}$ indicate the effective index of the gain section and the phase section. Tuning on the phase section changes the $n_{eff,phase}$, which shifts the cavity mode of the FP [13].

$$\frac{\Delta\lambda_{FP}}{\lambda_{center}} = \frac{\Delta n_{eff,phase}L_{phase}}{n_{g,gain}L_{gain} + n_{g,phase}L_{phase} + n_{g,DBR}L_{eff}} \tag{2-18}$$

$n_{g,gain}$, $n_{g,phase}$ and $n_{g,DBR}$ represent the group index of the sections, and λ_{center} indicates the center of the wavelengths. Tuning the DBR shifts the wavelength among the cavity modes, and phase tuning allows for a wavelength fine tuning. For the WDM application, the emission wavelength can be aligned to the target channels in the WDM system. The reported maximum tuning range based on the current injection and the thermal tuning is over 10 nm [41], [42], and a combination of both is 20 nm [43]. However, the tuning range is insufficient to cover the full C-band. One option is operating several lasers with smaller tuning ranges in parallel, but this causes extra costs and requires a complex control. In the next chapter, several approaches are introduced to overcome the limited tuning range beyond DBR lasers.

2.4. Widely tunable lasers

Several approaches have been investigated with multi-filters to overcome the limited tuning range from (2-15). This chapter introduces widely tunable lasers based on the Vernier effect, representing reflection and transmission type filters.

2.4.1. The Vernier effect

A vernier scale, e.g., a vernier caliper, is a tool to measure distance with relatively high resolution compared to typical scales. It uses two linear scales with different marks, and the user reads the length using the mark where the two points are coincident. Similarly, comb-like filters can select wavelengths by shifting the position of the filter's spectrum to generate a single coincidence for tunable single mode lasers.

2.4.2. Tunable lasers based on reflection filters

The widely used reflector for the Vernier effect is SGs, consisting of repeated waveguides and gratings. The cavity effect from the repeated sections leads to the comb-like reflection spectra. SG DBR laser using SGs consists of four sections: front SG DBR, gain, phase, and rear SG DBR. The structure is similar to the three-section DBR laser in chapter 2.3, where the front coating is replaced by the front SG DBR and the typical DBR by the rear SG DBR. By using the Vernier effect, tuning on the SG DBRs selects wavelengths with tuning methods from chapter 2.2. Since the SG DBR laser was proposed in 1993 [44], commercial lasers [11], [15] cover the full C band with below linewidth 100 kHz. The detail of the SG DBR laser will be introduced in chapter 3.

Super-structure grating (SSG) is a reflector, including repeated gratings with varied periods [45]. Optimized SSG with phase modulations can produce a square envelope of the reflection spectrum [46]. Because SG has an envelope of reduced reflections away from the center of the wavelength, SSG can select wavelengths without unwanted coincidence. However, optimization of the envelope by the phase variation requires complex mathematical calculations. SSG DBR lasers offer a tuning range of 40 nm, but the optical linewidth is limited to 400 kHz [46].

In contrast to SG and SSG DBR lasers, other methods have been investigated to use the sum of comb-like reflections. Y-laser comprises Y-coupler with two SG or SSG to use the Vernier effect. The final reflection spectrum after Y-coupler is calculated by the sum of two mirrors. The design has the main advantage of using a cleaved facet as an output port instead of DBR with higher propagation losses. Y-lasers report over the 35 nm tuning range, but measured linewidth is not released [47], [48].

Digital supermode (DS) -DBR laser uses a front SSG and eight separated tunable DBRs with different Bragg wavelengths. By tuning on one of the DBRs, another reflection of the different Bragg wavelength can be superposed to select the laser's wavelength. This concept has a significant advantage to simple control over other lasers based on the Vernier effect, despite many electro pads for the DBRs. Reference [16] demonstrated the wavelength tuning range over C band and below 200 kHz linewidth.

Moreover, codirectional coupled sampled grating reflector laser includes a vertical coupler to select wavelengths [49], and tunable twin guide laser has been proposed with separated layers of tuning and active sections [50]. However, none of the concepts have been satisfied the 100 nm tuning range with below 200 kHz linewidth.

Coupled cavity lasers (CCLs) consist of two coupled Fabry-Perot cavities with a reflective interferometer to use the Vernier effect [51]–[53]. These lasers have the advantage of a simple fabrication process without electron-beam lithography to realize gratings. However, the tuning range is limited in C band due to the tuning on the gain section, which is worse than the tuning on passive tuning filters. Furthermore, the long length of the gain section broadens the optical linewidth, and thus an additional self-injection method is required to demonstrate the narrow linewidth [52].

2.4.3. Tunable lasers based on transmission filters

Reference [54] demonstrates a tunable laser with three asymmetric MZIs with comb-like transmission spectra in a long ring cavity. A wavelength selection uses the Vernier effect by filtering many modes in the cavity to operate a single mode operation. The performance of the laser shows 74.3 nm tuning range with 363 kHz optical linewidth but suffers from a large footprint of 3.65 x 0.9 mm^2.

RR is a filter based on a looped waveguide with coupled waveguides, which generates periodic transmission from the constructive and destructive interference in the resonance [55]. For RR laser, multiple RRs are usually used to form a reflector due to the comb-like transmission in contrast to the comb-like reflection of SG or SSG. RRs have the benefit from a long effective filter length with a lower coupling coefficient. The long effective length reduces the laser's linewidth [56]. Furthermore, the high Q factor of the transmission spectrum compresses repeated coincidences in the Vernier effect, causing a broad tuning range [57]. However, the advantages mentioned above are working only with low loss waveguides.

RR lasers based on III-V material, e.g., InGaAsP and InP, have been investigated, but they do not perform better than DBR type of lasers. Reference [58] demonstrates a double RR tunable laser based on III-V monolithic process. RRs are designed as DBR type tunable lasers, including slightly different FSRs to select wavelength by the Vernier effect. This concept does not need any gratings as in DBR type lasers. A tuning range of 35 nm could be achieved, however corresponding linewidth data has not been reported from these lasers. Double RRs with a reflector in a large loop show 110 kHz linewidth but the tuning range is limited to 34 nm [17].

Silicon and silicon nitride platform have developed RRs with low loss waveguides, which maximize the benefit stated above of RRs for the extensive tuning range and the narrow linewidth [18], [19], [57]. Reference [59] demonstrates double RR and quad RR lasers based on silicon RRs with 40 nm tuning and linewidth of 2 kHz and 110 nm tuning with 220 Hz linewidth. Moreover, silicon nitride RR laser also reported a 120 nm tuning range with sub 100 Hz linewidth [19]. Despite their outstanding performance, silicon and silicon nitride require III-V active sections for a hybrid integration due to their indirect bandgap. The extra integration increases fabrication cost for a wafer bonding or butt coupling.

3. Sampled Grating DBR lasers

3.1. SG DBR laser for the generic foundry platform

Today, open-access generic foundry platforms [60], [61] provide integrated optoelectronic components from a single wafer to design and fabricate photonic integrated circuits (PICs) within multi-project wafer runs. Thus customers can realize a wide range of PICs from academic to industrial use based on active (e.g., laser and gain) and passive (e.g., waveguide, coupler, photodiode, filter, and reflector) components. However, only a few tunable laser types are compatible with an InP generic foundry platform because of the difficulty of optimizing tuning sections without other building blocks' performance degradation. Within the platform technology, reference [17] demonstrates tunable lasers based on RR filters with optical linewidth of 110 kHz, but the tuning range is limited 34 nm. MZIs are used as tuning sections for a tuning range of 74.3 nm with optical linewidth of 363 kHz [54]. However, this laser suffers from relatively large footprint of 3.65 x 0.9 mm^2. CCLs are realized using two coupled laser cavities [51], but a tuning range is limited by 6.5 nm.

In this chapter, novel SG DBR lasers are reported, fabricated by the foundry platform [60] for the first time. These lasers show a 53 nm tuning range in the C band and measured side mode suppressions (SMSRs) are over 42 dB. Lorentzian optical linewidth is 713 kHz and the footprint of the whole laser is 2.3 x 0.3 mm^2. From this work, the foundry platform supports the SG DBR building block in the PDK now. Partial results of thie work have been published in [62].

3.2. Design and modeling

This chapter introduces design and modeling for the SG DBR laser fabricated by the foundry platform process. It includes optimization of optical waveguides, SG DBRs, and the laser.

3.2.1. Optical waveguide

A ridge waveguide is a widely used structure for lasers, fabricated by wet-chemical etch to create the top of the InP, and hence the structure shows a trapezoid as illustrated in Figure 6 (a). The ridge width is 2.4 µm for the top and 2.2 µm for the bottom, and the height is 1.8 µm. The waveguide is based on the p-n junction of p-doped InP on the top, n-doped Q1.3 layer, and the substrate. Q1.3 layer with 250 nm is located between InP, including most fields in the layer. Figure 6 (b) shows an electric field profile with the fundamental TE mode of the waveguide in Figure 6 (a). The profile is calculated by a commercial mode solver [63], which simulates the spatial profile of modes by solving Maxwell's equation. The calculated refractive index n_{eff} is 3.208 and the group index n_g is 3.59 with material dispersion. Gratings are patterned on the Q1.3 layer with 70 nm etching depth and with $n_{eff} = 3.185$, corresponding to a coupling coefficient of $\kappa_0 \approx 300\ cm^{-1}$.

The doping density is vital for the waveguide loss due to the free carrier absorption, as stated in 2.2.1. Weber investigated the loss from the carrier density in the InGaAsP by p- and n-doped [30]. From data for n-GaAs, the absorption from n-doped InGaAsP was suggested as

$$\alpha_n = 3.1 \times 10^{-22} N, \tag{3-1}$$

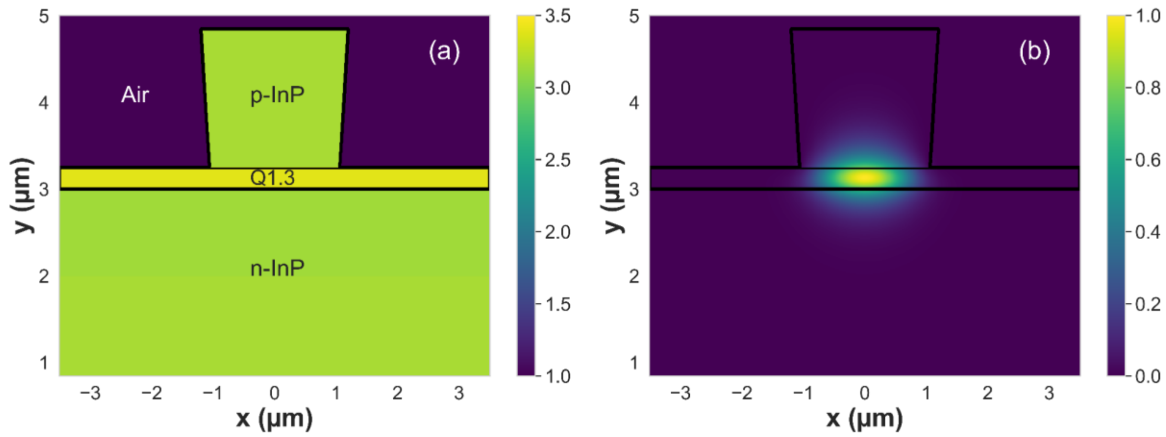

Figure 6 (a) Schematic cross section of the ridge waveguide with index distribution. (b) the electric field profile of the fundamental TE mode.

where N represents the electron density in m^{-3}, and the absorption is approximately uniform from 1 µm to 2 µm range. Typical bulk loss of n-doped InP is 4 dB/cm at λ=1.5 µm [64].

Dominant loss from the carrier is p-doped InGaAsP, which is given by

$$\alpha_p = 4.252 \times 10^{-20} e^{(-3.657E)} P, \tag{3-2}$$

where P denotes the hole density in m^{-3}, and E represents the photon energy in electron volts, typically 56 dB/cm with P = $10^{18}/\ cm^3$ at λ=1.3 µm [64]. As stated in [30], doping-related absorption does not depend on the specific composition of InGaAsP alloy and is also independent of the temperature. Figure 7 shows calculated absorption losses of p- and n-doped InP with various doping densities at λ=1.55 µm from (3-1) and (3-2).

The bandgap energy causes additional loss in the optical waveguide. When the photon energy is close to the bandgap energy of the material, the absorption occurs by exciting electrons into the conduction band. The bandgap energy is related to the InGaAsP's composition, and hence the loss depends on the PL. The loss from the electron transition is given by [30]

$$\alpha_{pl} = \alpha_0 e^{\left(\frac{E-E_0}{\gamma}\right)}, \tag{3-3}$$

where α_0 is 3000 cm^{-1}, γ is about 10 mV, and $E - E_0$ presents the difference energy from the photon and the PL. For the PL of 1.45 µm (Q1.45) at λ=1.55 µm, absorption loss is about 12 cm^{-1} (52 dB/cm) [30]. Figure 8 shows the absorption loss from the bandgap energy with different PL at λ=1.55 µm. Up to PL=1.35 µm, the loss is negligible but dramatically increases when PL closes to λ.

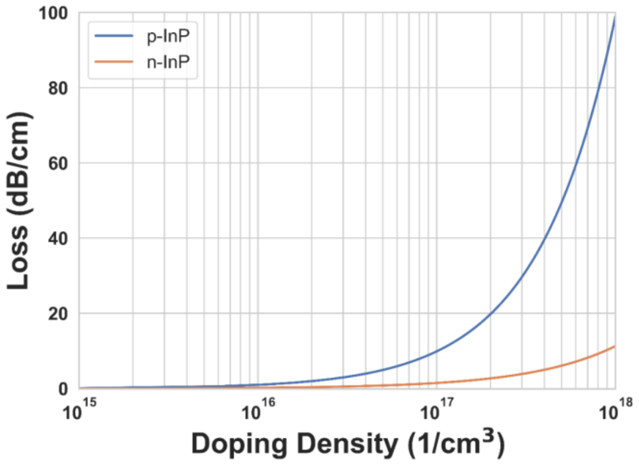

Figure 7 Absorption loss of p- and n-doped InP with different doping densities.

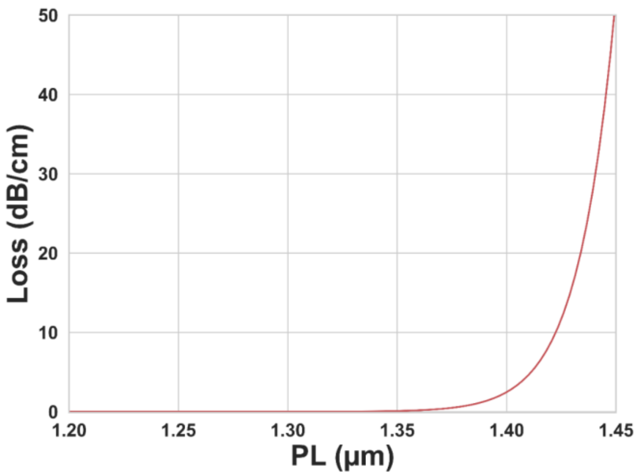

Figure 8 Absorption loss from the bandgap energy with variant PL.

The propagation loss of the waveguide is determined by the confinement of light in materials depicted in Figure 8. For example, the electric field profile shows mode overlap in the waveguide structure, including the doping density and PL, and thus this provides loss of the propagation based on (3-1), (3-2), and (3-3). Low doping density and PL are preferred to design a low loss waveguide. However, as shown in Figure 4, p-doped InP typically covers passive and active sections. Despite the low loss propagation for passive sections, low doping density degrades a series resistance of the active section. One way to reduce the loss is using the higher PL of the center layer to reduce mode overlap in the p-doped InP. However, the higher PL generates absorption loss over Q1.35, and thus Q1.3 is selected. Correspondingly, the propagation loss is 13.9 dB/cm from Figure 6 (b), involving absorption losses from (3-1), (3-2), and (3-3).

3.2.2. SG DBR

As Jayaraman reported [65], SG DBR consists of repeated waveguides and gratings with a sampling period. Figure 9 (a) shows the schematic image of the SG DBR with characteristic parameters. Z_0 represents the length of the period, i.e., the sampling period. The grating burst length is Z_1 with the grating period of Λ. The number of grating bursts is N, and hence N of Figure 9 is 3. L_{SG} denotes the total length of the SG DBR, which is given by $L_{SG} = Z_0 \times (N-1) + Z_1$. SG DBR can be considered a combination of short cavities with a length of Z_0, and thus cavities generate the discrete reflection spectrum as stated in chapter 2.1. The FSR of the SG DBR is derived by (2-13) as

$$\Delta\lambda = \frac{\lambda^2}{2n_g Z_0}. \tag{3-4}$$

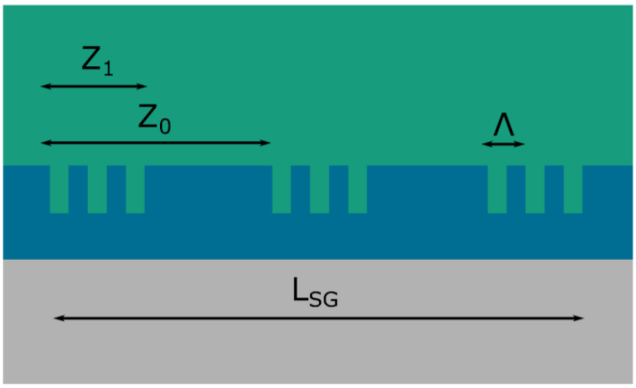

Figure 9 Schematic image of the SG DBR.

In the Fourier domain, a real space of the SG DBR is changed to spatial frequencies, which show the comb-reflection. SG DBR includes multiplication of continuous gratings with Λ, and a sampling function with the period of Z_0 and the width of Z_1. The continuous grating and the sampling function in the real domain are changed to a delta and sampling function, respectively. Consequently, the frequency response is calculated by convolving the grating and sampling function, which is a convolution of the delta function and a sampling comb. Reference [65] carefully investigated the Fourier transform and suggested coupling coefficients of each peak, given by

$$\kappa(n) = \kappa_0 \frac{Z_1}{Z_0} \frac{sin(\pi n Z_1/Z_0)}{\pi n Z_1/Z_0} e^{-i\pi n Z_1/Z_0}, \tag{3-5}$$

where n is the number of the peak, κ_0 is the coupling coefficient of the Bragg grating from (2-12). The number of peaks in the half of the maximum reflection (N_{3dB}) is approximately identical to the integer of Z_0/Z_1, and hence the the FWHM of the envelope is given by

$$\Delta\lambda_{3dB} = N_{3dB}\Delta\lambda = \frac{\lambda^2}{2n_g Z_1}. \tag{3-6}$$

For the order zero (n=0), the reflectivity of the peak is determined by the total grating length ($N \times Z_1$) and κ_0:

$$R_{max} = tanh^2(\kappa_0 N Z_1). \tag{3-7}$$

The effective length of the SG DBR (L_{eff_SG}) is larger than a typical DBR length because the sampling structure includes repeated waveguides. At Bragg wavelength, the length is derived by [66], [67]

$$L_{eff\_SG} = \frac{1}{\kappa_{SG}} tanh(\kappa_{SG} L_{SG}), \tag{3-8}$$

Where κ_{SG} denotes the coupling coefficient of the SG DBR, which is

$$\kappa_{SG} = \frac{N Z_1}{L_{SG}} \kappa. \tag{3-9}$$

Due to the SG DBR's sampling structure, κ_{SG} spacially averages κ from (2-12).

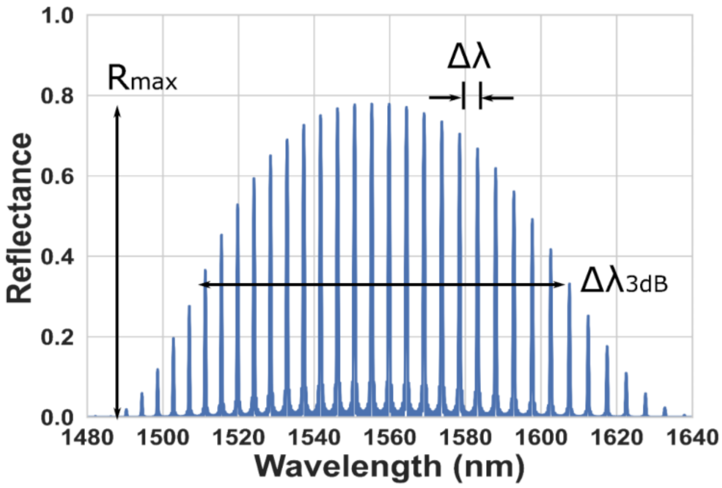

Figure 10 Simulated reflection spectrum of the SG DBR by TMM.

TMM can calculate the com-like reflection more precisely such as shown in Figure 10 with $\kappa_0 = 300\ cm^{-1}$, $Z_0 = 74.3\ \mu m$, $Z_1 = 4.39\ \mu m$, $\Lambda = 242.46\ nm$. Optimized parameters of the SG DBR uses the Vernier effect to maximize the tuning range, and reference [48], [65], [66] investigated the detail theory and model of the SG DBR.

3.2.3. Laser structure

Figure 11 shows a schematic image of the SG DBR laser based on the HHI foundry process, which includes four sections: a front and rear SG DBR, gain, and phase section. Similar to the three section DBR laser in Figure 4, the Q1.3 layer is sandwiched between the p- and n-doped InP layer and Fe-doped InP is used for a substrate. The gain section includes MQWs, and the phase section is designed to control the cavity modes. The gain section is connected to pads to apply a forward bias to amplify photons. Thermal heaters are deposited on SG DBRs and phase sections to control wavelengths by the Vernier effect. The lengths of the sections are 500 µm, 400 µm, 400 µm, and 800 µm, respectively.

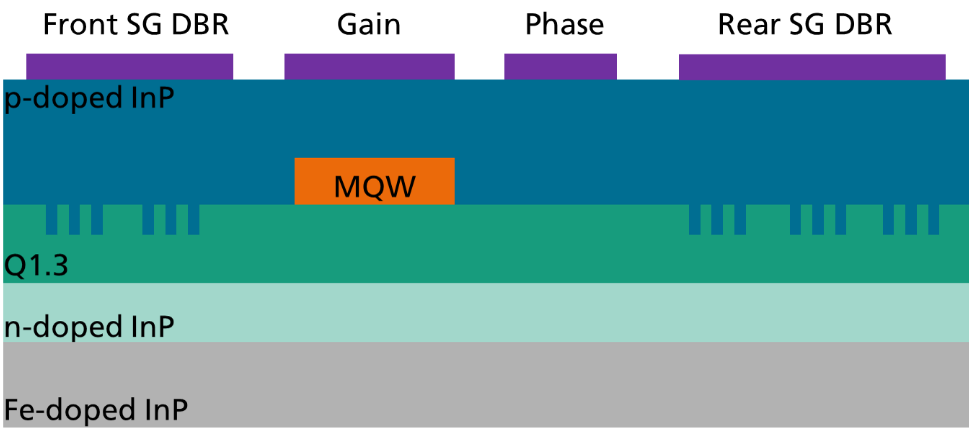

Figure 11 Schematic image of the SG DBR laser

The principle of wavelength selection by the Vernier effect in the SG DBR laser is shown in Figure 12. Figure 12 (a) depicts reflection spectra of the front and rear SG DBRs (green and blue curves) and cavity modes of the laser cavity (black dash lines). $\Delta\lambda$ of the front and rear SG DBRs are $\Delta\lambda_f$ and $\Delta\lambda_r$, respectively. $\delta\lambda$ denotes the difference of $\Delta\lambda_f$ and $\Delta\lambda_r$ ($\delta\lambda = \Delta\lambda_f - \Delta\lambda_r$). The coincidence at λ_2 points out the wavelength matching both SG DBRs and, it corresponds laser's operating wavelength. In Figure 12 (b), the rear SG DBR is shifted to the longer wavelength region by $\delta\lambda$ whereby the coincidence wavelength of λ_3 is selected. The wavelength difference of λ_2 and λ_3 is $\Delta\lambda_r$. Accordingly, such a slight tuning of $\delta\lambda$ tunes the significant wavelength of $\Delta\lambda_r$. Figure 12 (c) presents an equivalent wavelength selection by the front SG DBR, which is shifted by $\delta\lambda$ but the selected wavelength is λ_1.

When both reflection spectra shift by equal wavelengths, the coincidence point moves continuously. In this case, the corresponding wavelength of laser's output shifts discretely with the FSR of cavity modes. It can access wavelengths between peaks of the comb-like reflection, e.g., $\Delta\lambda_f$ and $\Delta\lambda_r$. Figure 12 (d) shows the wavelength is increased by FSR from λ_2.

The phase section is designed to cover the wavelength region between cavity mode jumps. The tuning on the phase section can shift the cavity modes in the cavity, as discussed in chapter 2.1. Consequently, controlling passive sections of SG DBRs and the phase section can access all wavelengths in the tuning range, so called quasi-continuous tuning.

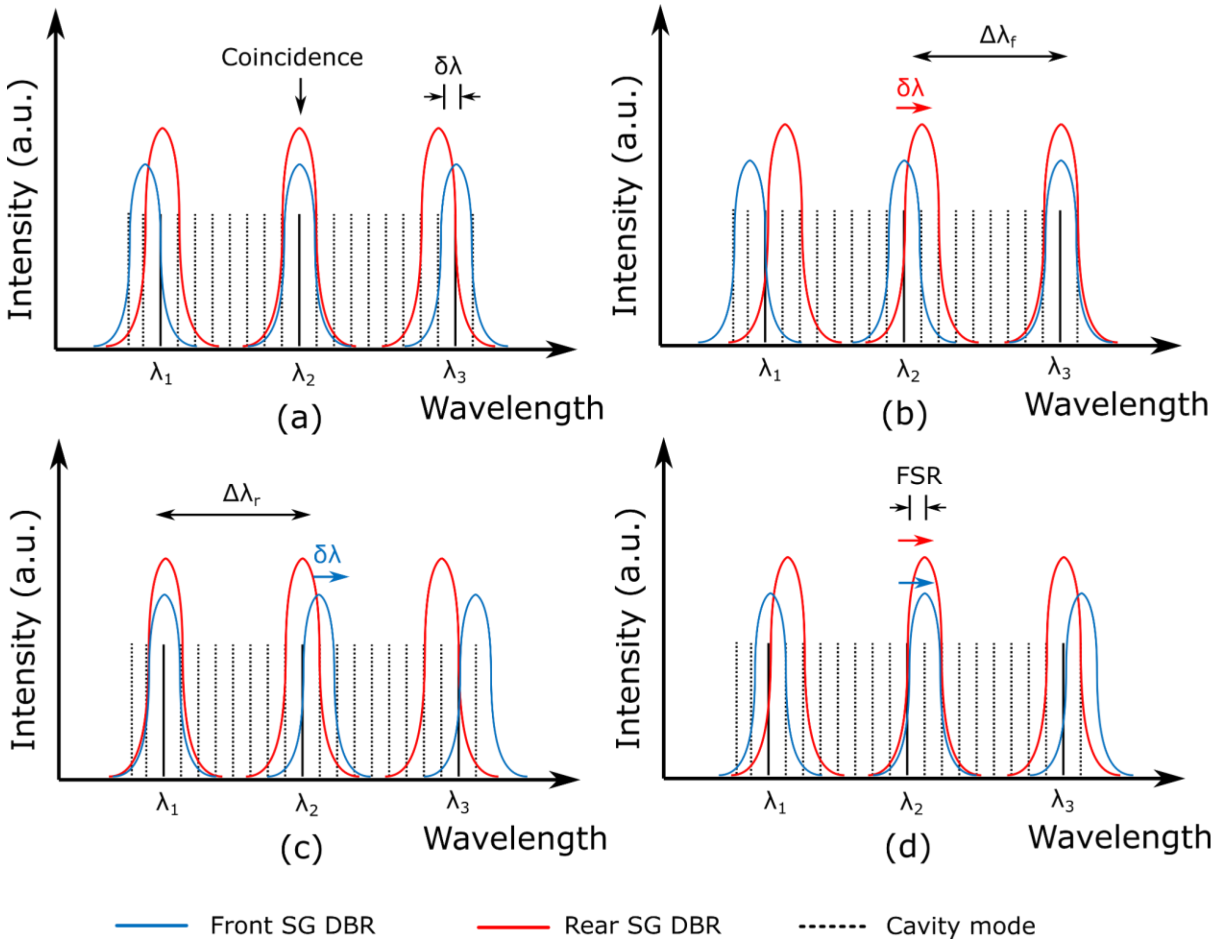

Figure 12 The Vernier effect of the SG DBR laser. (a) reflection spectra of the front (blue) and rear (red) SG DBRs. Dashed lines represent cavity modes, and standard lines illustrate coincidence wavelengths (λ_1, λ_2, and λ_3). The coincidence wavelength is λ_2. $\delta\lambda$ shows the difference of peak spacing between the front and rear SG DBRs. (b) The reflection spectrum of the rear SG DBR is shifted by $\delta\lambda$. This leads the coincidence wavelength to move on λ_3, which is jumped from λ_2 by $\Delta\lambda_f$. (c) λ_1 is selected by shifting the front SG DBR with $\delta\lambda$, and the shift is $\Delta\lambda_r$. (d) Both reflection spectra shift together by FSR to select the next cavity mode.

A limitation of the tuning range by the Vernier effect originates from repeated coincidences between the comb-like filters. For example, in the case of two SG DBRs with $\Delta\lambda_f$ = 5 nm and $\Delta\lambda_r$ = 4 nm, the periodicity leads to repeated coincidence points at 20 nm on both sides around the main coincidence. When the gain bandwidth is wider than the 20 nm, multi wavelengths are operated. To increase the tuning range, the distance between repeated coincidences has to be extended by the increased $\Delta\lambda$ and reduced $\delta\lambda$, as [68]

$$\Delta\lambda_{tuning} = \frac{\Delta\lambda_f \Delta\lambda_r}{\delta\lambda}. \quad (3\text{-}10)$$

In order to increase $\Delta\lambda_{tuning}$, improved tuning methods directly extend $\Delta\lambda_f$ and $\Delta\lambda_r$ in (3-10). As stated in chapter 2.2, the current injection has the large Δn, but it suffers from enormous losses due to the free-carrier absorption, leading the broad optical linewidth. QSCE requires extended filter length due to the small Δn. Thus, thermal tuning is widely used for the SG DBR laser because of over 5 nm tuning range with low losses [11], [15]. An optimized design with the small $\delta\lambda$ can increase $\Delta\lambda_{tuning}$, but it requires the high Q factor of combe-like filters. When $\delta\lambda$ is reduced, the overlap between the reflections at second peaks (see λ_1 and λ_3 in Figure 12 (a)) is increased, and thus SMSR is also enlarged. SG DBRs require a lower coupling coefficient to realize a high Q factor, giving rise to longer structure length [65]. However, electron-beam lithography allows limited length with higher accuracy, and hence the Q factor is restricted. Typical $\delta\lambda$ for the SG DBR laser is below 0.5 nm with $\Delta\lambda$ over 5 nm, and duty cycle of Z_1/Z_0 is below 10% to demonstrate over the C-band tuning [65]. Furthermore, to suppress the unwanted coincidences, $\Delta\lambda_{3dB}$ is designed to suppress the undesired coincidences, or restricted gain bandwidth of MQWs is used.

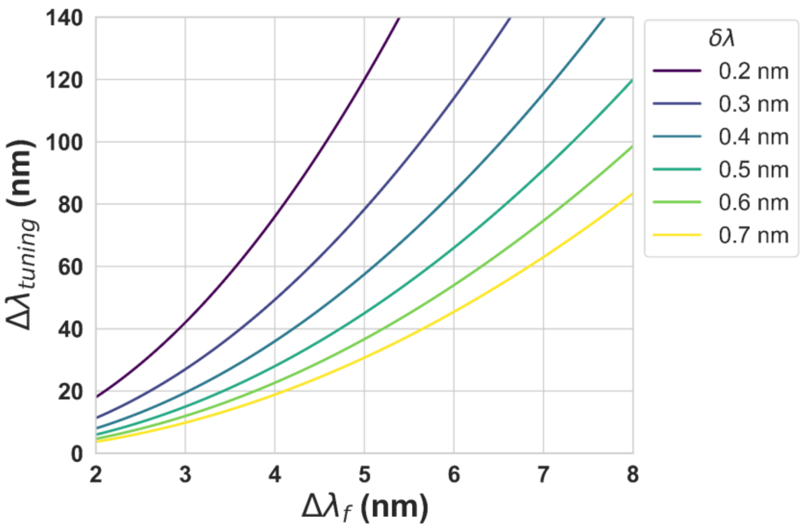

Figure 13 Tuning range ($\Delta\lambda_{tuning}$) of the Vernier effect with different $\Delta\lambda_f$ and $\delta\lambda$.

Figure 13 depicts calculated $\Delta\lambda_{tuning}$ from (3-10) with different $\Delta\lambda_f$ and $\delta\lambda$ [69]. The corresponding $\Delta\lambda_f$ is determined by the difference between $\Delta\lambda_f$ and $\delta\lambda$ ($\Delta\lambda_r = \Delta\lambda_f - \delta\lambda$). For the C band tuning range, $\Delta\lambda_f$ = 4~5 nm and δλ = 0.5 nm are proper. In order to demonstrate over the 100 nm tuning, $\Delta\lambda_f$ > 6 nm with δλ < 0.4 nm is required.

To cover the tuning range of 45 nm for C band, $\Delta\lambda_f$ and $\Delta\lambda_r$ are optimized as 5 and 4.5 nm, respectively, and the corresponding δλ is 0.5 nm. To realize the parameters, the front SG DBR contains Z_0 = 67 µm, Z_1 = 4.3 µm, and N= 8. The rear SG DBR includes Z_0 = 74.3 µm, Z_1 = 4.4 µm, and N = 11. Both SG DBRs use Λ = 242.46 nm to match the center of the wavelength at 1550 nm. According to (3-6), $\Delta\lambda_{3dB}$ is 76.2 nm and 77.6 nm for the front and rear SG DBRs, respectively. Notwithstanding $\Delta\lambda_{3dB}$ is larger than $\Delta\lambda_{tuning}$, the gain bandwidth of MQWs is limited to an around 60 nm. Thus, the restricted bandwidth suppresses unwanted coincidences. The Z_1 is designed as long as possible to increase L_{SG} for the high Q factor. Target maximum reflections are 60% and 80% at the center of wavelength for the front and rear SG DBRs based on (3-7). Design parameters of SG DBRs are summarized in Table 2.

Table 2 SG DBR design parameters

	Front SG DBR	Rear SG DBR
Z_0	67 μm	74.3 μm
Z_1	4.3 μm	4.4 μm
N	8	11
L_{SG}	472.3 μm	747.3 μm
Λ	242.46 nm	

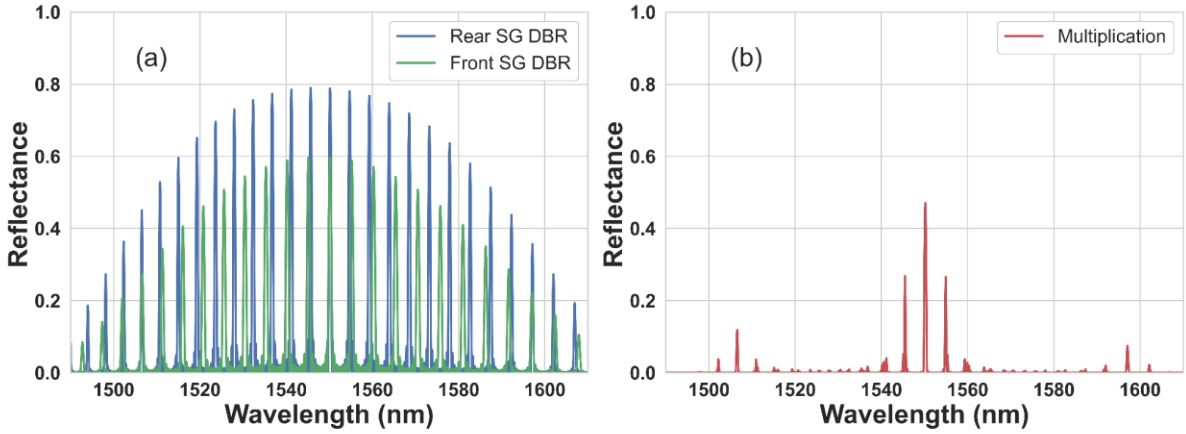

Figure 14 (a) Reflection spectrum of front and rear SG DBRs calculated by TMM. (b) Multiplication of spectra from Figure 14 (a).

Figure 14 (a) shows calculated reflection spectra of the front and the rear SG DBR by TMM with design parameters in Table 2. The propagation loss of 13.9 dB/cm is included. Simulated FWHMs from the maximum peak are 0.77 nm and 0.56 nm for the front and the rear SG DBR, respectively. Spectrum characteristics of TMM is well matched to the values from (3-1), (3-3), and (3-4). SMSR is related to a difference between the central peak and the second strongest peak in Figure 14 (b), which shows about half. The experimental result of SMSRs is demonstrated over 42 dB, and it will be investigated in next chapter.

The FSR of cavity modes of the laser cavity based on (2-13) is described by [68]

$$\text{FSR} = \frac{\lambda^2}{2(n_{,active}L_{active} + n_{g,passive}L_{passive})}, \tag{3-11}$$

where $n_{g,active}$, and $n_{g,passive}$ represent group indexes of the active and passive section. $L_{passive}$ includes the phase length and L_{eff_SG} for the front and rear SG DBRs. The calculated FSR is 0.27 nm with simulation parameters as follow: $n_{g,active}$ = 3.8, $n_{g,passive}$ = 3.59, L_{eff_SG} of the front and rear SG DBRs = 177.2 and 231 µm.

3.3. Experiment

Figure 15 shows the developed SG DBR laser, which includes the front SG DBR, gain, phase, and rear SG DBR sections as shown in Figure 11. The footprint of the whole SG DBR laser is 2.3 x 0.3 mm^2. The laser is based on the ridge waveguide, which is realized on Fe-doped InP substrate. The grating- and phase sections are defined by selectively removing the MQW-layers down to the Q1.3 layer underneath. The light from MQWs is coupled to the Q1.3 layer in a so-called offset-quantum well. The p-InP layer is deposited, and selectively Zn is diffused on the gain section to reduce the series resistance. To define the waveguide, reactive ion beam- (RIE) and wet etch process in the generic technology are used. Afterward, the DBR gratings are defined by direct-writing with electron-beam lithography and subsequently etching into the Q1.3 layer. As studied in section 3.2.1, the resulting coupling coefficient κ is around 300 cm^{-1}. To achieve the narrow optical linewidth, platinum heaters for thermal tuning are realized on top of the SG DBR- and phase sections to tune the SG DBR reflection spectrum and the cavity mode spacing of the laser cavity. The gain section includes p-contact on the upper and n-contact on the bottom side, connected to the contact pads on the top of the laser. Contact pads are designed to use a multi-needle probe for applying currents to each section. The front and the rear output facet are tilted at 7°, and an anti-reflection coating is covered to avoid reflection from the waveguide to the air. With the foundry platform process [60], I fabricated laser with minor modifications regarding the grating etching depth in the SG DBR section only.

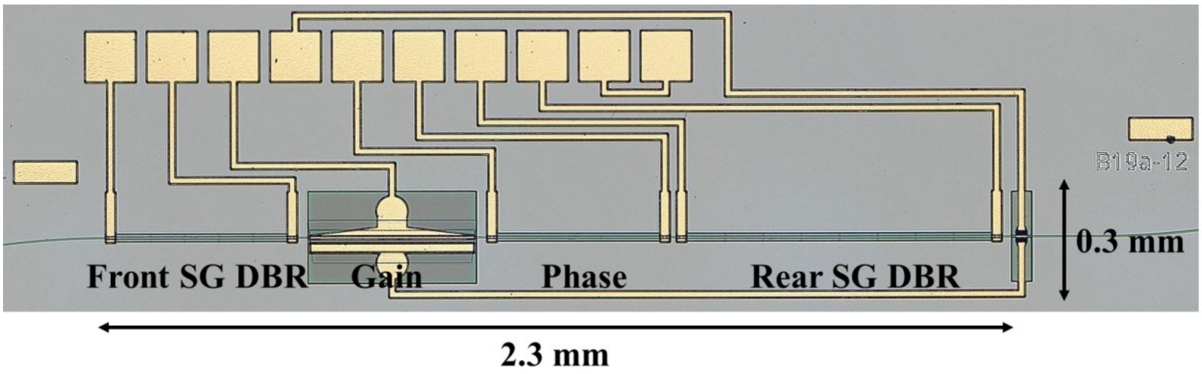

Figure 15 Microscope image of the fabricated SG DBR laser.

3.3.1. Pulsed PI measurement

The SG DBR laser is mounted on an Au coated heat sink to achieve good heat dissipation and stabilize the temperature at 20°C by a thermoelectric cooler (TEC) to test the optical performance. Figure 16 depicts pulsed PI curves with an integrating sphere from the front facet with 0 to 150 mA currents. A measured threshold current is 20 mA, and the front facet output power amounts to 8 mW at 100 mA gain current with 2.6 V. No current is applied to the tuning sections in this case.

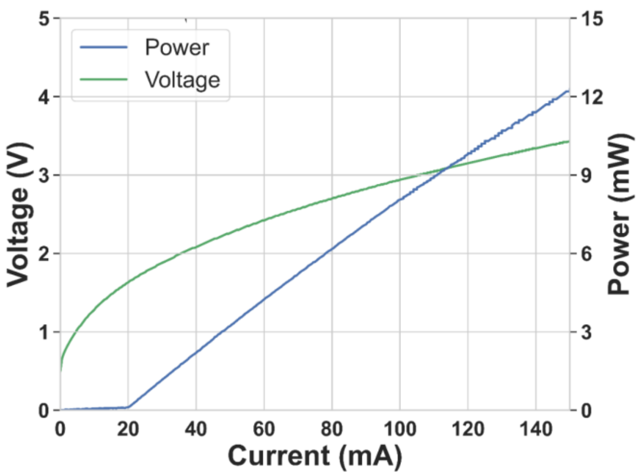

Figure 16 Experimental measurement of the output power without current injection on passive sections.

3.3.2. Tunable wavelength performance

To measure the tuning performance, a tapered fiber collected the light from the AR coated 7° output facet, and an optical isolator is connected to prevent back reflections from the measurement setup. An optical spectrum analyzer (OSA) measures the signal with 0.07 nm resolution. The electrical multi-probe, including multiple needles, is connected to the electrical pads on top of the contact pads to control each section using Keithley source meters. The current of 100 mA is applied to the gain section and set at 20°C by TEC.

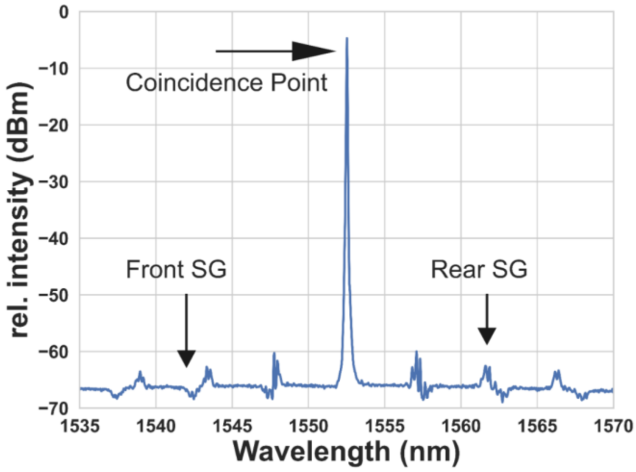

Figure 17 Optical spectrum of the SG DBR laser without tuning currents to passive sections. The main peak shows the coincidence point of two SG DBRs. Small peaks originates from the rear SG DBR's reflection, and the front SG DBR's transmission causes dips.

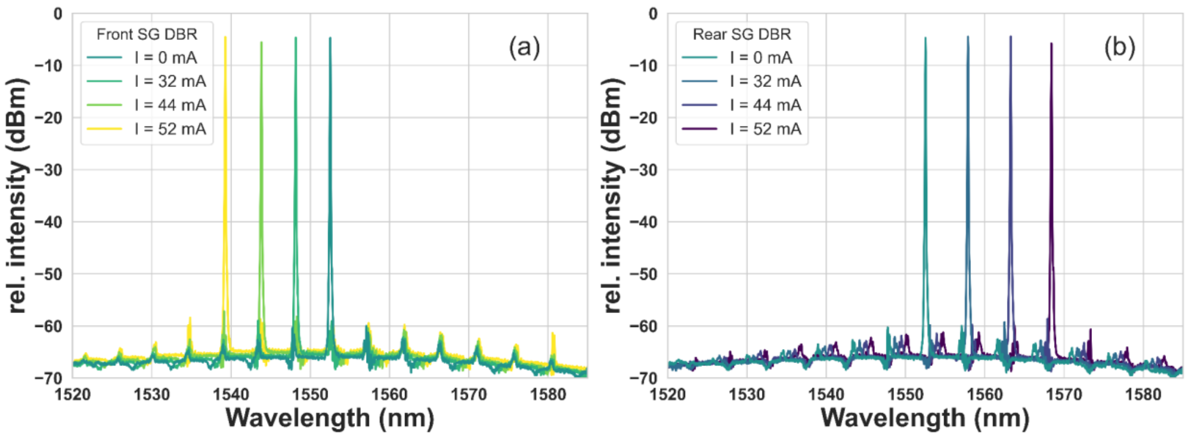

Figure 18 (a), (b) superposed optical spectra with different currents to the front and the rear SG DBR.

Figure 17 shows an optical spectrum from the SG DBR laser with no currents to tuning sections. The central peak is 1552.52 nm with an SMSR of 55.3 dB. Small peaks in Figure 17 depict reflections from the rear SG DBR. Furthermore, small dips originate from the transmission of the front SG DBR. When tuning heaters operate to control reflection spectra of SG DBRs, the coincidence wavelength is shifted where the peak and dip are matched.

Superposed optical spectra are depicted in Figure 18 with different currents to the SG DBR heaters. As discussed in chapter 2.2.3, heating increases the refractive index, resulting in shifting the reflection spectrum of the SG DBR to longer wavelengths. Thus, Figure 18 (a) shows shifted wavelengths to the shorter wavelength range with different currents on the heater of the front SG DBR due to the longer $\Delta\lambda_f$ than $\Delta\lambda_r$, as shown in Figure 12 (c). The wavelength jump is around 4.5 nm, which matches the target $\Delta\lambda_r$ of the rear SG DBR without tuning on the phase and the rear SG DBR section. Contrarily, tuning on the rear SG DBR changed the coincidence to the longer wavelength region with 5 nm of $\Delta\lambda_r$ as Figure 18 (b).

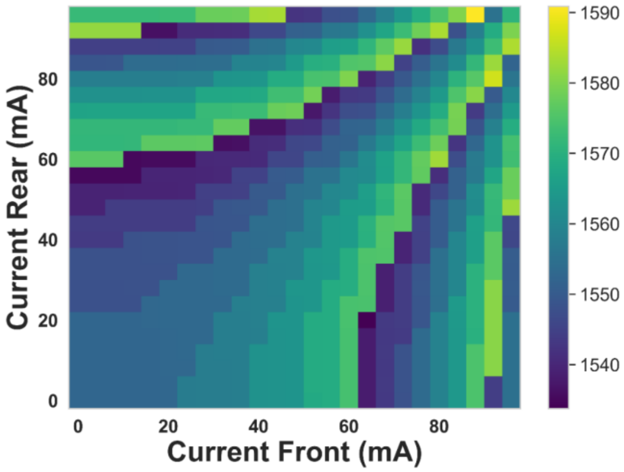

Figure 19 A wavelength mapping at current of 100 mA on the gain section. Different currents are applied to the front and the rear section. Peak wavelengths (nm) are shown.

The measured peak wavelengths are shown in Figure 19 with applied currents on the front and the rear SG DBR from 0 mA to 88 mA with 4 mA interval. For this measurement, the gain current of 100 mA is applied to the gain section, and the phase section is not controlled. The combination of controlling both SG DBRs presents the wavelength shift as discussed in Figure 12, which includes wavelength jumps from reflection peaks and cavity modes, namely the wavelength mapping. Based on the wavelength data as a look-up table, the SG DBR laser could select any wavelengths in the tuning range with the FSR of cavity modes. Figure 20 shows superposed optical spectra, covering the wavelength tuning range of 53 nm from 1533 to 1586 nm. The obtained tuning range exceeds the target of the 45 nm by more than 8 nm. The extended tuning is in the longer wavelength region can be explained by a red shift of the gain curve due to a thermal effect from heaters near the gain section. Furthermore, corresponded SMSRs for the 53 nm are over 42 dB as shown in Figure 21. Relatively low SMSRs is observed at both ends of the tuning range, since the reflection spectrum has an envelope as depicted in Figure 14 (a). By using the phase section for fine tuning of wavelength shifts and improved SMSRs can be achieved.

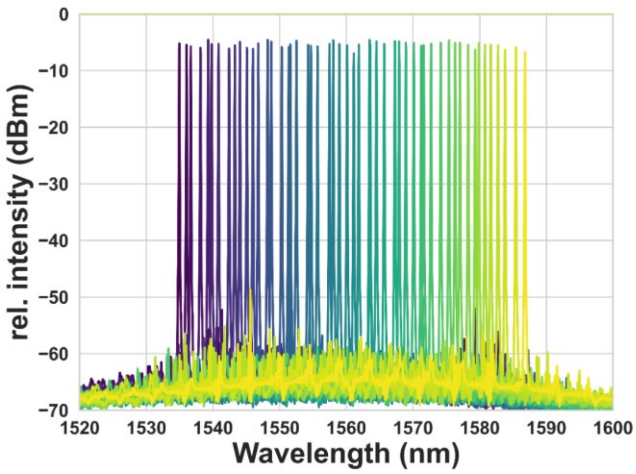

Figure 20 Superposed spectra with 53 nm tuning range.

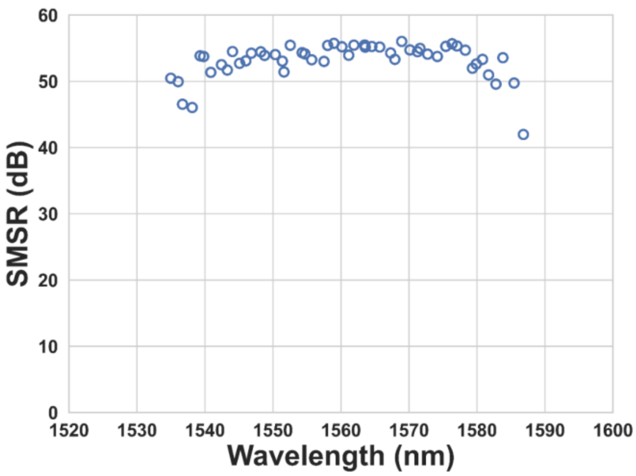

Figure 21 SMSRs of the SG DBR laser over 42 dB.

3.3.3. Linewidth measurement

The optical spectrum of the single mode laser generates not a monochromatic wavelength but small bandwidth, which determines the optical linewidth of the laser. The linewidth stems from two main reasons: quantum noise and technical noise [56]. The quantum noise of semiconductor lasers is caused by amplified spontaneous emission (ASE), which adds phase fluctuation to the stimulated emission. Moreover, ASE generates refractive index fluctuations following a change in the carrier density. The phase noise from ASE changes a small amount of the optical intensity in the laser mode, leading to restoring the steady state. The restoration generates refractive index variations, which causes additional phase fluctuations and linewidth broadening [70].

Schawlow and Townes theoretically derived the well-known expression for the optical linewidth of lasers [71], and Henry modified this for diode lasers with the linewidth enhancement factor as [70], [72]

$$\Delta\nu = \frac{h\nu v_g^2 n_{sp}\alpha_m(\alpha_i + \alpha_m)(1+\alpha_H^2)}{8\pi P}, \tag{3-12}$$

where $h\nu$ is the photon energy, v_g is the group velocity, n_{sp} is the spontaneous emission coefficient, α_m is the mirror loss, α_i is the internal cavity loss, and α_H is the linewidth enhancement factor from [70]. P is the laser output power, assuming that equal power couples out to two facets. This formula is referred to as the Schawlow-Townes-Henry linewidth.

The technical noise originates from various factors, e.g., shot noise in the tuning region, thermal noise of bias source, and fluctuations of bias source [73], which are in the shape of 1/f for the frequency noise spectrum, dominating at lower frequency region [74], [75].

The optical spectrum of lasers has a Gaussian shape near the peak and a Lorentzian shape away from the peak, namely the Voigt profile [76]. The 1/f noise contributes to the Gaussian part, and thus an intrinsic linewidth is defined by only the Lorentzian part. The typical intrinsic linewidth of semiconductor lasers is from a few kHz to hundreds of MHz, requiring high resolution measurement. Standard optical spectrum analyzers are not capable of such high resolution.

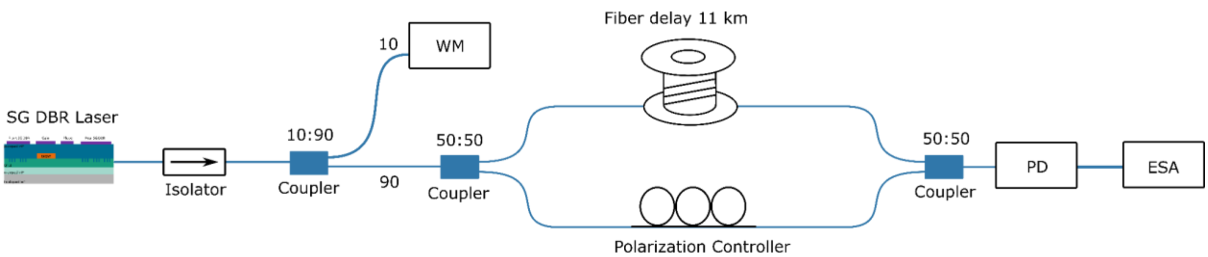

Figure 22 Schematic image of a delayed self-homodyne measurement setup.

Figure 22 depicts the delayed self-homodyne measurement setup, which has been widely used for the linewidth measurement since it was reported in 1980 [77]. The fundamental concept of this method is using an asymmetric MZI to generate the interference signal, including the phase noise of the laser source. The optical output power from the SG DBR laser is connected to an optical isolator, preventing back reflection from the measurement setup. A 10:90 coupler taps 10% power to a wavemeter (WM) for monitoring the operating wavelength. The rest of the signal is divided by a 50:50 coupler for two arms. One arm includes an 11 km fiber delay, which is designed to be longer than the coherent length of the laser signal. With the long fiber delay, two beams in the interferometer are uncorrelated, and hence this uncorrelated condition determines the minimum linewidth of the setup. The estimated minimum linewidth of the 11 km fiber delay is about 18 kHz [78], which is smaller than the measured linewidth analyzed in the following paragraph. Another arm consists of a polarization controller to match polarization of two beams. A 50:50 coupler combines two arms, and the superposed light generates the interference signal, which is capable frequency for the PD. An electric spectrum analyzer (ESA) is connected to the PD to analyzing the electrical signal.

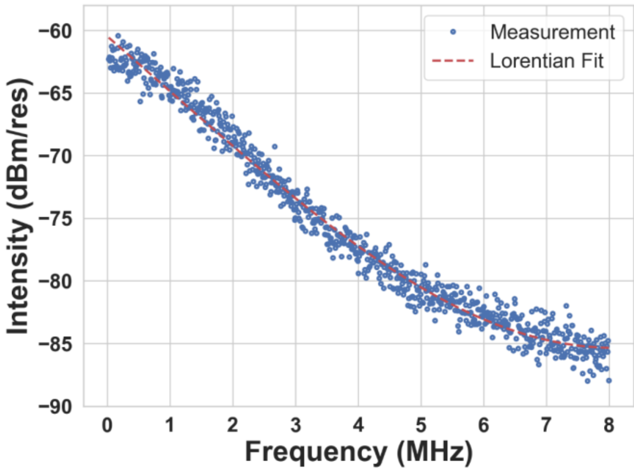

Figure 23 Linewidth of the laser of 713 kHz is measured (blue circle) with Lorentzian fit (red line).

The measured electrical spectrum up to 8 MHz is shown in Figure 23. Here, a current of 100 mA is applied to the gain section without any tuning on the passive sections. The red dotted line shows the Lorentzian fit of the measured data as shown in blue circles. The intrinsic linewidth is deduced to 713 kHz.

4. SG DBR lasers with an integrated RR for predetermined channels

This chapter reports a novel SG DBR RR laser, consisting of the four section SG DBR laser with an integrated RR. The additional RR provides wavelength channels with a fixed wavelength spacing and improves the optical linewidth simultaneously. This chapter includes simulations of laser components, design of the laser, and an experiment showing the fabrication and characteristics of the wavelength tuning and the optical linewidth. In order to verify the proposed concept, a typical SG DBR laser is realized based on the same wafer to compare optical performances. Moreover, an optimized SG DBR laser is demonstrated with a 98 nm tuning range with the same layer stack of the SG DBR RR laser. Partial results of this work have been applied for [79].

4.1. Tunable lasers for prefixed wavelength channels

For coherent DWDM, tunable lasers are preferred over fixed wavelength lasers. Tunable lasers have the advantage of realizing cost-effectiveness by realizing flexible and sliceable channels compared to fixed wavelength lasers [11]. For DWDM applications, the wavelength of tunable lasers has to be exactly tuned to an equal wavelength grid, the so-called International Telecommunication Union (ITU) grid [80] having a frequency grid spacing of, e.g. 50 GHz, 100 GHz or 200 GHz. The ITU-grid is used for channel spacing in DWDM at wavelengths around 1550 nm and is defined by ITU-T G.694.1. The ITU-grid is defined relative to 193.1 THz and extends from 191.7 THz to 196.1 THz with 100 GHz spacing. While defined in frequency, the grid is often expressed in terms of wavelength, in which case it covers the wavelength range of 1528.77 nm to 1563.86 nm with approximately a 0.8 nm channel spacing. For practical purposes, the ITU-grid has meanwhile been extended to cover 186 THz to 201 THz and subdivided to provide 50 GHz (0.4 nm), 25 GHz (0.2 nm), and even 12.5 GHz (0.1 nm) spaced grids. Therefore a tight control and fine-tuning of the wavelength are desired. External FP etalons are generally used as a filter with a FSR corresponding to the ITU-grid. After passing through the filter, a photodetector monitors the signal to find the accurate wavelength [81], [82]. However, most published approaches are based on fiber or free space optics [83]. So bulky modules and thus expensive packaging is needed.

In some approaches, CCLs are used where the cavity length has been optimized to match the 100 GHz grid. These lasers consist of two cavities coupled with one reflector. One cavity length is matched to the 100 GHz, and thus control of the second cavity generates wavelength tuning matched automatically to the ITU 100 GHz grid [53]. However, narrow optical linewidth cannot be expected because of the extended active length with high optical losses in CCLs. Thus, it is desired to improve existing laser devices so as to provide a wide tuning range in combination with a narrow linewidth, which may be precisely tunable to a predetermined fixed wavelength spacing grid, e.g., to the ITU-grid.

4.2. Concept of SG DBR RR lasers

Reference [84], [85] demonstrate a DBR laser with an intra-cavity RR to realize the narrow linewidth of 63 kHz. The laser is based on a four section DBR laser, comprising front and rear DBR, gain and phase section. Furthermore, a RR is designed in the middle of the four section DBR laser to increase the effective cavity length. Light resonates in the cavity with two DBR mirrors and passes through the RR simultaneously. The RR is optimized to generate the single mode operation, including compact bent waveguides for a minimized circumference to increase FSR from the RR's filtering. In this case, when DBR's reflection bandwidth is equal to or smaller than the FSR, other modes from the RR are suppressed. Moreover, cavity modes from the whole laser cavity are also eliminated due to the high Q factor of RR. However, this concept does not demonstrate widely tuning range. Reference [85] shows a single wavelength only, and [84] demonstrates 50 GHz (~0.8 nm) tuning with QCSE. Furthermore, the laser output is coupled by the front DBR, which suffers from a loss in gratings.

The proposed SG DBR RR laser is for a proper solution of predetermined wavelength channels with improved optical linewidth. Figure 24 (a) and (b) show schematic images of the typical SG DBR laser and the SG DBR RR laser. The proposed laser is based on the typical four section SG DBR lasers as Figure 24 (a), including front and rear SG DBR, phase, and gain, as investigated in 3.2.3. The laser comprises the additional RR located in the middle of the SG DBR laser, which is designed for predetermined wavelength channels, e.g., DWDM ITU-grid. While light in the typical SG DBR laser resonates through the phase and gain section by two SG DBRs, the SG DBR RR laser adds the RR to this path. Amplified light from the gain section goes to a 85:15 MMI coupler passing through the transition component, which is designed to couple the shallow and deep etched waveguide (yellow and blue color, respectively). This will be discussed in chapter 4.3.2. At the 85:15 MMI coupler, light couples in the RR and resonant wavelengths couples to the bottom of the waveguide by a 50:50 MMI coupler. The light goes through another transition and the phase section. The light is reflected by SG DBR 2, and returns to the way it went. Finally, SG DBR 1 reflects the light, and this process is repeated. Furthermore, MMIs couples out light to port 1 and 2 simultaneously, which are tilted 7° with AR coating to avoid back reflection. In contrast to the typical design (Figure 24 (a)) where the front side of the cavity is terminated by the front SG DBR, in the new design the outputs of the two branches are coupled by the RR that causes less losses than the gratings. The separation is an etched area, which is inserted between the SG DBRs to block thermal crosstalk.

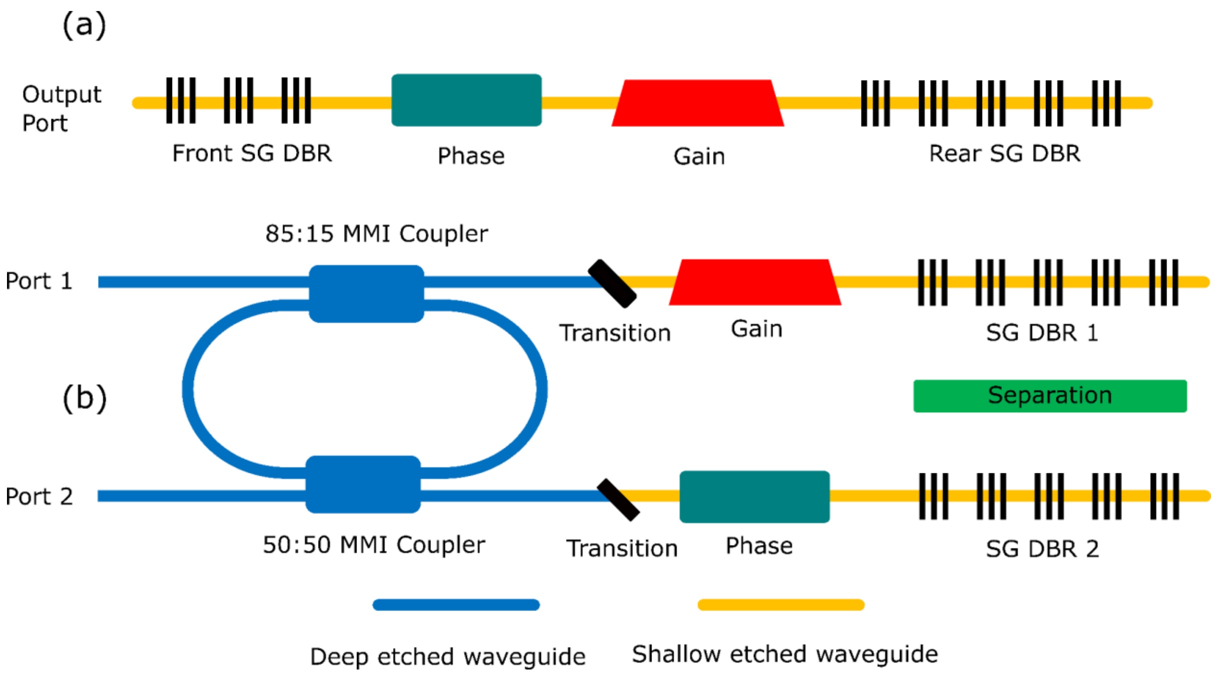

Figure 24 Schematic image of (a) typical SG DBR laser and (b) SG DBR RR laser.

Figure 25 (a) shows reflections of SG DBRs and cavity modes from the laser cavity of the SG DBR laser. As discussed in 3.2.3, controlling SG DBRs selects the coincidence wavelengths with the FSR of cavity modes. For example, the front and rear SG DBRs shift simultaneously to the longer wavelength region, and the laser's emitted wavelength is also tuned to larger but discretely with the cavity mode's FSR. In other words, such cavity modes also act as predetermined channels. Typical values of the FSR is from 0.2 to 0.3 nm according to (3-11), which depends on the effective cavity length of the laser. However, it is challengeable to control the FSR due to the limited Q factor of the SG DBR and long design lengths of each sections. First, when a long cavity length is designed to realize the small FSR, the single mode operation is not feasible because the reduced FSR is much smaller than the FWHM of the reflection peaks. Second, the design for small cavity length to realize the large FSR is difficult because the gain and phase section inherently requires 400 μm and 150 μm, and thus it is not feasible to realize the FSR larger than 0.58 nm according to (3-11).

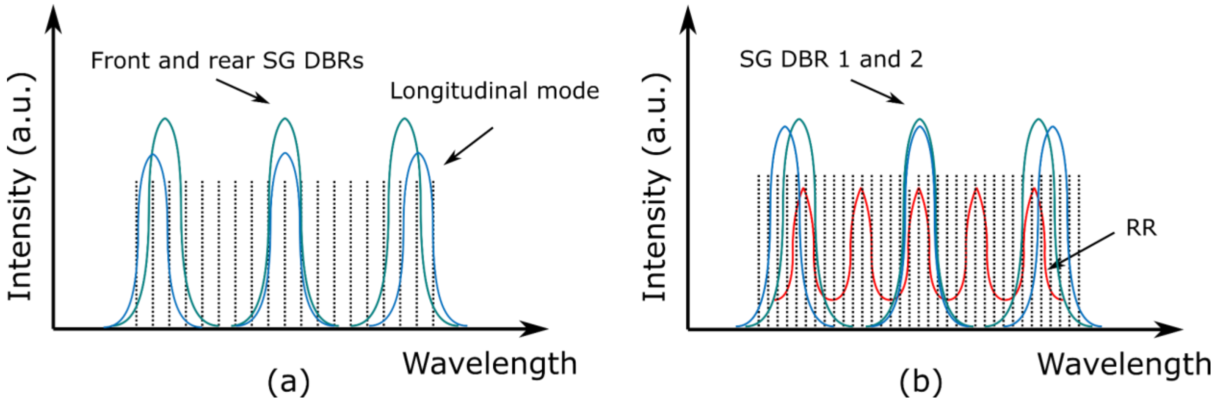

Figure 25 (a) Mode selection of the typical SG DBR with reflections of SG DBRs and cavity modes. (b) proposed SG DBR RR with SG DBRs reflections, longitudinal modes of FP (cavity modes) and a transmission of RR.

The proposed concept provides the additional RR's filtering, as shown in Figure 25 (b). A red line shows a transmission spectrum of the RR, which passes only specific wavelengths, satisfying a constructive interference condition in the loop structure. In contrast to the standard design in Figure 25 (a) where the front SG DBR is less reflection than the rear SG DBR, both SG DBRs in Figure 25 (b) are high reflections. It is because the laser's outputs are coupled by port 1 and 2. The FSR of cavity modes in Figure 25 (b) becomes smaller than Figure 25 (a) due to the extended cavity length by the RR. Despite of the smaller FSR of cavity modes, the single mode operation is feasible because the RR's Q factor is commonly high enough to suppress cavity modes, whereas the typical SG DBR has the limited Q factor. Therefore, when reflection spectra of SG DBR 1 and 2 shift simultaneously, the wavelength from the laser emits following the RR's FSR, which is simply adjusted by controlling the circumference of the loop structure. Accordingly, the FSR of the RR generates prefixed wavelength channels. Moreover, the extended cavity length also improve the optical linewidth of the laser.

Note that this concept focuses on providing prefixed channels, but the quasi continuous tuning is also possible when the RR is tunable. By tuning on all passive sections, the laser can access all wavelengths in the tuning range, whereas the additional tunable RR increases complexity to control the laser. In this chapter, the SG DBR RR laser without tuning on the RR is demonstrated.

4.3. Design and modeling

4.3.1. Waveguide

Waveguide propagation loss is crucial for the tunable laser's performance. As discussed in 3.2.3, the high Q factor determines the tuning range from the Vernier effect because such a narrow FWHM can suppress repeated mode from comb-like spectra. In order to demonstrate a high Q factor, filter structure requires a longer structure length. However, if the waveguide loss is significant, the total cavity loss is enlarged by the extended filter length, resulting in the broadened optical linewidth.

As investigated in 3.2.1, the main reason for the waveguide loss is the mode overlap in the p-InP. Reference [86] demonstrated low loss waveguides with the additional non-intentional doped (n.i.d.) InP and local diffusion of Zn. Both techniques focused on suppressing mode overlap in high doped p-InP, which leads to waveguide loss from 2 dB/cm to below 0.4 dB/cm. A low loss waveguide is designed based on the extra n.i.d. InP layer below the p-doped InP, as shown in Figure 26 (a). The p-InP is divided into two different levels of p- and p+InP layer, including lower doping for the p-InP than the p+InP. Moreover, a thin blocking n-InP layer is inserted between the n.i.d. InP and the p-InP to prevent Zn diffusion into the n.i.d. InP. In between the n-InP and n substrate, a thin Q1.06 layer is inserted as an etch stop layer for a deep etched waveguide. The deep etch will be discussed in the next paragraph. Figure 26 (b) shows the electric field profile of the waveguide with a fundamental TE mode, and most of the fields over Q1.3 layer are confined in the n.i.d. InP. The lower doped p-InP can reduce the waveguide loss, which is close to the electric field profile. This ridge waveguide is used for SG DBRs and the phase section in Figure 24 (b) with yellow color, so-called shallow etched waveguides.

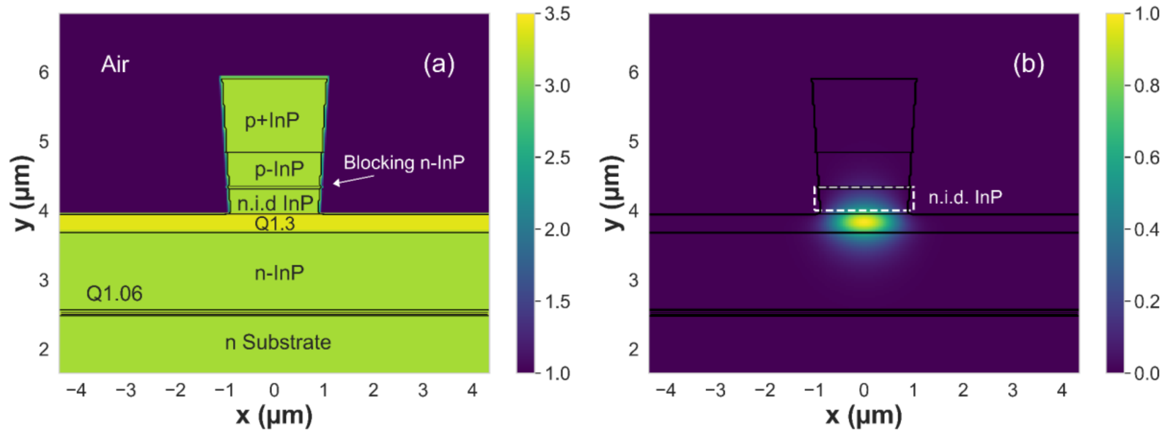

Figure 26 (a) Index distribution of the shallow etched waveguide with the n.i.d. InP and a blocking n-InP. (b) Electric field profile of the waveguide with the fundamental TE mode.

Deep etched waveguides are preferred for components requiring high index contrast, e.g., small radius bent waveguides and MMI couplers [61], [87]. In bent waveguides, the electric field profile moves from the center to outward, and hence high index contrast between the waveguide core and cladding improves the optical confinement of waveguides [88], [89]. Deep etched structure increases the index contrast compared to the shallow etched, which helps to realize small bent waveguides. This small footprint is also applied to MMI couplers to realize compact MMI couplers [87]. Therefore, the deep etched waveguide is optimized based on the same layer stack of the shallow etched ridge waveguide for the compact RR, as shown in Figure 27 (a). With the same layer stack of the shallow etched waveguide, both sides of the waveguide are etched until Q1.06 layer by a dry etch technique. Figure 27 (b) shows the electric field profile of the fundamental TE mode in the waveguide. As Figure 26 (b), n.i.d. InP suppresses the mode overlap in the p-InP to reduce the waveguide loss.

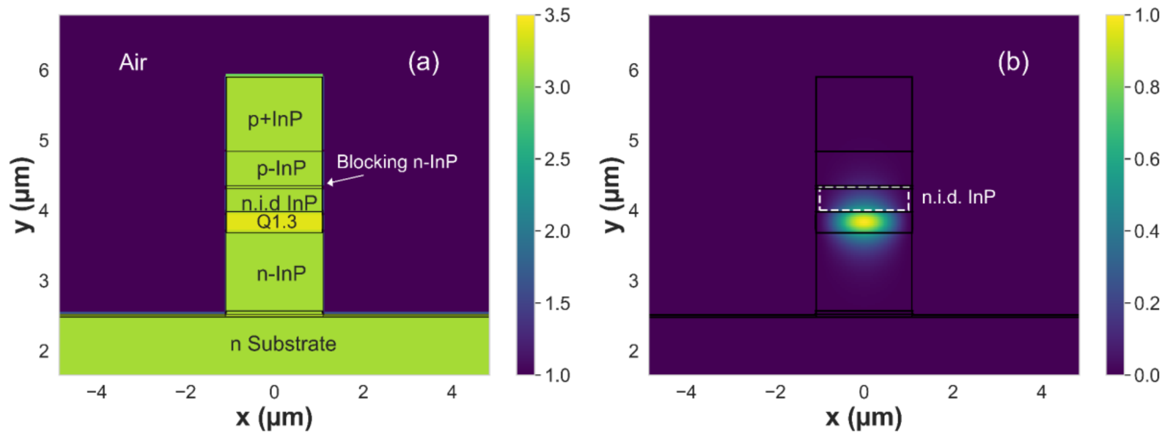

Figure 27 (a) Index distribution of the deep etched waveguide with the n.i.d. InP and a blocking n-InP. (b) Electric field profile of the waveguide with the fundamental TE mode.

Figure 28 shows calculated waveguide losses of the shallow and deep etched waveguide with varied layer heights of the n.i.d. InP. In a case without the n.i.d. InP, deep etched waveguide has the larger loss (10.3 dB/cm) than the shallowed (9.39 dB/cm) because more mode overlap in the p-InP waveguide. The shallow etched waveguide includes the longer Q1.3 layer containing more confinement in the layer, and thus the mode overlap in the p-InP is decreased. When the n.i.d. InP height increases, both waveguides reduce to around 3 dB/cm.

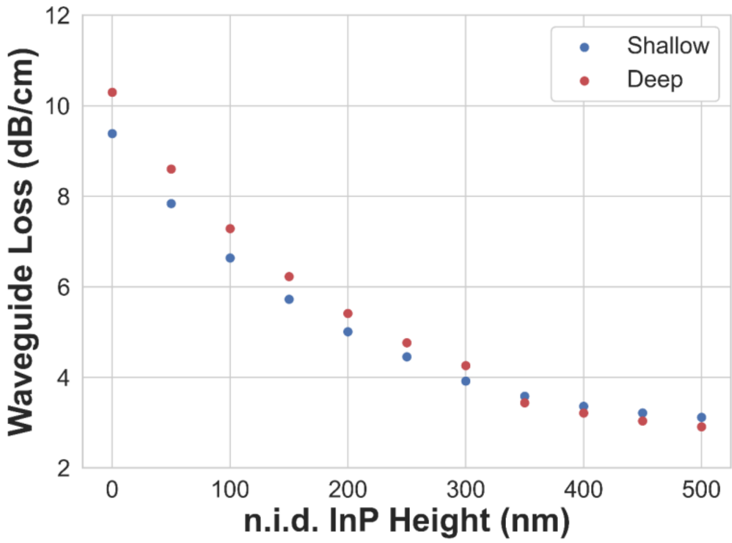

Figure 28 Waveguide loss of the shallow and deep etched waveguide with different height of the n.i.d InP layer.

The fabrication process of the waveguide requires a regrowth of the n.i.d. InP and the blocking layer, and an etch process. For the gain section, n.i.d. InP layer has to be removed for low series resistance. Therefore, the n.i.d. InP layer and the blocking layer are deposited on a whole wafer first and then selectively removed in the gain area. Accordingly, there is an offset between the active and passive sections. Figure 28 shows that increasing n.i.d. InP height improves the waveguide loss, however, this causes the large offset, resulting in issues in subsequent processes. The height of 350 nm is selected with losses of 3.58 and 3.44 dB/cm for the shallowed and the deep etched waveguide, respectively.

4.3.2. Waveguide transition

A transition component is designed to connect the shallow and deep etched waveguide, as shown in Figure 29. A structure with brown color depicts the waveguide mask, and the left side is for the shallow etched area (yellow), and the right side shows the deep etched area (blue). Both waveguides are coupled in the center with tapered structures to match mode field profiles. An inserted broadened rectangular structure provides a fabrication tolerance for misaligned masks for two different etch processes. Moreover, the rectangular is tilted 7° to avoid reflection from the index difference. W_s and W_d denote the waveguide width at the center position for the shallow and deep etched waveguide, respectively.

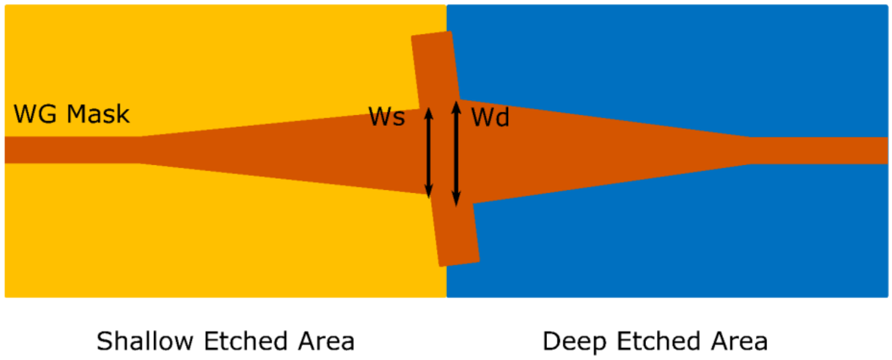

Figure 29 Schematic image of the transition structure to connect the shallow and deep etched waveguide.

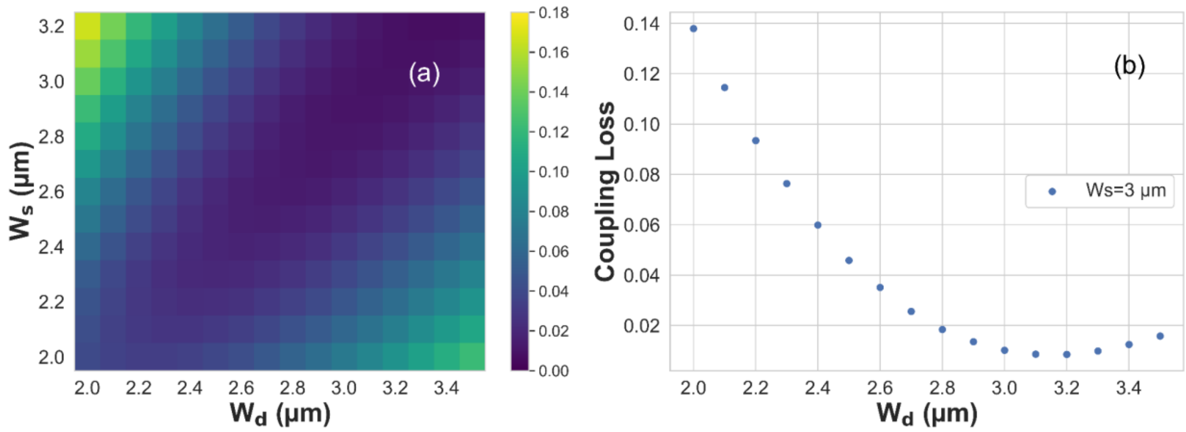

Figure 30 (a) Coupling loss from mode overlaps between the shallow and deep etched waveguide with varied waveguide widths. W_s and W_d denote the width of waveguides in Figure 29. (b) Coupling loss with different W_d at W_s = 3 μm.

Figure 30 (a) shows loss calculations between modes from the shallow and deep etched waveguide with different W_s and W_d by the mode solver [63]. In order to calculate the coupling loss, mode overlaps are simulated with TE mode profiles in both waveguides. This is simulated by a mode overlap calculation [90] with W_s and W_d from 2.0 to 3.2 μm and from 2.0 to 3.4 μm, respectively. The optimum W_d is slightly larger than W_s. For example, with W_s = 3 μm, coupling loss is minimum at W_d = 3.2 μm as shown in Figure 30 (b). As the width of both waveguides increases, the coupling loss is reduced, but the reduction is decreased gradually. Furthermore, the increased width requires a long taper waveguide, which enlarges the footprint of this component. Optimized W_s and W_d are 3 and 3.2 μm with a 100 μm taper waveguide to realize 0.008 coupling loss (0.035 dB). Considering the propagation loss of 3.5 dB/cm, the expected total loss of this component is 0.105 dB.

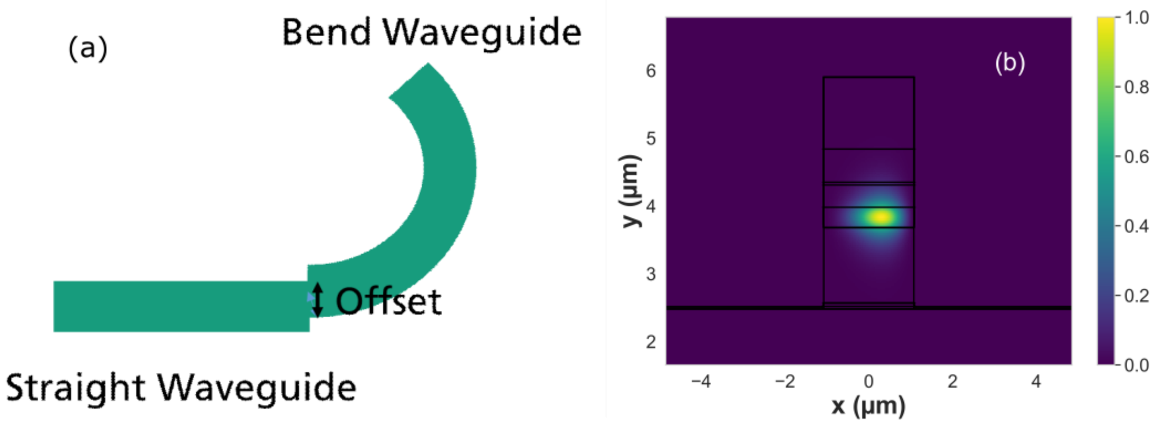

Figure 31 (a) Coupling the straight and bent waveguide with an offset.(b) Electric field profile of the waveguide with the fundamental TE mode in the bent waveguide.

A slight offset is designed to optimize a coupling between the straight and bent waveguide, as illustrated in Figure 31 (a) [91]. As stated above, the center of the electric field profile in the bent waveguide is shifted outward. Comparing the electric field profile in the straight waveguide as shown in Figure 27 (b), Figure 31 (b) shows an electric field profile with same parameters of Figure 27 (b), but this is bent with 80 µm. It is clear that the center of the profile is shifted to right side with around 0.3 µm. In a case without the offset, different positions of mode profiles in the straight and bent waveguide causes the coupling loss, which is calculated as 0.293 dB. When the offset is designed with 0.156 µm to match the mode overlap, coupling loss is reduced to 0.066 dB. The offset is smaller than the shift of the field profile of 0.3 µm, due to the asymmetric profile in the bent waveguide. Figure 32 shows calculated offsets with different radii of the bent waveguide. The optimization is based on finding the minimum coupling loss between mode profiles in the straight and bent waveguide. As the radius increases, the optimized offset decreases because the profile shift is reduced. All subsequent joint between the straight and the bent waveguide is determined based on Figure 32.

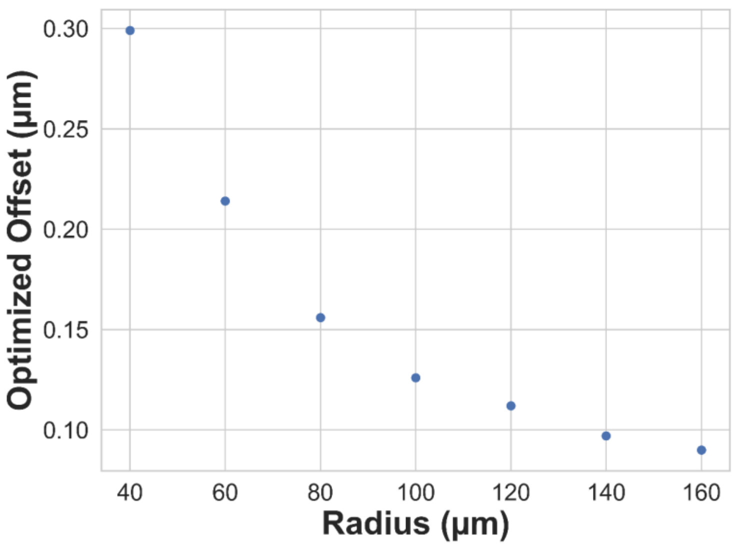

Figure 32 Optimized offset length with different radii. The offset is calculated to obtain the minimum coupling loss between the straight and bent waveguide.

4.3.3. MMI

Directional couplerss (DC) and MMIs are widely used as waveguide couplers of RRs. DCs use evanescent coupling between waveguides by beating odd and even modes [92]. DCs are preferred for the silicon platform because of their low loss, low back reflection, and ease of controlling the coupling ratio, despite difficulty demonstrating a small gap between two waveguides. However, DCs for the InP platform require the shallow etched waveguide to realize the compact size, and hence a transition is needed to connect the deep etched waveguide.

MMI is a coupler based on multimode interference [93], [94], consisting of input and output ports with a multimode waveguide, as shown in Figure 33 with design parameters. The MMI is designed based on the same layer stack of the deep etched waveguide. When the phase is matched with optimized design parameters, interference in the multimode waveguide divides light from the input port (port 1) to output ports (port 3 and 4) by 50:50, as shown in Figure 34 (a). Structure parameters for the MMI in Figure 34 (a) are Gap = 1 µm, W_{mmi} = 12.3 µm, W_{wg} = 2.3 µm, and $L_{coupler}$ = 208 µm. Figure 34 (b) shows simulated transmissions from port 1 to port 3 and 4. The optimum $L_{coupler}$ is 208 µm for transmissions of port 3 and port 4 with 0.457 and 0.467, respectively. The calculated loss of the device is 0.34 dB. The field profile and transmissions of Figure 34 are simulated by [63].

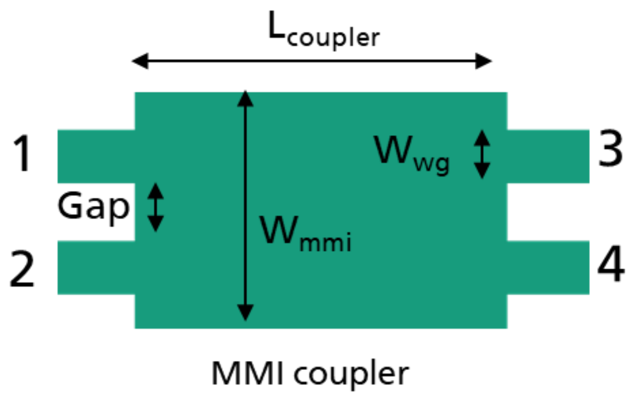

Figure 33 Schematic image of the MMI coupler.

Furthermore, different structure parameters can realize the 85:15 coupler, as shown in Figure 35. With the same simulation condition of the 50:50 MMI, optimized parameters for the 85:15 coupling are W_{mmi} = 8.2 μm and $L_{coupler}$ = 138 μm. Figure 35 (a) shows the electric field profile, including the light source from port 1. After passing through the multimode waveguide, light is coupled to port 3 with 15%, and port 4 with 85%. Calculated transmissions to port 3 and 4 are shown in Figure 35 (b). With the optimum $L_{coupler}$ = 138 μm, transmissions are 0.14 and 0.824 for port 3 and 4, respectively. The expected device loss is 0.16 dB. Table 3 shows detailed parameters of the 50:50 and 85:15 MMI.

Table 3 Detailed parameters of MMIs

	Gap	**W_{mmi}**	**W_{wg}**	**$L_{coupler}$**	**Loss**
50:50 MMI	1.8 μm	12.3 μm	2.3 μm	208 μm	0.34 dB
85:15 MMI	1.8 μm	8.2 μm	2.3 μm	138 μm	0.16 dB

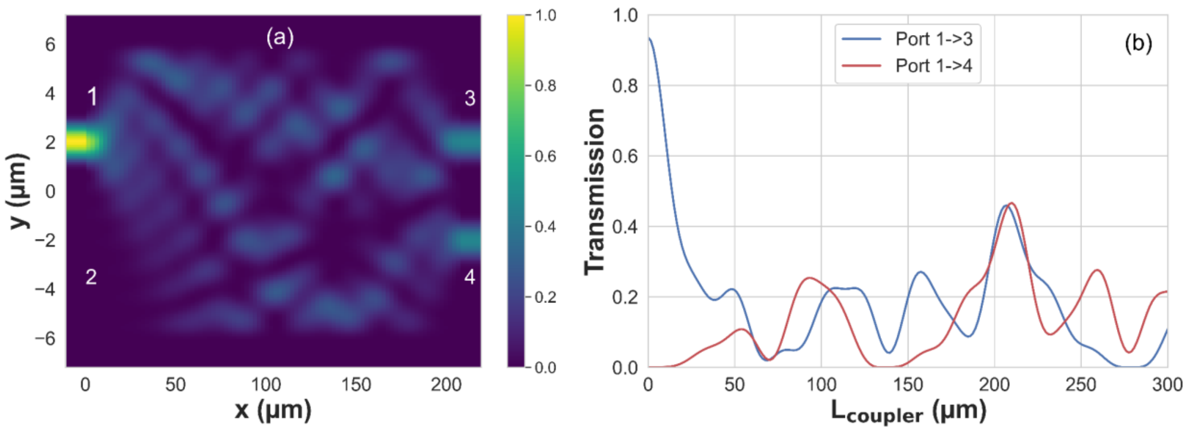

Figure 34 (a) Electric field profile in 50:50 MMI coupler. Source is started in the port 1 with fundamental TE mode. (b) Calculated transmission from port 1 to port of 3 (blue) and 4 (red).

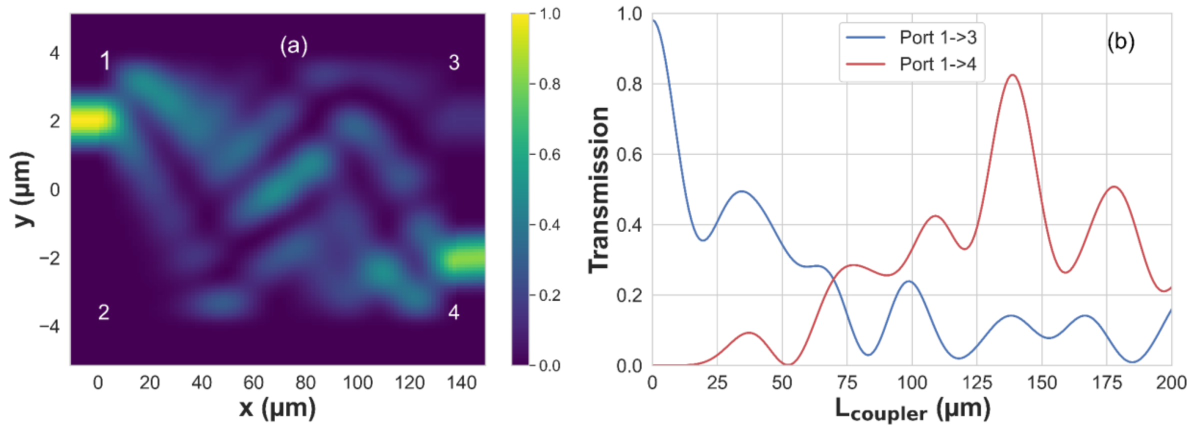

Figure 35 (a) Electric field profile in 85:15 MMI coupler. (b) Calculated transmission from port 1 to port of 3 (blue) and 4 (red).

4.3.4. Ring resonator

The RR consists of two couplers with a loop structure based on the deep etched waveguide, as shown in Figure 36 [55], [95]. A light source from port 1 couples to the loop and passes in the loop with multiple round-trips. Hence, constructive and destructive interference are generated according to the phase condition, and only wavelengths satisfying constructive interference pass to port 2. The light that does not match the phase condition passes through the MMI1 and is coupled out to port 3. In other words, the RR selects specific wavelengths to port 2 by the phase condition based on design parameters. The RR is widely used as a wavelength filter, e.g., an add-drop filter.

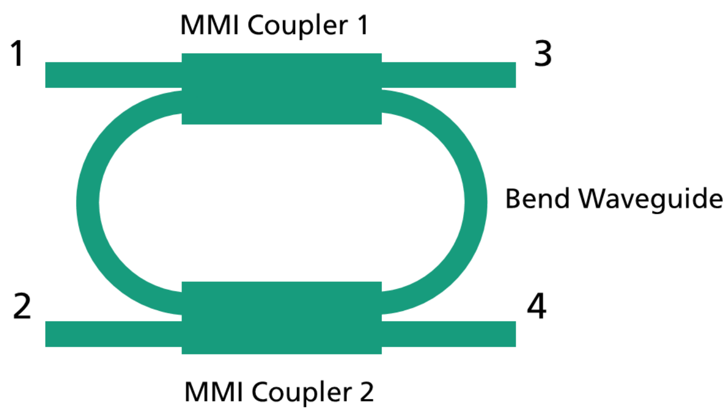

Figure 36 Schematic image of the RR.

Reference [48] reviewed the characteristic of the RR for the silicon platform, but the investigation can be applied to this InP RR. The characteristic is derived by assuming continuous wave operation and matching fields. The transmission from port 1 to port 2 (T_{12}) and 3 (T_{13}) is given by [55],

$$T_{12} = \frac{T_2}{T_1} = \frac{(1 - r_1^2)(r_2^2 - r_2^2)a}{1 - 2r_1r_2acos\emptyset + (r_1r_2a)^2}, \tag{4-1}$$

$$T_{13} = \frac{T_3}{T_1} = \frac{r_2^2a^2 - 2r_1r_2acos\emptyset + r_1^2}{1 - 2r_1r_2acos\emptyset + (r_1r_2a)^2}, \tag{4-2}$$

where $\emptyset$ is the phase shift, which is determined by a multiplication of the propagation constant (β) and of the round trip length of the loop (L). r_1 and r_2 denote the coupling coefficient of the MMI1 and MMI2, respectively. a is the amplitude transmission with the propagation loss of bent waveguides and couplers, as $a^2 = \exp(-\alpha L)$, where α is the attenuation factor in 1/cm. When the coupled power is equal to the loss ($r_2 = ar_1$), zero transmission in T_{13} at the resonance wavelength occurs, namely a critical coupling.

From (4-1) and (4-2), FWHM of T_{12} can be derived as,

$$FWHM = \frac{(1 - r_1r_2a)\lambda_{res}^2}{\pi n_g L\sqrt{r_1r_2a}}, \tag{4-3}$$

where λ_{res} denotes the resonance wavelength.

FSR is the essential parameter, especially for the Vernier effect. FSR of the RR is determined by group index and the length of the loop similar to (2-13), which is:

$$FSR = \frac{\lambda^2}{n_g L}. \tag{4-4}$$

Due to the fixed length of the MMI coupler, the circumference of bent waveguides determines the FSR from (4-4). For the FSR of 50 and 100 GHz, L sets 1665.4 and 832.7 µm with n_g = 3.59 at λ =1.55 µm. With the $L_{coupler}$ = 208 µm of the 50:50 MMI coupler, the corresponding radius is 198.9 and 66.3 µm. In the case of the radius for 50 GHz, the total length is 1664.5 µm, and the expected propagation loss is 0.583 dB with the waveguide loss of 3.5 dB/cm. However, this extended length is sensitive to the propagation loss, so even if the loss increases a little, the overall loss of the RR increases significantly. As the radius of the bent waveguide decreases, the electric profile tends to shift outwards. The radius of 66.3 µm for the 100 GHz has a risk of significant loss from a sidewall roughness because the profile is very close to the sidewall. In order to avoid losses from the radius that is too large or too small, the radius of 85.5 µm is selected with corresponding the FSR of 85 GHz (0.68 nm).

Figure 37 shows calculated transmission spectra for T_{12} and T_{13} from (4-1) and (4-2). MMI1 and 2 are assumed 50:50 couplers, corresponding r_1 and r_2 = 0.707. a is 0.953, including the waveguide loss and coupler loss of 3.5 dB/cm. Material dispersions of the waveguide is also included, and n_g = 3.59 at 1.55 µm. L is optimized with 979.5 µm, having two 208 µm MMIs and 85.5 µm bent waveguides. The transmission spectrum of T_{12} from port 1 to 2 is shown in Figure 37 (a). Only wavelengths satisfying the constructive interference transmit to port 2, and the peak spacing is 0.68 nm. The calculated FWHM is 0.167 nm, and the Q factor is 9289 at 1.55 µm from $Q = \lambda_{res}/FWHM$. The maximum transmission at resonance wavelengths is 0.85 and the minimum is 0.11. After passing through the RR, wavelengths matching the constructive interference couples to port 2 with FSR = 0.68 nm. In the SG DBR RR laser, the filtered wavelengths are resonated in the laser cavity only, which acts as the predetermined wavelength channels. Figure 37 (b) shows the spectrum of T_{13} from port 1 to 3. The maximum transmission is equal to Figure 37 (a), but the transmission at resonance wavelengths is almost zero because this close to the critical coupling (r_2a=0.668 and r_1=0.707). However, this low transmission is not suitable for the SG DBR RR laser because the laser's output is coupled to the RR. If the RR has this zero transmission for T_{13}, most light in the laser cavity cannot couple out, and the power of the laser is significantly lowered.

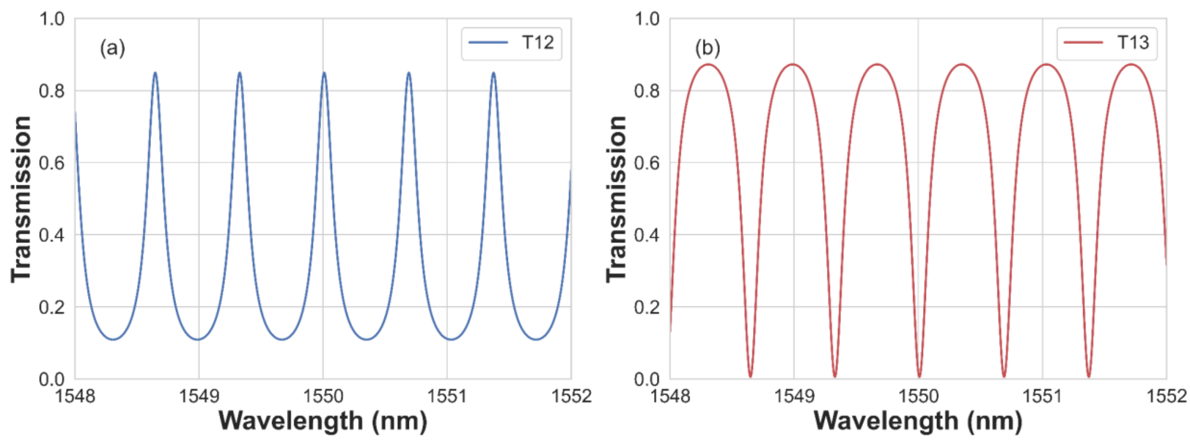

Figure 37 Transmission spectra of the RR wtih 50:50 MMI couplers from port 1 to 2 (a) and 3 (b).

To increase the transmission of T_{13} at resonance wavelengths, MMI1 and 2 are designed with different coupling ratios to avoid the critical coupling. Figure 38 (a) and (b) show calculated T_{12} and T_{13} with the same simulation condition of Figure 37, but MMI1 is replaced from the 50:50 to the 85:15 MMI coupler. In this case, T_{12} shows the transmission of 0.73 and 0.25 for the maximum and minimum with FSR = 0.68 nm as shown in Figure 38 (a). Comparing the zero transmission at resonance wavelengths of Figure 37 (b), T_{13} shows the minimum transmission is 0.15 and the maximum is 0.73 as shown in Figure 38 (b). Because of the increased transmission, the laser can operate with enough output power. The calculated loss of the RR is 0.56 dB.

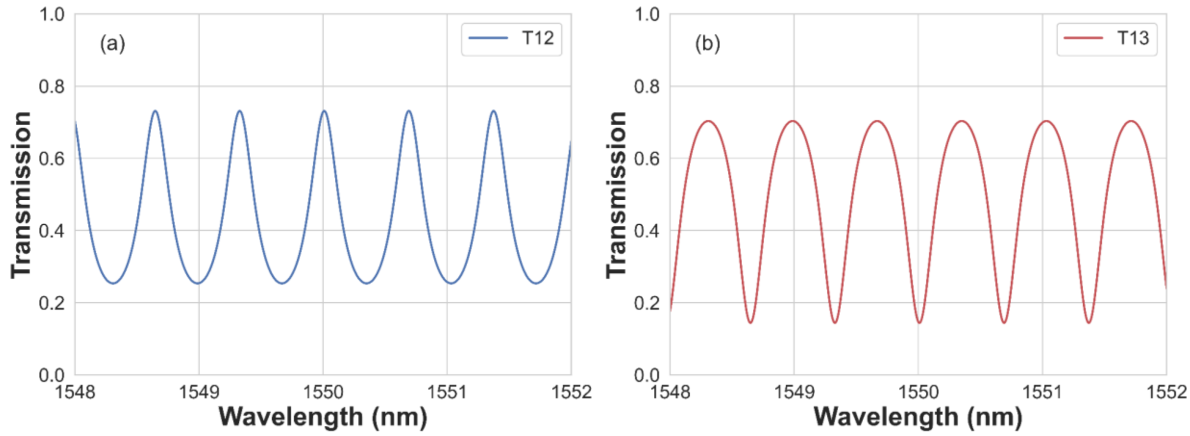

Figure 38 Transmission spectrum of the RR wtih 85:15 MMI1 and 50:50 MMI2 couplers from port 1 to port 2 (a) and 3 (b)

4.3.5. SG DBRs and a RR

As stated in 4.2, SG DBRs are optimized for the SG DBR RR laser to cover a wide tuning range with high reflections for both SG DBRs, while typical SG DBR lasers use the lower front reflection than the rear SG DBR. FSRs of SG DBR1 and 2 ($\Delta\lambda_1$ and $\Delta\lambda_2$) are 5.43 and 4.95 nm, respectively, and the tuning range from the Vernier effect is 54 nm. The SG DBR1 contains Z_0 = 61.3 μm, Z_1 = 6.2 μm, and N= 13. The rear SG DBR includes Z_0 = 67.5 μm, Z_1 = 6.2 μm, and N = 12. Both SG DBRs use Λ = 242.39 nm to match the center of the wavelength at 1550 nm. Figure 39 (a) shows overlapped reflection spectrum of SG DBRs and the transmission of the RR. Reflection spectra of SG DBRs are calculated by the TMM, and the RR's transmission is simulated by the exact condition of Figure 38 (a). To focus on the RR's effect, calculated wavelengths are limited to 20 nm. Figure 39 (b) shows the multiplication of all spectra in Figure 39 (a). Because the RR's FSR is not matched to the second strongest peak of SG DBRs, peaks in 1545 and 1555 nm are suppressed. As discussed in chapter 3.3.2, the significant difference between the central and the second strongest peak in Figure 39 (b) provides large SMSRs for the laser.

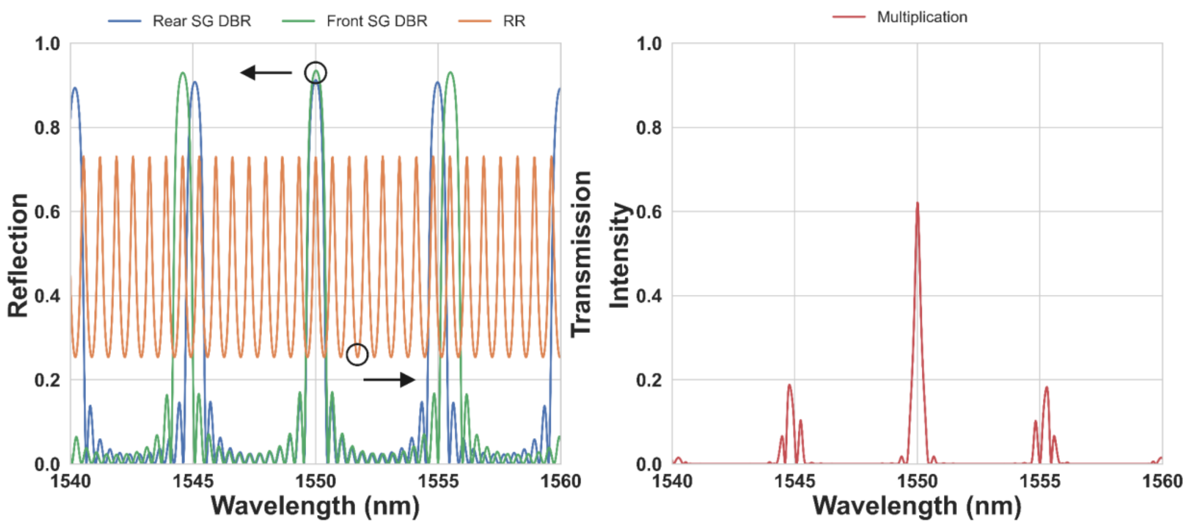

Figure 39 (a) Reflections and the transmission spectra of SG DBRs and the RR, respectively. The RR is calculated with same simulation condition of Figure 38 (a).

Furthermore, the typical SG DBR laser is designed as a reference laser to compare performances of the SG DBR RR laser. The reflection of the front SG DBR is 71.4%, but other design parameters are equal to the SG DBR RR laser. Table 4 summarizes detailed parameters of the SG DBR and SG DBR RR laser.

Table 4 SG DBR design parameters for SG DBR and SG DBR RR laser

	SG DBR Laser		**SG DBR RR Laser**	
	Front SG DBR	**Rear SG DBR**	**SG DBR1**	**SG DBR2**
Z_0	61.3 μm	67.5 μm	61.3 μm	67.5 μm
Z_1	6.2 μm	6.2 μm	6.2 μm	6.2 μm
N	8	12	13	12
L_{SG}	435.6 μm	749.2 μm	742.4 μm	749.2 μm
R_{max}	71.4%	90.7%	93.1%	90.7%
Λ	242.39 nm			

4.4. Experiment

Figure 40 shows microscope images of the developed SG DBR RR laser, including two SG DBRs, gain, phase, and RR, as shown in Figure 24(b). The lengths of two SG DBR sections are 800 μm, the gain is 400 μm, and the phase is 150 μm. SG DBR1 and gain are located at the top, and SG DBR2 and phase are at the bottom. The RR includes 85:15 and 50:50 MMI couplers with 85.5 μm bent waveguides, connecting components at the top and bottom. The gain section consists of MQWs with different PLs to cover long wavelength ranges. The connection between the gain and passive sections is equal to Figure 11 by the offset QW. The RR uses the deep etched waveguide, but other passive sections are based on the shallow etched waveguide with the n.i.d. InP layer. For the fabrication, the additional n.i.d. InP is regrowth on the whole wafer and then selectively removed in the gain section to realize low series resistance on the gain. The SG DBR RR laser is based on the shallow etched waveguide, but the RR uses the deep etched waveguide. The transition component couples two different waveguides. The footprint of the laser is 2.5 x 0.3 mm.

Furthermore, the typical SG DBR laser is demonstrated as shown in Figure 41, including the front SG DBR, gain, phase, and the rear SG DBR. The lengths of the sections are 500 µm, 400 µm, 150 µm, and 800 µm, respectively, and the footprint is 2.5 x 0.25 mm. The layer stack equals the SG DBR RR laser because the laser is realized on the same wafer. Contact pads are designed to use a multi-needle probe for applying currents on each section for both lasers. Two output ports are designed to couple out laser power from 85:15 MMI coupler on the top (port A), and 50:50 MMI coupler on the bottom (port B). Waveguides at the end of facets are tilted 7° and anti-reflection coated to avoid reflection from the facet between the waveguide and the air.

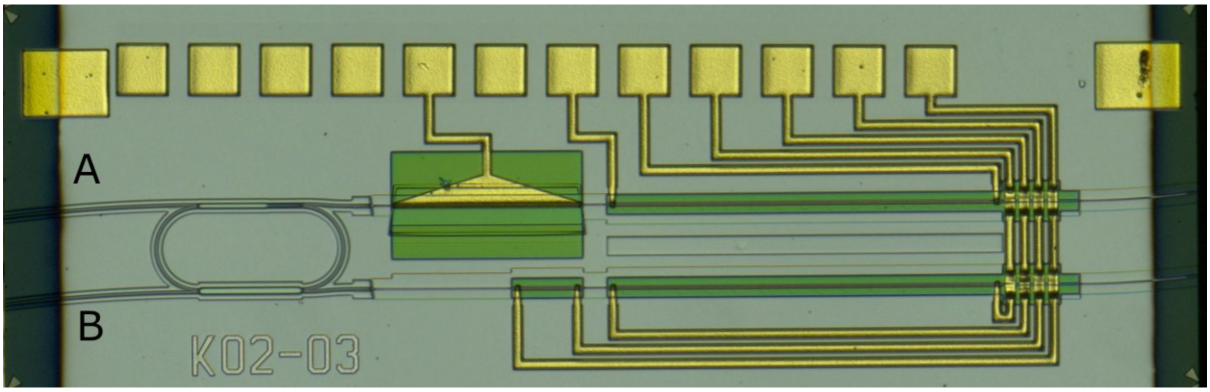

Figure 40 Microscope image of the SG DBR RR laser.

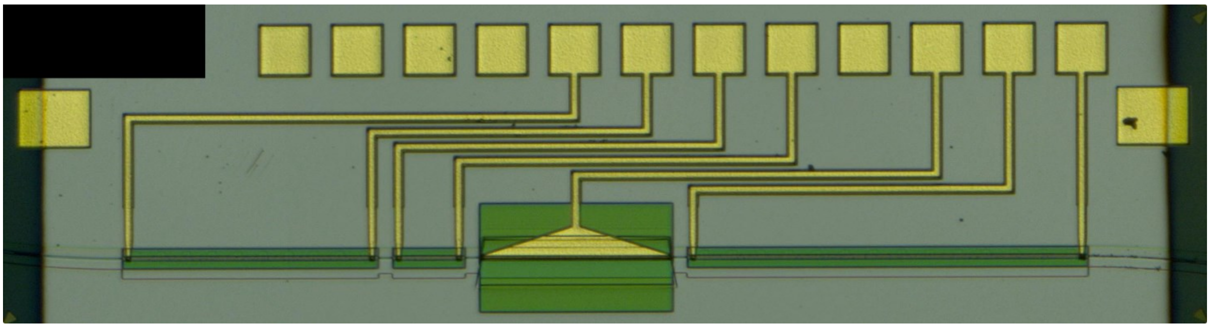

Figure 41 Microscope image of the typical SG DBR laser.

4.4.1. Pulsed PI measurement

Lasers are mounted on an Au-coated heat sink to realize a good heat dissipation and use a TEC to stabilize the temperature at 20°C. Figure 42 (a) and (b) show pulsed PI measurement with an integrating sphere on the output ports from the left facet for the SG DBR RR and the SG DBR laser. For the measurements, no current is applied to tuning sections. The SG DBR RR laser shows a threshold current of 71.9 mA and power of 4 mW with a gain current of 150 mA. In the same measurement condition, the threshold current of the SG DBR laser is 50.4 mA, and power is 7.7 mW. Measured voltages are 1.41, and 1.56 V at 150 mA gain current for the SG DBR RR and SG DBR laser, respectively. Such voltages are lower than 3.2 V from the SG DBR laser based on the foundry process (see Figure 16) because this work uses the n-substrate, which realizes the improved series resistance than the foundry process' Fe-doped substrate.

The larger threshold current of the SG DBR RR laser comes from the integrated RR, which couples out more power than the SG DBR laser. In contrast to the SG DBR laser based on 71.4% and 90.7% mirrors, the SG DBR RR laser includes 93.1% and 90.7% mirrors but the RR couples out 50% and 15% out of the cavity. To reach the threshold condition, the SG DBR RR requires more gain to compensate for the power coupling to outside of the cavity by the RR.

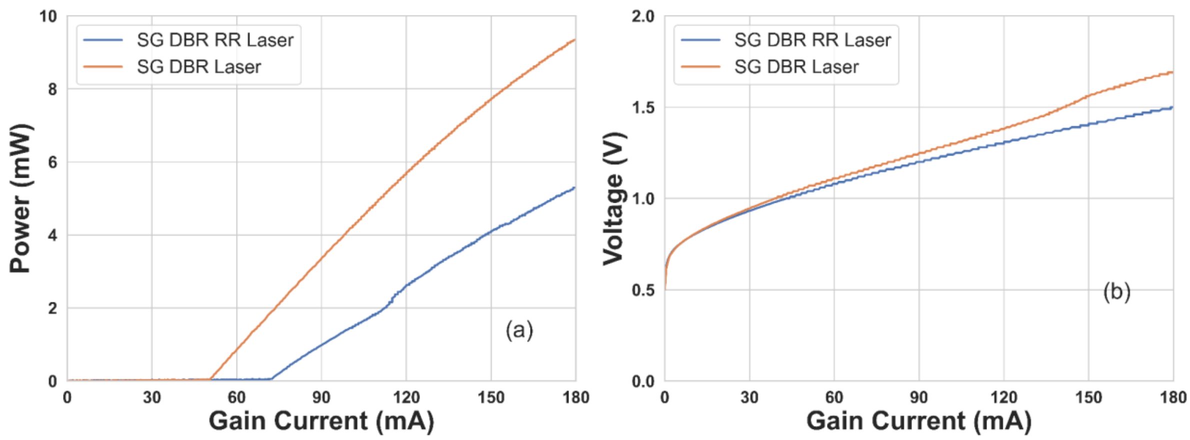

Figure 42 (a) Pulsed PI measurement of the SG DBR RR and SG DBR laser. (b) Voltage measurement.

However, the 50.4 mA threshold current of the SG DBR laser is still much higher than the 20 mA of the similar laser based on the foundry process in 3.3.1 (see Figure 16). Hence FP lasers are investigated with the equal cavity lengths based on the foundry process and this work, as shown in Figure 43 (a). Measured threshold currents are 23 and 22.6 mA, and output powers are 18.8 and 6.93 mW at the gain current of 150 mA for the foundry process and this work, respectively. The foundry process uses MQWs with identical QWs, whereas this work uses two different QWs for the MQWs. Even though both FP lasers show similar threshold current, the output power of the foundry process lasers is clearly higher. This can be explained by the fact that the different QWs in this work lasers amplify a much wider wavelength range and thus effectively reduce the power efficiency at the laser wavelength.

Figure 43 (b) shows the corresponding voltages. As aforementioned, this work uses the n-substrate and the Zn diffusion during the p-InP deposition, while the foundry process is based on the Fe-substrate and the selectively Zn diffusion process. Therefore the series resistance in the gain section of this work shows improved than the foundry process.

Whereas the threshold conditions are similar for both FP lasers, the SG DBR laser from this wafer exhibits a larger threshold current than the foundry process device. Consequently, this difference must be caused by higher optical losses in the passive sections. A primary reason for the unexpected high loss is the used thin n-InP blocking layer, which is most likely too thin to prevent the Zn diffusion into the underlying material. If this layer does not effectively block Zn-diffusion, Zn can penetrate into the n.i.d. InP and Q1.3 layer also. In this case, the increased p-doping causes huge losses, as calculated in Figure 7. In order to solve this issue, the next generation can use the thicker blocking layer or replace the whole n.i.d. InP with n-InP despite of expense of the doping loss.

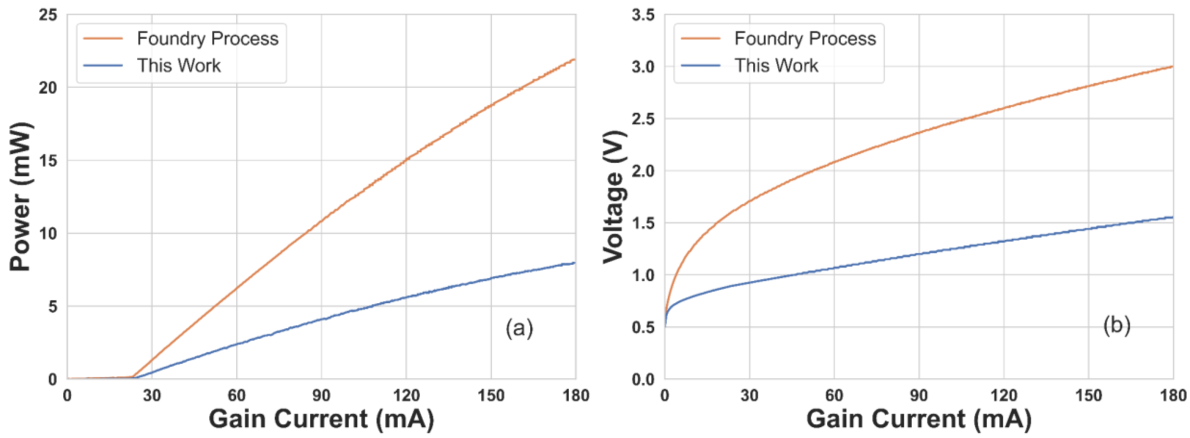

Figure 43 (a) Pulsed PI measurement of FP laser with 400 µm for based on the foundy process and this work. (b) Voltage measurement.

4.4.2. Wavelength tuning performance

To characterize the optical performance of lasers, the same measurement condition is used as stated in 3.3.2. The TEC is set to stabilize the temperature at 20°C, and the tapered fiber is used to collect light from port B. First, optical spectra are investigated from port A and B with different gain currents. Figure 44 (a) shows the spectrum with 40 mA on the gain section at port A, coupled with the 85:15 MMI coupler. The applied current is below the threshold condition, which emitted the ASE only, not a laser spectrum. The ASE from the gain section passes through the RR and is coupled out by port A. Hence the spectrum is similar to Figure 35 (b), which shows the intensity filtered out resonance wavelengths. The measured FSR of the ASE spectrum is 0.685 nm, which is close to the simulation result of 0.68 nm. When the gain current is 150 mA over the threshold current, the stimulated emission is measured at 1562.7 nm, as shown in Figure 44 (b).

The optical spectrum at port B is free from the most ASE because only light matching the coincidence of two SG DBR and the RR could be emitted. The optical spectrum with 40 mA on the gain section as Figure 45 (a) shows the small intensity at 1562.7 nm. Figure 45 (b) shows the stimulated emission at 1562.7 nm with 150 mA, which is over the threshold condition. All subsequent measurements use port B with free from the ASE.

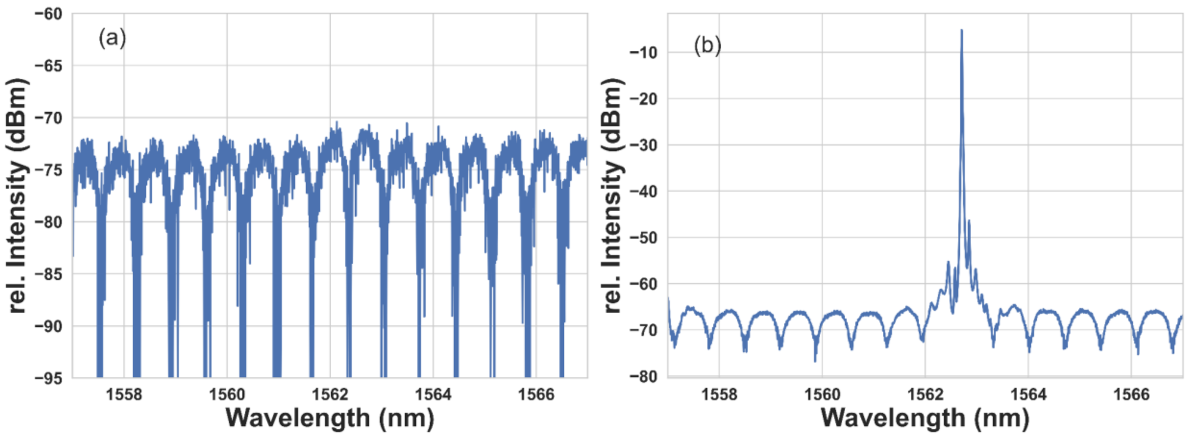

Figure 44 Optical spectrum of the SG DBR RR laser from port A with the gain current 40 mA (a) and 150 mA (b).

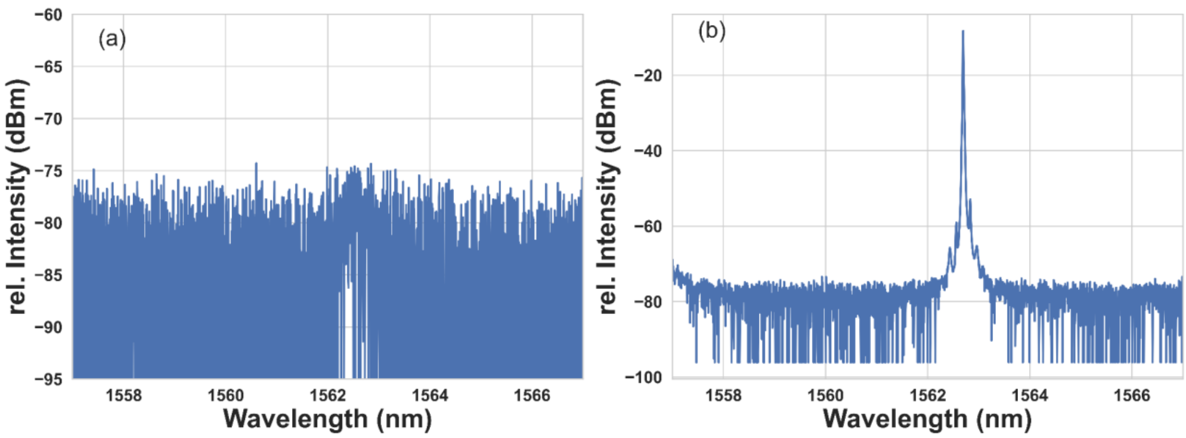

Figure 45 Optical spectrum of the SG DBR RR laser from port B with the gain current 40 mA (a) and 150 mA (b).

The wavelength tuning is investigated by controlling heaters on two SG DBRs with different powers from 0 to 0.7 W with an interval of 0.02 W for the SG DBR and SG DBR RR laser, as shown in Figure 46 (a) and (b), respectively. Wavelength maps show peak wavelengths from optical spectra. The gain current of 150 mA is applied to the gain section, and no current is applied to the phase section.

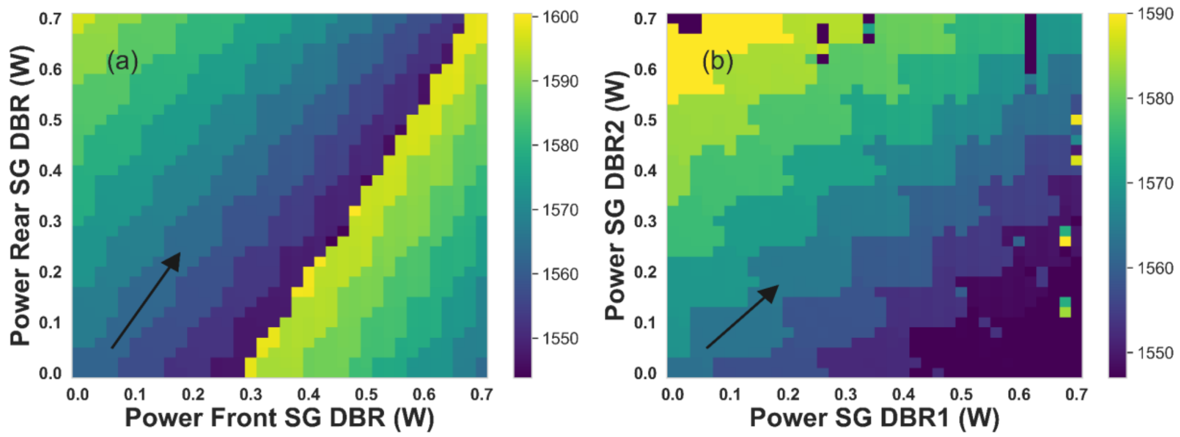

Figure 46 Measured wavelength mapping at current of 150 mA on gain section for the SG DBR (a) and SG DBR RR laser (b). Arrows point out a tuning direction to tune both SG DBRs with same tuning power.

Arrows in Figure 46 (a) and (b) point out the direction to tune both SG DBRs with the same powers in the unit length, which indicates that both SG DBR reflections shift by equal wavelengths for the SG DBR and SG DBR RR laser, respectively. As discussed in 3.2.3, tuning on both SG DBRs by same wavelength can shift the coincidence wavelength linearly, but discrete manner with the cavity mode spacing. The slope of the arrow in Figure 46 (a) is 8/5, which stems from the ratio between 500 and 800 µm for the front and rear SG DBRs length, respectively. The SG DBR RR has identical lengths of SG DBRs (800 µm) for SG DBR 1 and 2, and hence the slope is 8/8.

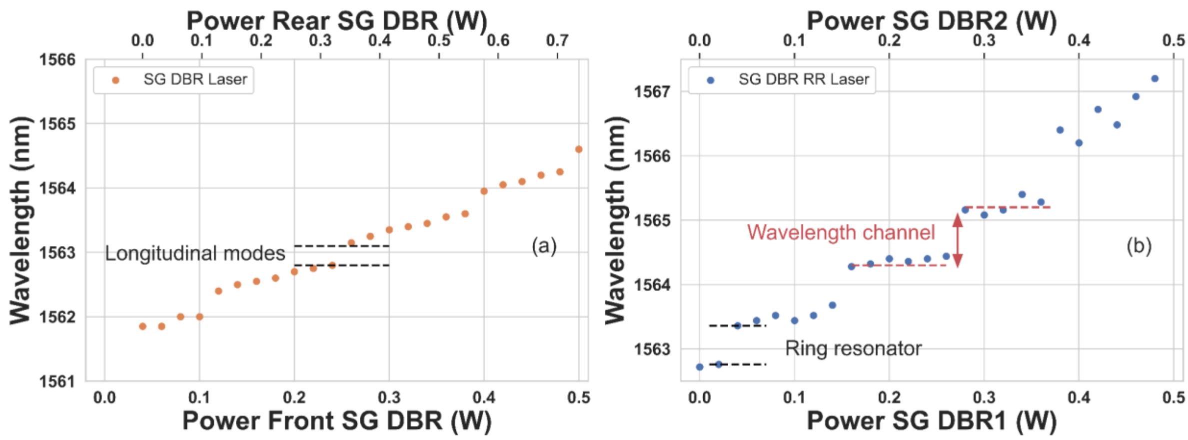

Figure 47 (a), (b) Mode jump behavior following arrows in Figure 46. (a) Peak wavelengths width different heater powers on SG DBRs of the SG DBR laser. (b) for SG DBR RR laser. Two SG DGBRs are controlled to match equal heater powers in the unit length.

Figure 47 (a) and (b) show peak wavelengths following the arrows in Figure 46 (a) and (b) for the SG DBR and SG DBR RR laser, respectively. In Figure 47 (a), heat powers of the front and rear SG DBRs are ramped up from 0.04 to 0.5 W and 0 to 0.736 W, respectively. The increase of powers for the front SG DBR is 0.46 W and the rear is 0.736 W, which are equal to the ratio of 8/5. The mode jumps occur with continuous increase of 0.28 nm and mode jump of 0.36 nm, repeatedly. The continuous tuning comes from thermal crosstalk from heaters of SG DBRs to the laser cavity. When heater powers are ramped up, the temperature of the cavity is also increased, resulting in shift of cavity modes. Hence, the continuous shift and the jump are repeated in the tuning behavior. The mode jump indicates the FSR of cavity modes, but the measured value of 0.36 is extended than the expected spacing of 0.27 nm from (3-11) with design parameters in Table 4. It is described by the thermal crosstalk, when the mode jump occurs, cavity modes shifts simultaneously.

Figure 47 (b) shows mode jumps from the SG DBR RR laser with heater powers from 0 to 0.5 W for the SG DBR 1 and 2. Four mode jumps by the RR (black dashed lines) occurs during the heat variations, and the average value is 0.73 nm, which is extended value than the FSR of 0.685 nm from Figure 44 because of the thermal crosstalk as the SG DBR laser. As the mode jump behavior of the SG DBR laser, Figure 47 (b) shows continuous tuning and mode jumps repeatedly. After heater powers over 0.38 W, measured peak wavelengths increase linearly because of laser chip’s high temperature. The linear shift appears only in the SG DBR RR laser and not in the SG DBR laser due to the separation structure inserted between SG DBRs (see Figure 24 (b)). The etched area is designed to suppress the thermal crosstalk between two SG DBRs, but this degrades a thermal dissipation for the whole laser chip. Therefore, the influence of the thermal crosstalk by heater powers is significant, and the linear wavelength shift occurs. The average continuous tuning for the mode behavior is

0.17 nm before 0.38 W. Actual prefixed channels are determined by the average of continuous tuning (red dashed lines), not the jumps in the end (black dashed lines). As powers of heaters increase, the spacing between red dashed lines also increases because the whole laser's temperature is heated gradually. The average wavelength channel spacing is 0.83 nm until heat powers of 0.38 W.

The increase of the channel spacing is not proper for the concept of prefixed wavelength channels in the tuning range. Moreover, the linear wavelength shifts during high heat powers are also an issue in realizing the fixed channels. Both behaviors originate from the significant thermal crosstalk from the powers of heaters. Note that improved designs for waveguides can solve the issues. For example, [15] demonstrated a suspended waveguide with an etched area under the waveguide. Although the waveguide required complex fabrication for the etching, such a structure isolates thermal flow from the heater on the waveguide. The localized heat increases thermal efficiency for the tuning significantly and also reduces the thermal crosstalk due to the isolated thermal flow.

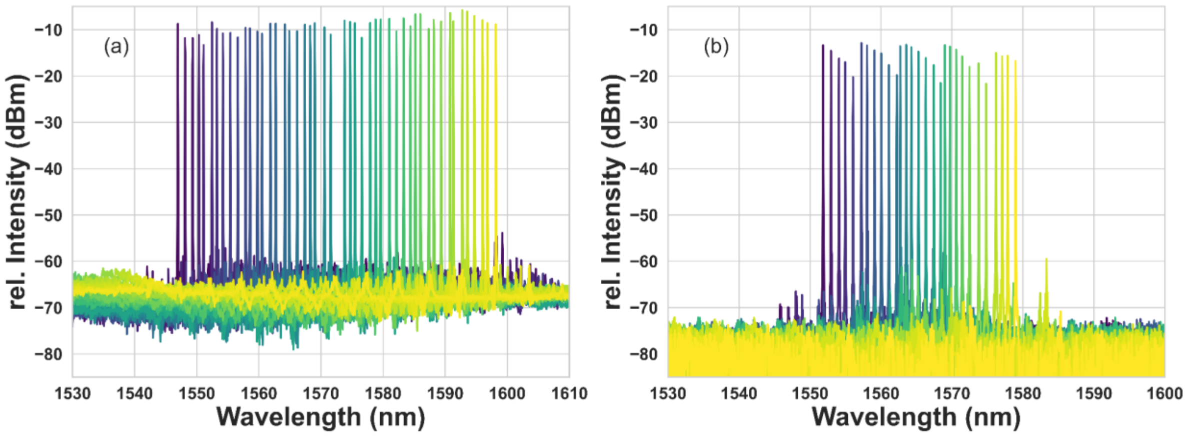

Figure 48 Optical spectra of the SG DBR laser (a) and SG DBR RR laser (b).

From Figure 46 (a), superposed optical spectra are shown in Figure 48 (a) for the typical SG DBR laser with 56 nm tuning range from 1544 nm to 1599 nm. The measured tuning range is well matched to the target value of 54 nm. Figure 48 (b) shows overlapped spectra, selected in the wavelength mapping of Figure 46 (b) for the SG DBR RR laser. The tuning range is 28 nm from 1552 to 1579 nm, which is reduced by 28 nm from the SG DBR laser. An expected reason for the small tuning range is the high loss in passive sections from the extended cavity caused by the Zn penetration. Due to the high loss in the cavity, the low gain region in the gain bandwidth away from the center did not receive enough gain. Furthermore, the high temperature of the chip degrades the phase matching condition of MMIs. As discussed in 4.3.3, constructive interference in the multimode waveguide divides electric field to the output ports. When the MMI is heated up due to the thermal cross talk, the condition for the constructive interference is mismatched, and thus loss is enlarged. The loss caused by the unwanted heat reduces the output power of the laser. As illustrated in Figure 12, the Vernier effect selects wavelengths by controlling the combination of both SG DBRs to find the coincidence, including wavelength jumps between peaks (Figure 12 (b) and (c)) and cavity modes (Figure 12 (d)). For the cavity mode jumps, thermal heater power shifts both reflection spectra over $\Delta\lambda$, which requires more powers than the jumps between peaks. Peak powers of spectra in Figure 48 (b) shows increase and decrease repeatedly, following heat powers on SG DBRs. For example, the initial coincidence wavelength without tuning on heaters is 1562.7 nm. When heaters are ramped up simultaneously (Figure 12 (d)), the peak wavelength is shifted with six channels until 1568.4 nm. During this ramping up, peak powers are decreased because of the increased loss from MMIs. Afterward, the next coincidence wavelength 1569 nm is selected by operating SG DBR 2 only (Figure 12 (b)) with heater power of 0.04 W. Due to the small heat power, the peak power at 1569 nm is increased again. The average FSR of 29 wavelength channels of Figure 48 (b) is 0.97 nm as shown in Figure 48 (b), which is extended than the target of 0.685 nm because of the thermal crosstalk.

SMSRs are shown in Figure 49, including over 42 dB and 39.7 dB for the SG DBR and SG DBR RR laser, respectively. Note that the fine tuning by using the phase section can improve the SMSRs.

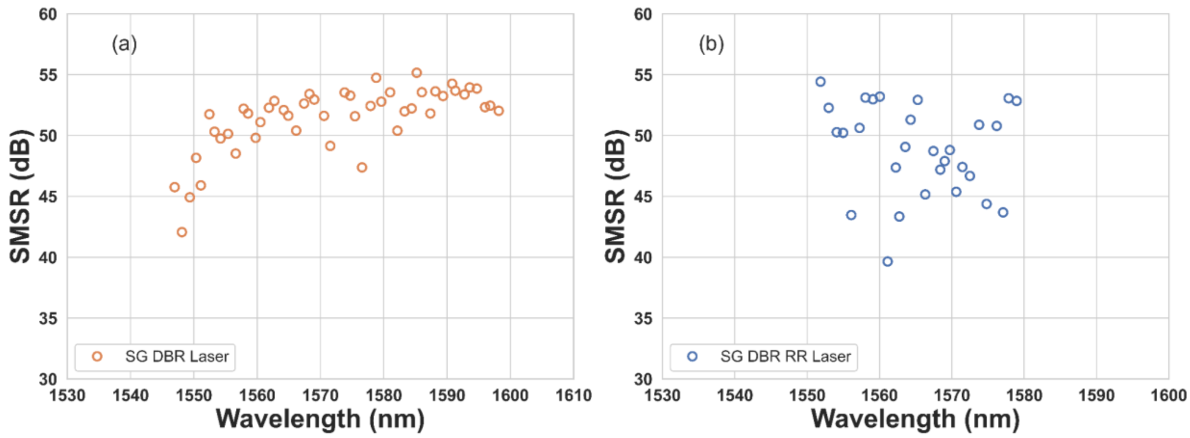

Figure 49 SMSRs of the SG DBR laser (a) and SG DBR RR laser (b), corresponding to spectra of Figure 48 (a) and (b).

Mode jump behaviors with different power on the phase section are measured for the SG DBR laser as shown in Figure 50 (a). Before the mode jump, continuous wavelength shift is measured about 0.4 nm, and the mode jump occurred with 0.28 nm. The mode jump came from the FSR of the cavity mode, which matched the predicted FSR of 0.27 nm from (3-11) with parameters as follow: $n_{g,active}$ = 3.8, $n_{g,passive}$ = 3.59, L_{gain} = 400 µm, and $L_{passive}$ = 790 µm. The fine tuning by the phase section covers the cavity mode spacing in Figure 47(a). Therefore, the quasi-continuous tuning is feasible to access all wavelengths in the tuning range by tuning on SG DBRs and the phase section. Figure 50 (b) shows the mode jump from the SG DBR RR laser with the continuous tuning of 0.2 nm and the mode jump of 0.095 nm. Such a jump is reduced by around one-third due to the extended cavity length from the RR. From (3-11), extracted $L_{passive}$ is 3099 µm, including all passive waveguide lengths.

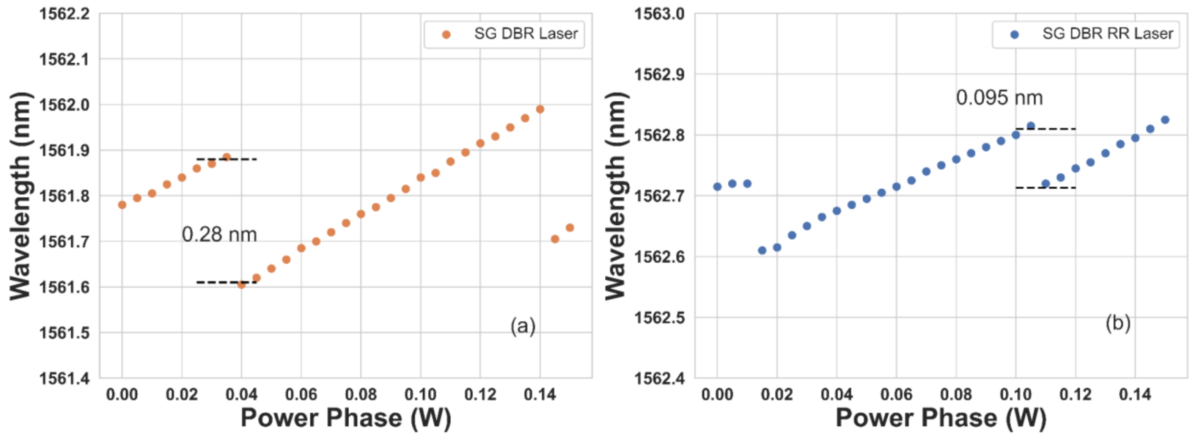

Figure 50 Mode jump with variant power on the phase section for the SG DBR (a) and SG DBR RR laser (b).

4.4.3. Linewidth measurement

Extended cavity structures are widely used to increase the length ratio between the active and passive length to demonstrate narrow linewidth lasers [59], [85]. As discussed in 3.3.3, ASE adds phase and index fluctuation to the laser mode. When the cavity's passive length is extended, the total number of photons in the cavity is enlarged, but spontaneous emission is limited in the relatively short active length. The ASE couples to the laser mode is reduced, and hence the noise is reduced. This mechanism is referred to as noise dilution for narrow linewidth [59].

Patzak [96] reported the Schawlow-Townes-Henry formula with a factor of the extended cavity, and Andreou [85] simplified this for the DBR laser with a RR, which is given by

$$\Delta\nu = \frac{h\nu v_g^2 n_{sp}\alpha_m(\alpha_i + \alpha_m)(1+\alpha_H^2)}{4\pi P}\frac{1}{C}\frac{1}{F^2}, \tag{4-5}$$

where C is a factor implying asymmetric mirror reflections, causing different power coupled out from the laser. The F is related to the extended cavity as

$$\mathrm{F} = 1 + \frac{n_{g,passive} L_{passive}}{n_{g,active} L_{active}}. \tag{4-6}$$

$L_{passive}$ is the total length of passive sections, including $L_{passive}$, L_{eff_SG}, and effective length of RR (L_{eff_RR}) and all waveguides for connecting each section. L_{eff_RR} is determined by the differential delayed phase at the resonance wavelength [97], which is typically not equal to the physical device length due to the resonance in RR. The F implies the noise dilution mentioned above, which includes the ratio between the active and passive sections. Note that the loss of waveguide limits the extended cavity length because enlarged $L_{passive}$ increases α_i and α_m simultaneously in (4-5). Reference [98] reported that the limitation is approximately the inverse of the passive waveguide loss. Calculated the $1/F^2$ factor for the SG DBR laser and the SG DBR RR laser are 0.12 and 0.014 with parameters in the previous chapter.

The proposed SG DBR RR laser is similar to the DBR laser with a RR, but the laser output is coupled out by RR. However, since the noise dilution is working in the same way, the linewidth improvement is realized in the SG DBR RR laser.

The optical linewidth is investigated based on the measurement setup as stated in 3.3.3. Figure 51 (a) shows the measured linewidth of the SG DBR and SG DBR RR laser with different wavelengths from 4.95 to 5.74 MHz and from 2.38 to 3.02 MHz, respectively. The linewidth is characterized by the Lorentzian fitting, which is shown exemplarily in Figure 51 (b) for 1567.26 (SG DBR laser, orange color) and 1569.06 nm (SG DBR RR laser, blue color). This linewidth result shows much broaden than 713 kHz in chapter 3.3.3. One reason is the expected loss in passive sections from the Zn penetration, which increases α_i and α_m in (4-5). Despite huge losses in passive sections, linewidth improvement is measured from 5.74 MHz to 3.02 MHz by 48%.

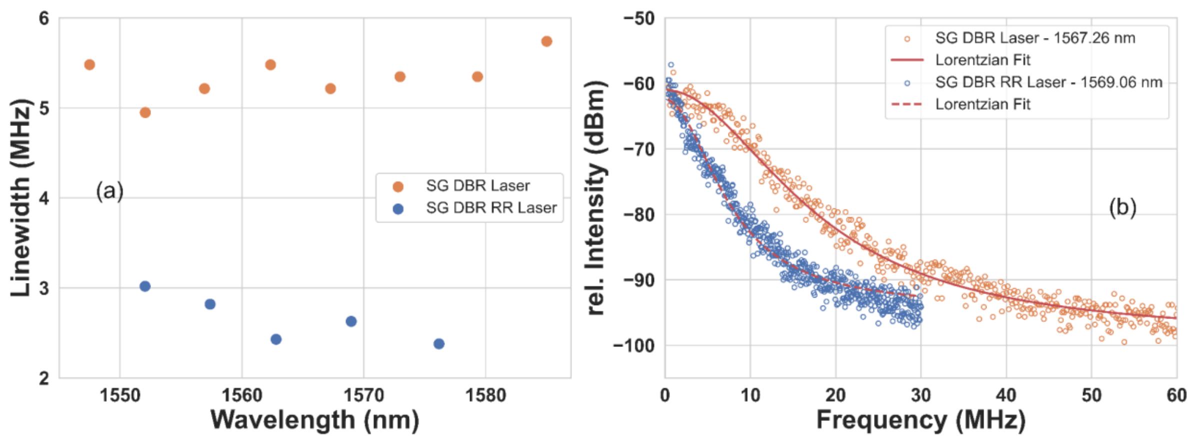

Figure 51 (a) Measured linewidth of the SG DBR laser and SG DBR RR laser, obtained with Lorentzian fitting. (b) ESA spectrum of two lasers with 1567.26 nm and 1569.06 nm, respectively.

4.5. Widely tunable SG DBR laser for 98 nm tuning range

A widely tunable SG DBR laser is demonstrated, which is designed for a 120 nm tuning range. This laser is designed as the SG DBR laser (see Figure 41), but SG DBRs are optimized with $\Delta\lambda_f$= 6.15 nm, $\Delta\lambda_r$ = 5.85 nm, and $\delta\lambda$ = 0.3 nm. Due to the optimization, maximum reflections of the front and rear SG DBRs is reduced to 36.3% and 60.8%. Table 5 shows detailed parameters of the widely SG DBR laser.

Table 5 SG DBR design parameters for the SG DBR laser with 98 nm tuning range

	SG DBR Laser	
	Front SG DBR	**Rear SG DBR**
Z_0	54.4 μm	57.2 μm
Z_1	2.79 μm	2.79 μm
N	10	15
L_{SG}	492.1 μm	802.9 μm
R_{max}	36.3%	60.8%
Λ	242.39 nm	

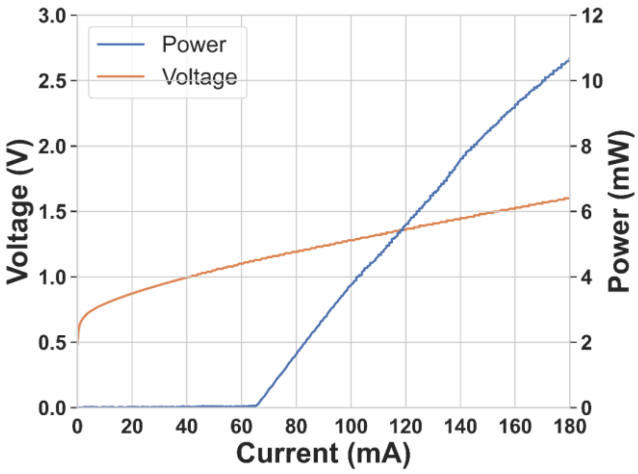

Figure 52 Pulsed PI measurement of the widely tunable SG DBR laser

Figure 52 shows a pulsed PI measurement at 20°C with different currents applied to the gain section. In this measurement, no currents are used to control passive sections. The measured threshold current is 67.5 mA and the output power at 150 mA is 8.42 mW. The threshold current is increased than the SG DBR laser for 56 nm tuning range because of low reflections of SG DBRs. The measured voltage is 1.485 V at 150 mA gain current.

The tuning map is characterized by the same measurement setup used above. Figure 53 (a) shows the tuning mapping with different power on the front and rear SG DBRs from 0 to 0.85 mW with the gain current 150 mA. The white color in the figure depicts areas that peak power of the optical spectrum is below -55 dBm. Due to the Vernier effect, the white area is for wavelengths below 1540 nm and over 1640 nm. Because of the low gain in the wavelength region, the stimulated emission cannot be achieved. A measured mode jump behavior is shown in Figure 53 (b) with different power on the phase section. The mode jump is 0.29 nm, corresponding to the cavity mode spacing, and a continuous tuning is about 0.3 nm. Selected superposed optical spectra and corresponding SMSRs from Figure 53 (a) are shown in Figure 54 (a) and (b). The measured tuning range is 98 nm from 1537 nm to 1635 nm and SMSRs over 38.3 dB. In comparison with the average SMSRs of 51.8 dB Figure 49 (a), this laser shows slightly lower average of 47.7 dB because of the reduced $\delta\lambda$.

For the linewidth measurement, the delayed self-homodyne method is used. Figure 55 (a) shows measured linewidths by Lorentzian fitting from 5.63 to 7.34 MHz. Moreover, this is exemplarily shown in Figure 55 (b) at 1561.15 nm with 5.63 MHz. The measured linewidth is slightly larger than the SG DBR laser in Figure 51 (a), because of low reflections of SG DBRs. The lower reflection keeps smaller number of photons in the cavity, and hence the linewidth is broaden.

In comparison with the SG DBR laser in 4.4, this laser shows significantly improved tuning range from 56 to 98 nm and small reduction of SMSRs by 4.1 dB. However, the linewidth is degraded due to the low reflections.

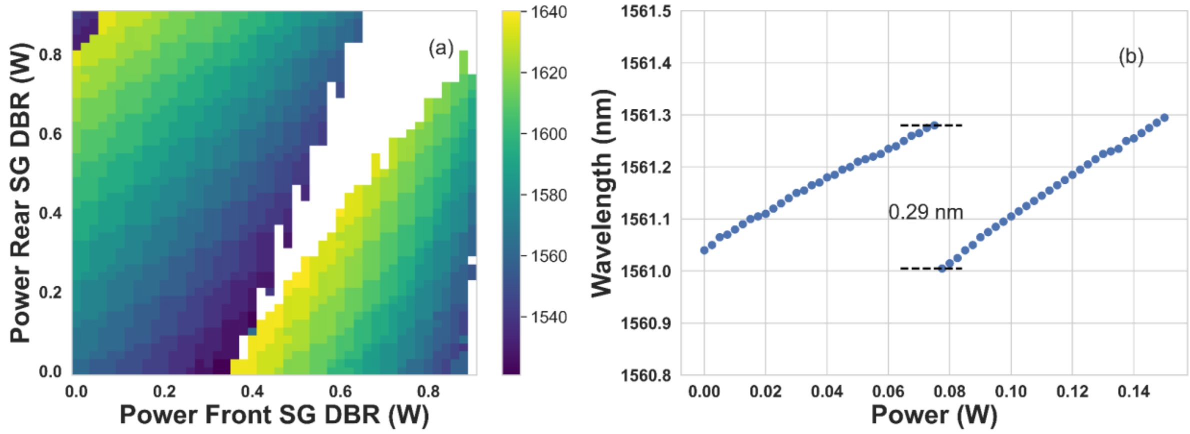

Figure 53 (a) Measured wavelength mapping at current of 150 mA on gain section.(b) Mode jump behavior with different power on the phase section.

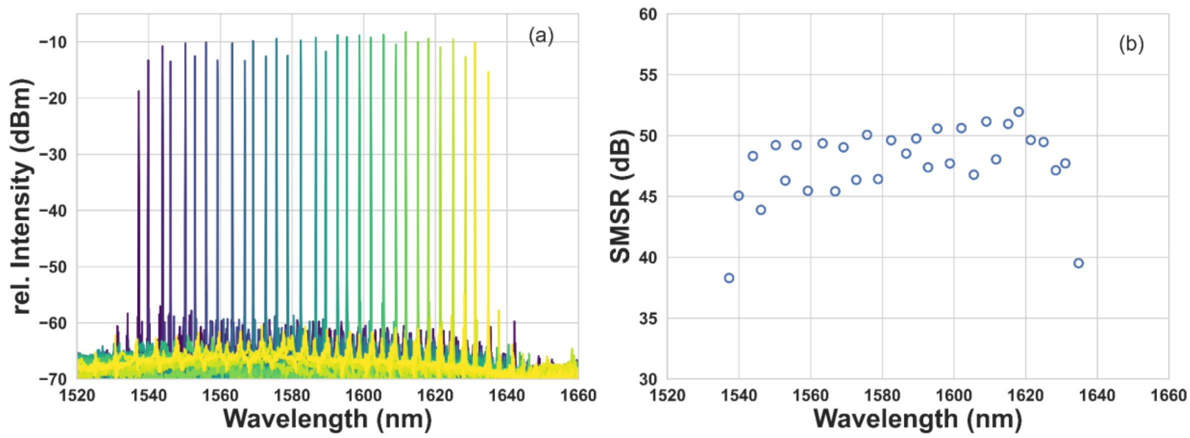

Figure 54 (a) Superposed optical spectra with 98 nm tuning range. (b) SMSRs over 38.3 dB.

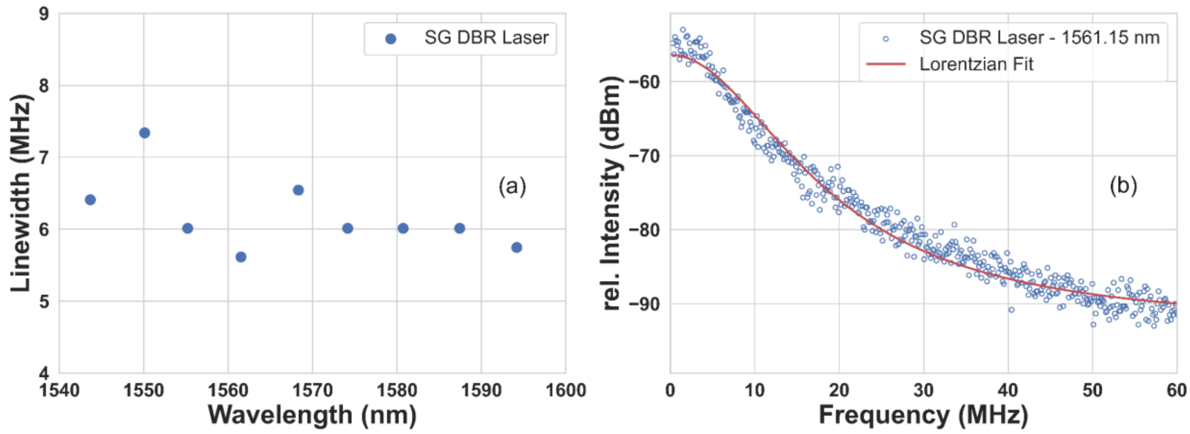

Figure 55 (a) Measured linewidth from Lorentzian fitting. (b) ESA spectrum with 1561.15 nm and corresponding Lorentzian fitting.

5. Tunable lasers for a THz PIC

This chapter introduces an application of the SG DBR laser, which is monolithically integrated PIC for THz spectroscopy with wide spectral bandwidth [99]. The PIC is based on the open-access generic foundry platforms [60], including two widely tunable sampled grating DBR (SG DBR) lasers, semiconductor optical amplifiers (SOAs), and passive components to combine signals. A state-of-the-art photodiode emitter is used to generate THz radiation. The measured THz power spectrum between 0.03 and 1 THz compares well with the spectrum generated with commercial tunable laser sources. This demonstrates the suitability of our PIC for future miniaturized CW THz systems. Partial results of this work have been published in [99], [100].

5.1. Fundamentals

THz technology is receiving much interest in a large variety of different fields [20], [101] like e.g. bio and medical applications [102], [103], spectroscopy [104], [105], and also for communications [106]. For these different applications, many approaches have been studied so far [107]. Two methods are widely investigated for a CW THz source based on photonics technology: a multi-wavelength source and optical heterodyning, respectively [106], [107]. Using a multi-wavelength source, represented, e.g., by a mode-locked laser with an external modulator or optical filter, a good spectral purity can be achieved, however, the THz bandwidth is limited. The optical heterodyning method using two different optical sources has the main advantage of a large THz bandwidth at the price of rather poor frequency stability [108]. Traditional approaches to realize THz sources use discrete optical components. Such an optical system comprising a bunch of different packaged components is large, and hence the system reliability is limited.

In contrast to the common THz system combining bulky modules, the PIC is a promising device for a THz system in order to significantly reduce cost and size, and to achieve high reliability. All required optical components such as laser sources, waveguides, couplers, splitters, modulators and amplifiers, can be integrated in such a PIC. The PIC size is in the range of several mm only, which is much smaller than a traditional system composed of different packed single elements. Moreover, PICs can be fabricated in large numbers such that scaling up for high volume and low costs is possible. Today, open-access generic foundry platforms [60], [61] offer all the required integrated components, i.e. building blocks (BBs), to fabricate the optical engine of a broadband CW THz system.

Hitherto, such PICs for THz applications have been realized with tunable distributed feedback (DFB) lasers and distributed Bragg reflector (DBR) lasers mostly, because of their technical maturity [108], [21], [109], [110], [22], [111], [112]. However, the narrow tuning range of DFB and DBR lasers limits the generated THz bandwidth. For example, usual DFB lasers provide a few nm tuning range only. DBR lasers with a separately tuned passive DBR section allow for larger tuning of about 15 nm [67]. PICs with two DFB lasers combined by a multimode interference (MMI) coupler [21] demonstrated a THz bandwidth of 1.25 THz by thermal tuning of the DFB lasers. References [108]–[110] have a similar design with [21] but include additional high-speed photodiodes (PD). Reference [22] coupled four DFB lasers in a PIC to cover a broad tuning range, providing 2.25 THz bandwidth in total. A DFB laser with an integrated tunable DBR was reported in [111] and enabled THz emission up to 1.5 THz. Using a hybrid integration approach based on a polymer PIC combined with InP chips [112], a THz bandwidth of 4.2 THz could be demonstrated. The good thermal properties of a polymer DBR allowed for lasers with a tuning range of 20 nm. However, the PIC requires additional hybrid integration of an InP based gain chip. Si-photonic PICs using ring lasers with 42 nm tunable laser have also been demonstrated [113], but also in this case the hybrid integration of an InP based gain chip is required.

5.2. Design and Simulation

Figure 56 shows a microscopic image of the realized PIC for a coherent THz spectrometer [114], [115], which requires two output ports with independent phase modulations for each wavelength. The PIC includes two SG DBR lasers with different tuning areas, namely laser 1 and laser 2, consisting of the front SG DBR, gain, phase, and rear SG DBR sections. The lengths of the sections are 500 µm, 400 µm, 120 µm, and 800 µm, respectively. The lasers are based on a ridge waveguide with a Fe-doped InP substrate. The gain section includes InGaAsP multi-quantum wells (MQWs) on top of a Q1.3-layer, and the other sections are designed by selectively etching the MQWs layers. Using direct-writing electron-beam lithography the SG DBR was patterned into the Q1.3 layer as chapter 3.3. The coupling coefficient was set to 120 cm^{-1}. Details of the layer information of these lasers are listed in reference [62]. SOAs have the same layer stack as the laser gain sections. The passive BBs, such as MMI couplers, TOPMs, and SSCs, are defined on an InGaAsP layer with a bandgap of 1060 nm. Butt-joint (BJ) sections connect the ridge waveguide from the lasers and SOAs to the deeply etched passive waveguides.

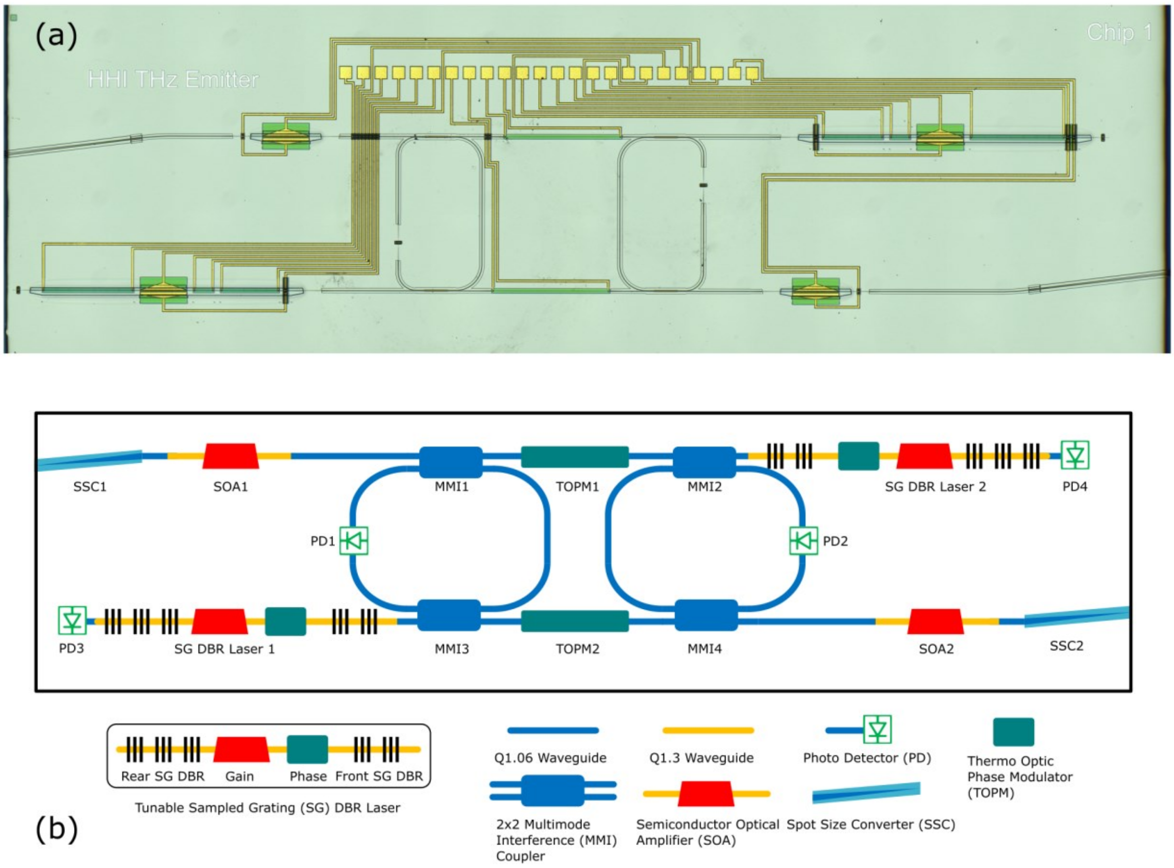

Figure 56 (a) Microscope image and (b) schematic image of the THz PIC. PDs are only absorbers to reduce back reflections and simplify output ports.

MMI2 and MMI3 divide the emitted light from laser 1 and 2, and MMI1 and MMI4 combine both wavelengths. Each port of MMI2 and MMI3 is connected to PD1 and PD2, respectively. The PDs absorb unwanted back reflections within the waveguide rings. To simplify the output, we connect one of the output ports from MMI1 and MMI4 to PD1 and PD2, respectively. The absorption of the PDs is sufficient to block any ring cavity effect. Output ports from MMI1 and MMI4 are coupled to SOAs. A SSC with an angle of 7° couples the amplified light into an optical fiber. An anti-reflection coating of the facet minimizes back reflection from the PIC to air interface. TOPMs control the phase of the light from laser 1 and laser 2. Predicted losses from the passive BBs are as follow: MMI: 3.5 dB, TOPM: 1 dB, SSC for fiber coupling: 3 dB and BJ: 2 dB.

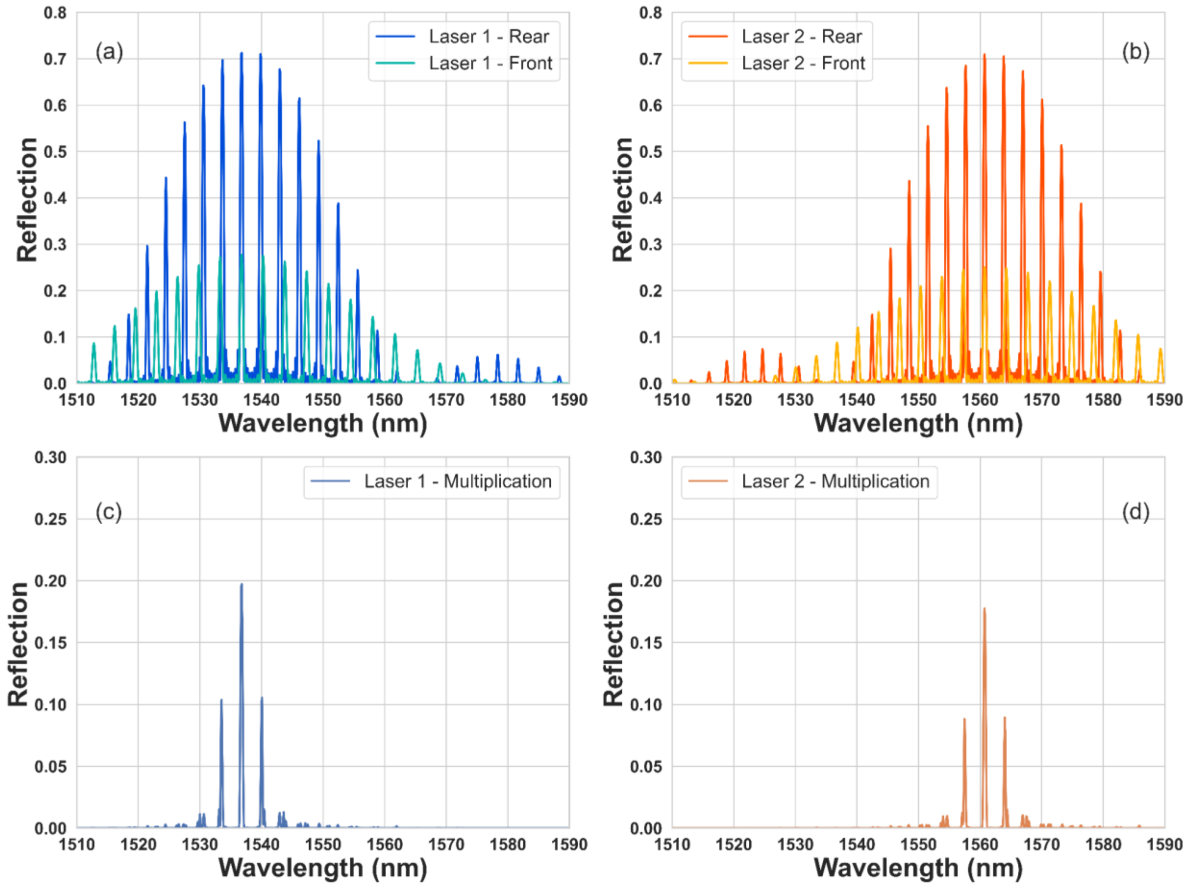

Figure 57 TMM simulation of laser 1 and 2. (a), (b) Reflection spectrum of front and rear SG DBRs. (c), (d) Multiplication of the reflections of the front and rear reflections in (a) and (b).

The SG DBR lasers are designed to cover different wavelength ranges with a small overlap. The design parameters of the SG DBRs are optimized based on the Vernier effect, which selects emission wavelengths from two slightly different comb-like reflections [13]. Both laser 1 and laser 2 have a target tuning range of 27 nm with a different center wavelength of 1538 nm and 1562 nm, respectively. Together, the two lasers cover 1524.5 nm - 1575.5 nm with an overlap of 3 nm. Corresponding $\Delta\lambda_f$ and $\Delta\lambda_r$ for the target tuning range are 3.5 nm and 3.1 nm, and the expected maximum reflections of the front and rear SG DBRs are 25% and 70%. Table 6 shows details of the design parameters. N_F and N_R denote the number of bursts in the front and rear SG DBRs. Figure 57 (a) and (b) show simulated reflection spectra of laser 1 and laser 2 calculated with the transfer matrix method (TMM), based on the design parameters in table 1. Fig. 2 (c) and (d) depict multiplications of the reflections in Figure 57 (a) and (b). Figure 57 (c) and (d) show the difference between the main and the side peaks around half. The experiment result of SMSRs is demonstrated over 37 dB, and it will be investigated in the next section.

The target tuning range of 27 nm is narrower than 53 nm in chapter 3.3, due to the low κ. The PIC is designed to follow the typical foundry process [60], which means that the κ is decided by the process value of $\kappa = 120$ cm^{-1}. Chapter 3.3 uses the technology based on the generic foundry platforms, but $\kappa = 300$ cm^{-1} to maximize the tuning range. The fabrication for chapter 3.3 is only focused on the tunable lasers, namely a dedicated wafer process.

Table 6 Detail parameters of the SG DBR lasers

	Laser 1	Laser 2
Center of wavelength (nm)	1538	1562
Z_{0_f} (μm)	93.9	97.5
Z_{1_f} (μm)	7.63	7.63
N_f	6	6
Z_{0_r} (μm)	106	110.1
Z_{1_r} (μm)	12.12	12.58
N_r	8	8

5.3. Experimental measurement

The realized PIC is mounted on an Au-coated heat sink and stabilized with a thermoelectric cooler (TEC) at 20°C to test the optical performance. Contact pads on the top of the PIC are connected to the control sections in the PIC by using the multi-needle probe to the pads for applying currents. Figure 58 (a) and (b) illustrate pulsed PI curves with an integrating sphere from SSC1. The current applied to SOA1 is 60 mA, and there is no applied current on the tuning sections. The PI curves show about 3 mW facet power at 100 mA gain current with 2.2 V. Threshold currents of the lasers are 41 mA and 43 mA for laser 1 and laser 2, respectively. The total power of two working lasers is expected the sum of each laser output. Furthermore, different SOA currents affects the optical output power, which is modeled and experimented as [116]. A 10 dB optical amplification is obtained by the 60 mA on the SOA. Laser 1 shows slightly lower power than laser 2 due to a curved waveguide with 200 μm-radius from MMI3 to MMI1, which has a larger loss for coupling to SSC1. In this case, the light from laser 2 passes through straight waveguides to SSC1, including lower loss than curved waveguide, therefore power of laser 2 is larger than laser 1. Moreover, laser 1 is closer to the SOA than laser 2 as in Fig. 1, such that the higher temperature of the SOA affects the thermal roll-off of laser 1.

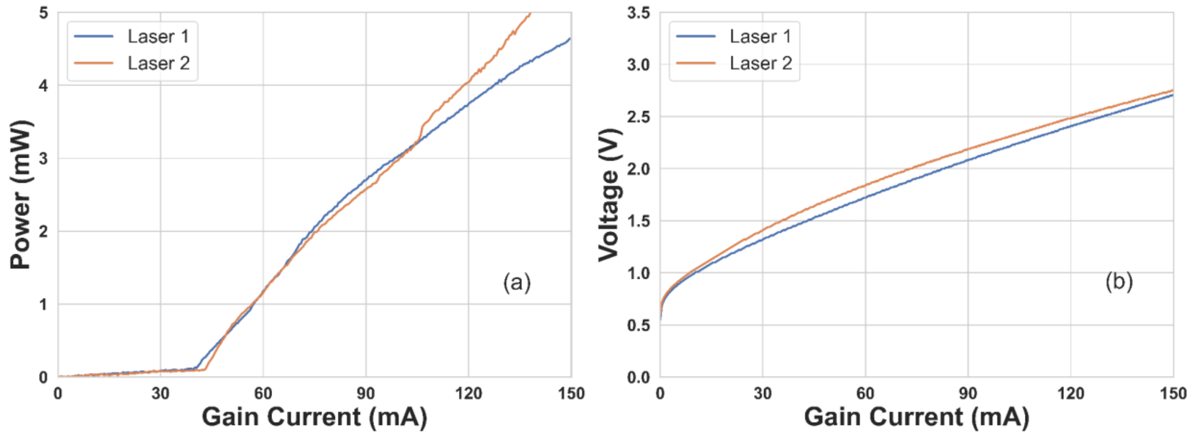

Figure 58 Pulsed PI measurement of laser 1 and 2 with 6 mA SOA current (a) PI curve. (b) Voltage measurement

Figure 59 (a) and (b) depict peak wavelengths of laser 1 and 2 with different tuning currents. The measurement setup is used as 3.3 and 4.4. The gain current of 100 mA is applied to the gain section, and 60 mA to SOA1. Front and rear currents were used between 0 and 45 mA and from 0 and 35 mA, respectively. Figure 60 (a) and (b) illustrate the selected optical spectra from Figure 59 (a) and (b) and the corresponding SMSRs. From Figure 59, one obtains, 24 nm tuning for laser 1 (1526 nm – 1550 nm), and 22 nm tuning for laser 2 (1547 nm - 1569 nm). Laser 2 has a smaller tuning range than laser 1 because of its lower gain at longer wavelengths. Note that the overlap between the two lasers is 4 nm. The SMSRs are depicted in Figure 60 (b). The lowest SMSR is 37 dB whereas the maximum amounts to 48 dB. Hence, the SMSR of this PIC is > 37 dB for all wavelength. Figure 59 and Figure 60 show that lasers can access any wavelength in the tuning range with the cavity mode. The laser power varies with wavelengths as shown in Figure 60 (a), but optimized currents on the gain section can improve the power distribution.

The tuning rage of this PIC, which amount to 43 nm, would allow for generating THz signals with a bandwidth of 5.36 THz. To the best of our knowledge this is a record value for monolithically integrated PICs.

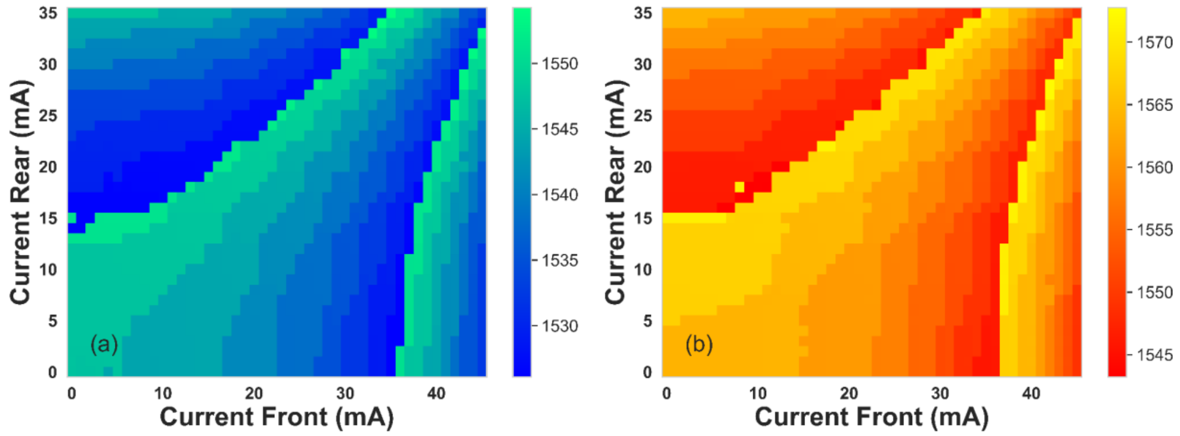

Figure 59 (a),(b) Peak wavelengths (nm) with different tuning currents of laser 1 and 2

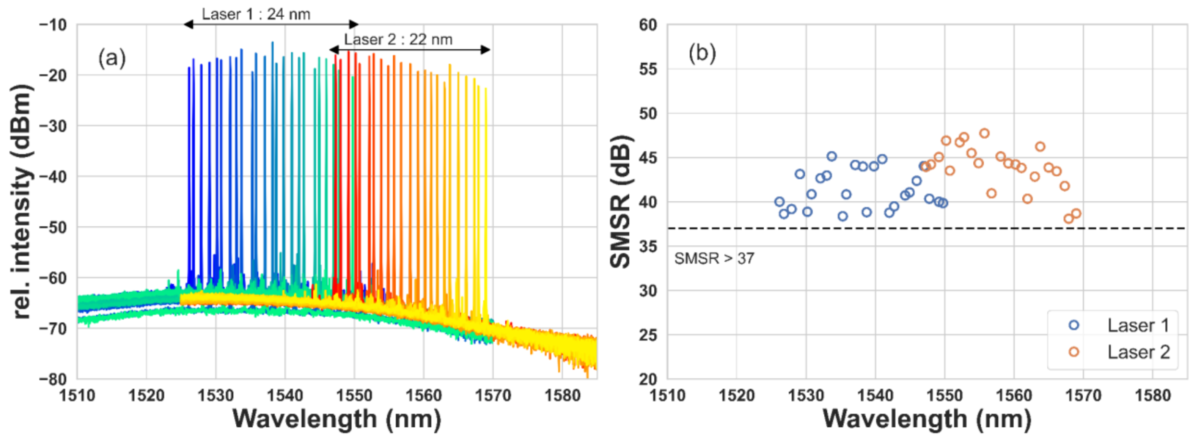

Figure 60 (a) Optical spectrum of laser 1 and laser 2 measured with an OSA. (b) SMSRs of laser 1 and laser 2.

In photonic CW THz systems the linewidth of the lasers determines the linewidth of the generated THz signal. In order to measure the optical linewidth of our laser PIC, a delayed self-homodyne method is used with the electrical spectrum analyzer (ESA) and the high-speed photodiode as aforementioned in 3.3.3. In Figure 61 (a) the linewidth of laser 1 (blue) and laser 2 (orange) are shown. The linewidth is determined as the FWHM of a Lorentzian fit to the measured data. This is exemplarily shown in Figure 61 (b) for 1530.8 nm (laser 1) and 1554.9 nm (laser 2). Note that the measured linewidth ranges from 2.69 MHz to 4.07 MHz for laser 1 and from 3.02 MHz to 4.26 MHz for laser 2. Laser 2 has slightly larger linewidth than laser 1 because of its lower gain in the longer wavelength range. Less gain leads to more spontaneous emission, i.e., larger threshold current, which means that the contribution of spontaneous emission to the phase noise is higher [72]. The linewidth value shows lower in the center of the tuning range, due to the reflection spectrum is maximum at the center region as shown in Figure 57.

The expected linewidth of the generated THz signal is still below 6 MHz ($\sqrt{2} \cdot 4.26$ MHz [117]), which provides high frequency resolution for a CW spectrometer [118]. Typically, ASE of the SOA degrades the optical linewidth. Such ASE increases the side lobes in the optical spectrum, of SG DBR laser, resulting in broaden linewidth. With an additional filter, e.g., MZI [30], it is expected that the linewidth can be improved.

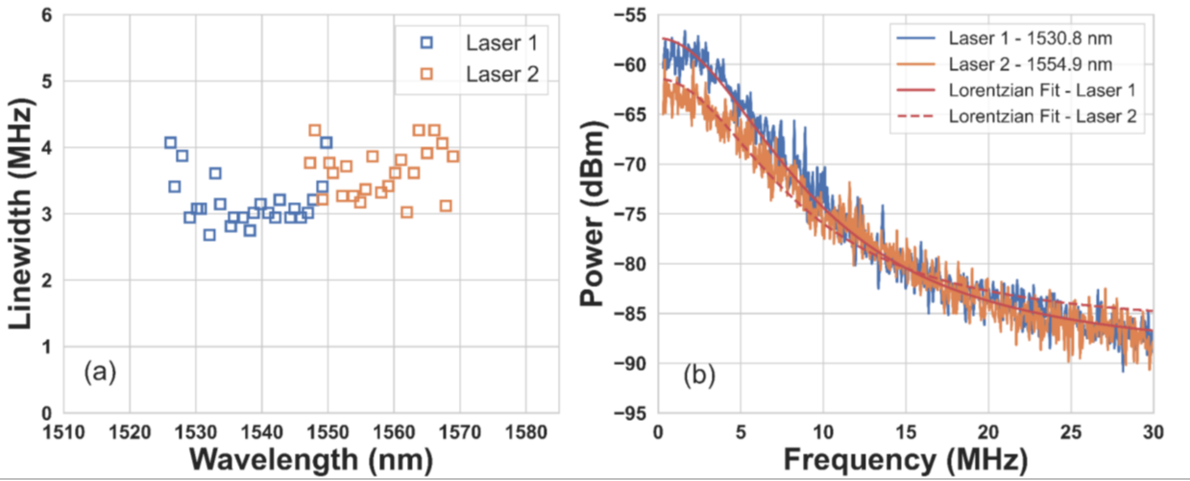

Figure 61 (a) Measured linewidth of laser 1 and laser 2 from Lorentzian fitting. (b) ESA spectrum of laser 1 and laser 2 with 1530.8 nm and 1554.9 nm, respectively. FWHMs of the Lorentzian fitting are 3.08 MHz and 3.17 MHz for laser 1 and laser 2.

In order to demonstrate THz generation with this PIC, spectral power measurement is performed with a THz photodiode (THz-PD, PCA-FD-1550-100-TX-3 from TOPTICA Photonics) similar to[119]. A schematic of our setup is shown in Figure 62. The optical beat signal of the PIC is connected to an isolator, preventing back-reflections from the measurement setup. An Erbium-doped fiber amplifier (EDFA) boosted the signal in order to drive the emitter with 8 mA photocurrent. The THz emitter is a state-of-the-art THz-PD with integrated broadband antenna, which is mounted on a silicon lens to radiate into free-space [120]. A 1% tap coupler allows to monitor the optical beat signal with an OSA. The THz-PD converts the optical beat signal to an electrical THz signal and radiated into ambient air. In order to measure the emitted terahertz signal with a pyroelectric power detector (THz20 from SLT), a waveform generator (model 3390 from Keithley) applies a square wave bias voltage between 0 V and -1.5 V with a frequency of 20 Hz to the THz-PD. A transimpedance amplifier (TIA), which is calibrated together with the power detector, boosts the detector current. A lock-in amplifier (LIA, model 7265 from Signal Recovery) synchronizes the detector signal with the bias of the emitter.

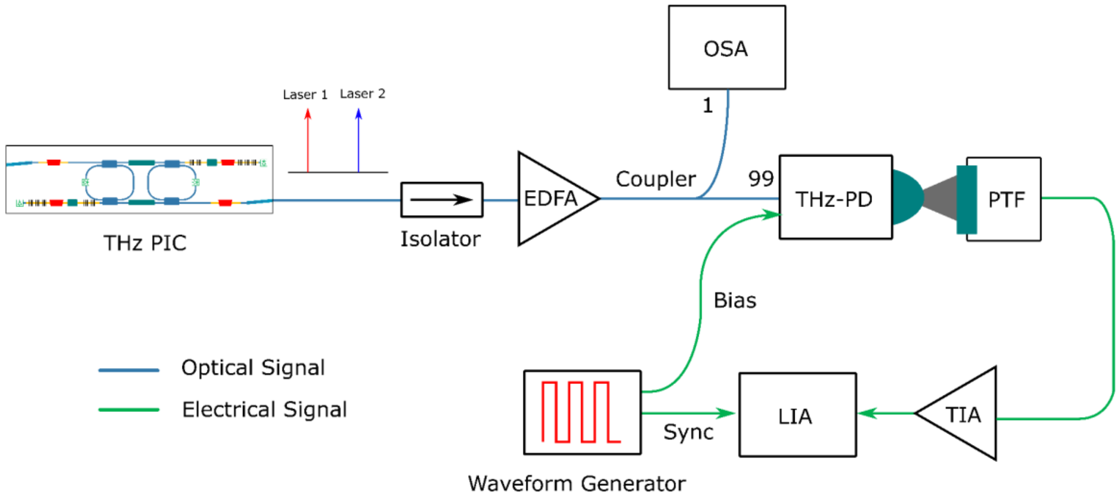

Figure 62 Schematic image of the THz measurement setup. Blue and green lines represent optical and electrical signals, respectively.

Two SG DBR lasers were controlled to generate THz signal. The wavelength tuning for both lasers was achieved by controlling the SG DBR sections in analogy to the previous measurements to generate THz signals. The 100 mA gain current is applied and adjusted it in the range ±10 mA in order to keep the peak power difference smaller than 3 dB. Furthermore, the applied current at SOA1 is 100 mA. Figure 63 (a) shows representative optical spectra with laser 1 and 2 operating simultaneously. The peak wavelengths are 1553.9 and 1555.5 nm for laser 1 and 2, respectively. The corresponding THz frequency is 199.6 GHz. Two commercially available tunable laser sources (TLS, i.e. AP3350A from APEX Technologies) are used instead of the PIC in the same measurement system to verify the PIC. Figure 63 (b) illustrates an optical spectrum of the TLS, with a difference frequency of 503.9 GHz (1552.9 and 1557 nm).

The experimental measurement of the THz power is shown in Figure 64. The THz power is measured from 0.03 to 1 THz with the maximum value of 320 μW at 0.1 THz, and 1.8 μW around 1 THz. Due to the sensitivity of the pyroelectric detector, the measurements are limited to 1 THz bandwidth. However, the THz power from the PIC matches the measurement with the TLSs, which verifies that the PIC can potentially replace the commercial laser sources. Since the PIC can generate optical beat signals higher than 5 THz, more broadband THz spectra is expected from operation in a coherent, i.e. more sensitive, measurement system [114], [115]. Since such systems requires complex and dynamic operation of The the PIC, the coherent THz system is still under investigation and will be presented elsewhere.

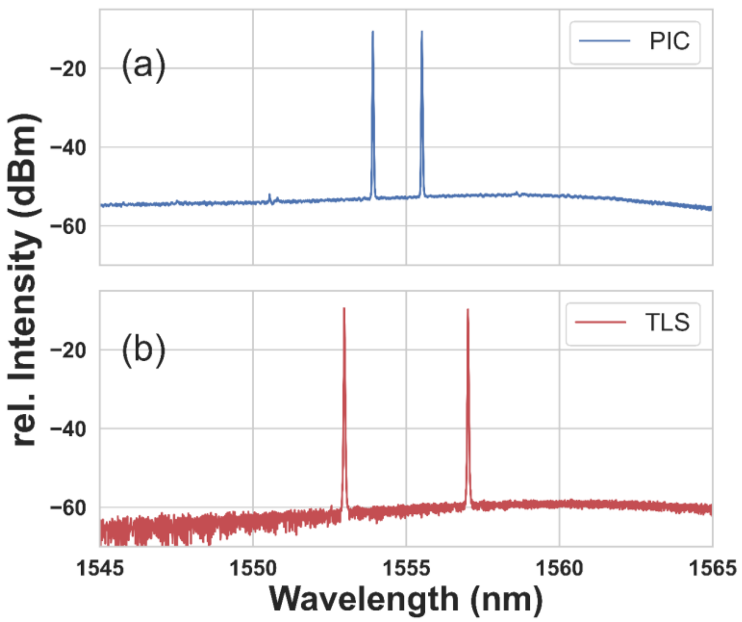

Figure 63 (a) Optical spectrum of the PIC while laser 1 and 2 are operated for 199.6 GHz simultaneously. (b) Optical spectrum of two discrete tunable laser sources (TLS) under the same conditions as in (a) for 503.9 GHz.

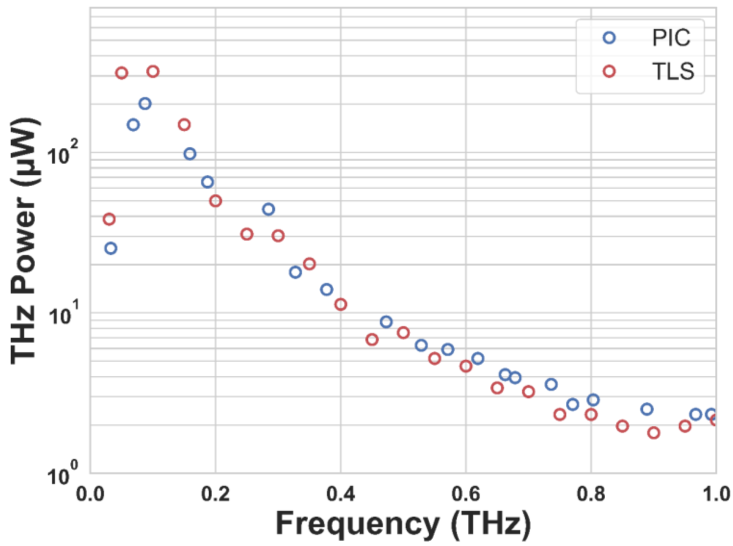

Figure 64 THz power from wavelength tuning of laser 1 and 2 generated by a PIN-PD emitter. The PIC (blue) and the TLS (red) are used as laser sources, respectively.

6. Conclusion and outlook

6.1. Conclusion

This thesis contributes three significant points to developing tunable lasers for a wide tuning range and narrow optical linewidth based on the InP platform used in optical communication and CW THz applications.

First, the SG DBR laser compatible with the open-access foundry platform is realized for the first time. The laser shows the 53 nm tuning range in the C band from 1533 to 1586 nm with over 42 dB SMSR. The Lorentzian optical linewidth amounts to 713 kHz, which is measured by the self-delayed homodyne method. The developed laser is the first SG DBR laser based on the foundry process with the minor modification for relatively deep etched gratings. From this work, the SG DBR is a part of PDK for customers. Table 7 summarizes key performances of tunable lasers based on the InP foundry platform and this work.

Second, the novel SG DBR RR laser is reported, which consists of the four section SG DBR laser and the additional RR. The RR aims to improve optical linewidth and provide predetermined wavelength channels. The laser is fabricated based on MQWs with different PLs to cover a wide tuning range. Passive components are optimized and realized, for example, low loss waveguides, MMI, and waveguide transitions. Moreover, the typical SG DBR laser is demonstrated with the equal layer stack and the wafer process of the proposed laser to verify the concept. It is investigated that wavelength channels of the 0.83 nm is demonstrated and the optical linewidth is improved by 48% compared with the typical SG DBR laser. Comparing the typical SG DBR laser with the tuning range of 56 nm, the SG DBR RR laser shows 28 nm because of the high loss of passive components.

Based on the same wafer, the widely tunable SG DBR laser is developed by optimizing the SG DBRs for covering the 98 nm tuning range. The measured SMSR is over 38.3 dB, and the Lorentzian optical linewidth is 7.34 MHz. Table 8 summarizes commercial tunable lasers based on the InP platform and this work.

The PIC for the CW THz application is demonstrated with the SG DBR lasers for the foundry platform. The PIC includes two SG DBR lasers offering 22 and 24 nm tuning ranges with 4 nm overlap. The combined tuning range of 43 nm corresponds to a bandwidth of 5.36 MHz, the highest bandwidth obtained with any integrated tunable laser source based on the InP platform. The SMSR is higher than 37 dB for the tuning range, and the measured optical linewidth is below 4.26 MHz, translating into a linewidth below 6 MHz of the corresponded THz signal. The THz power is measured between 0.03 to 1 THz. The THz performance is compared with commercial tunable sources. The PIC is fabricated by the InP foundry platform, has a small footprint, and is ready to be produced in volume at a low cost.

Table 7 Tunable lasers based on the InP foundry platform

Laser type	Tuning range	SMSR	Linewidth	Note	Reference
SG DBR laser*	53 nm	42 dB	713 kHz	First SG DBR laser for the foundry platform	[62] (2020)
Double RR laser	34 nm	50 dB	110 kHz		[17] (2020)
MZI laser	74 nm	43 dB	363 kHz	Large footprint	[54] (2015)
CCL	6.5 nm	40 dB	not released		[51] (2015)

*this work

Table 8 Commercial tunable lasers and the proposed SG DBR and SG DBR RR lasers

Laser type	Tuning range	SMSR	Linewidth	Note	Reference
SG DBR RR laser*	28 nm	39.7 dB	3.02 MHz	Wavelength channels of 0.83 nm Linewidth is improved by 48% compared to the SG DBR laser	[79] (2022)
SG DBR laser*	98 nm	38.3 dB	7.34 MHz		
SG DBR laser	55 nm	50.3 dB	100 kHz		[15] (2016)
Y Laser	35 nm	40 dB	not released		[47] (2004)
DS-DBR laser	40 nm	48 dB	200 kHz		[16] (2013)

*this work

Table 9 PICs for CW THz source

Laser type	Tuning range	SMSR	Linewidth	THz Signal	Reference
Two SG DBR lasers*	24 nm 22 nm	37 dB	4.07 MHz 4.26 MHz	1 THz (potential 5 THz)	[99] (2022)
Two DFB lasers	4 nm	45 dB	not released	570 GHz	[21] (2013)
Four DFB lasers	5 nm	50 dB	10 MHz	2.25 THz	[22] (2016)
DFB + DBR laser	15 nm	46 dB	5.6 MHz	1.5 THz	[111] (2012)

*this work

6.2. Outlook

For this work, the thermal tuning method is used to control the tuning of passive sections because it changes the moderate refractive index with low loss, compared with the current injection and QSE. The heat is generated by the Pt heater, which is deposited on the ridge waveguide. However, the required power for the wavelength tuning is relatively high, e.g., more than 1 W for two SG DBR (see Figure 46 (a) and (b)). Furthermore, the increased thermal power due to the low power efficiency generates the thermal crosstalk, as aforementioned in 4.4.2. To improve the thermal efficiency, reference [15] used the suspending waveguide, including the etched area surrounded the waveguide structure. Due to the thermal isolation by air, the thermal flow from the heater on the top is confined in the localized region, and hence it increases the temperature of the waveguide significantly. Even though this concept enhances the thermal efficiency, it requires a complex fabrication process to etch the area selectively. Moreover, the waveguide has to be hung suspended in the air, which is very fragile. For the issue, a patent [121] is published, which proposed a concept to etch the bottom of the wafer to block the thermal flow, directly dissipating to the heat sink. For the latter, the improved thermal tuning method will be demonstrated.

Whereas the proposed SG DBR RR laser shows prefixed wavelength channels and the improved optical linewidth, several further improvement can be investigated. The proposed laser uses the optimized waveguide with the n.i.d. InP layer for the low propagation loss. However, it is found that the loss is significant, resulting in the high threshold current and the limited tuning range due to the not enough height of the blocking layer. To solve this issue, the thicker blocking layer or a n-InP layer replacing the n.i.d. layer can be designed in the next generation. The thermal crosstalk from heaters on SG DBRs degrades the loss of MMIs and changes the channel spacing. As mentioned above, the improved thermal efficiency of heaters can solve the issue of the thermal crosstalk because the localized thermal heat will not influence other sections.

The SG DBR lasers in the PIC for the CW THz applications show the tuning range of 22 and 24 nm with 4 nm overlap, corresponding THz bandwidth of 5.36 THz. However, the measurement only investigates the THz signal up to 1 THz due to the limited performance of the THz-PD. With the coherent measurement setup [114], [115], the high bandwidth can be measured. Furthermore, the tuning range of SG DBR laser can be extended with the dedicated process, including deep etched gratings as 3.3.2.

7. Acknowledgments

I would like to thank my supervisor Prof. Dr. Martin Schell, for his valuable guidance and helpful discussion, which have enabled this thesis. This work is completed through collaboration with colleagues: Ariane Sigmund, Michael Theurer, Zander Marlene, Wolfgang Rehbein, and Martin Möhrle, who share knowledge and scientific experiences. The Ph.D. students in my group – Kanold Niklas, Gayatri Vasudevan Rajeswari, and Jan Gregor Gatzmann – inspire me to develop this project. Simon Nellen helps investigate THz part, and Francisco Soares and Moritz Baier contribute the part of foundry technology. I would like to acknowledge clean-room and back-end teams for their outstanding work. I am deeply indebted to Deutscher Akademischer Austauschdienst (DAAD), supporting financial funding for this work. Moreover, I would like to express my gratitude to my family, who believed in their son and brother. This work could not have been finished without the patience, support, and help of my beautiful wife Ilzoo. Finally, thank God for everything.

8. Published work

Publications related to this thesis

[1] M.-H. Lee, S. Nellen, F. Soares, M. Moehrle, W. Rehbein, M. Baier, B. Globisch, and M. Schell, “Photonic integrated circuit with sampled grating lasers fabricated on a generic foundry platform for broadband terahertz generation,” Opt. Express, vol. 30, no. 12, pp. 20149–20158, Jun. 2022, doi: 10.1364/OE.454296.

[2] M.-H. Lee, S. Nellen, F. Soares, M. Moehrle, W. Rehbein, M. Baier, and M. Schell, “InP integrated photonic circuit for terahertz spectroscopy up to 4.1 THz bandwidth based on sampled grating lasers,” in Conference on Lasers and Electro-Optics (2021), paper ATu2T.6, May 2021, p. ATu2T.6. doi: 10.1364/CLEO_AT.2021.ATu2T.6.

[3] M.-H. Lee, F. Soares, M. Baier, M. Moehrle, W. Rehbein, and M. Schell, “53 nm sampled grating tunable lasers from an InP generic foundry platform,” in Semiconductor Lasers and Laser Dynamics IX, Apr. 2020, vol. 11356, p. 1135605. doi: 10.1117/12.2554541.

[4] M. Moehrle and M.-H. Lee, “Dwdm intra-cavity laser device,” EP3840138A1, Jun. 23, 2021 Accessed: Apr. 29, 2022. [Online]. Available: https://patents.google.com/patent/EP3840138A1/de?inventor=moon-hyeok+lee&oq=moon-hyeok+lee

[5] M. Moehrle and M.-H. Lee, “Thermally tunable laser and method for fabricating such laser,” EP3565068A1, Nov. 06, 2019 Accessed: Apr. 29, 2022. [Online]. Available: https://patents.google.com/patent/EP3565068A1/en?inventor=moon-hyeok+lee&oq=moon-hyeok+lee

9. Reference

[1] “International Telecommunication Union (ITU) statistics,” *ITU*. https://www.itu.int:443/en/ITU-D/Statistics/Pages/stat/default.aspx (accessed Dec. 28, 2021).

[2] K. George, “IEA (2021), Data Centres and Data Transmission Networks,” *IEA*. https://www.iea.org/reports/data-centres-and-data-transmission-networks (accessed Dec. 28, 2021).

[3] M. Dayarathna, Y. Wen, and R. Fan, “Data Center Energy Consumption Modeling: A Survey,” *IEEE Commun. Surv. Tutor.*, vol. 18, no. 1, pp. 732–794, 2016, doi: 10.1109/COMST.2015.2481183.

[4] H. Ishio, J. Minowa, and K. Nosu, “Review and status of wavelength-division-multiplexing technology and its application,” *J. Light. Technol.*, vol. 2, no. 4, pp. 448–463, 1984, doi: 10.1109/JLT.1984.1073653.

[5] J. C. Palais, *Fiber Optic Communications*, 5th edition. Upper Saddle River, N.J: Pearson, 2004.

[6] J. M. H. Elmirghani and H. T. Mouftah, “All-optical wavelength conversion: technologies and applications in DWDM networks,” *IEEE Commun. Mag.*, vol. 38, no. 3, pp. 86–92, Mar. 2000, doi: 10.1109/35.825645.

[7] G. Jay, “Infinera, Future-proofing Your Network with Infinera C+L,” *www.infinera.com*, Jul. 08, 2019. https://www.infinera.com/blog/future-proofing-your-network-with-infinera-c-l/tag/innovation/ (accessed Dec. 31, 2021).

[8] S. Varma and M. L. Rampal, “Coherent communication system,” in *Proc. SPIE 1622, Emerging Optoelectronic Technologies*, Dec. 1992, vol. 1622, pp. 390–393. doi: 10.1117/12.637020.

[9] Infinera, “Coherent WDM technologies,” White Paper, 2016. [Online]. Available: https://www.infinera.com/wp-content/uploads/Infinera_Coherent_Tech.pdf

[10] M. Seimetz, “Laser Linewidth Limitations for Optical Systems with High-Order Modulation Employing Feed Forward Digital Carrier Phase Estimation,” in *OFC/NFOEC 2008 - 2008 Conference on Optical Fiber Communication/National Fiber Optic Engineers Conference*, Feb. 2008, pp. 1–3. doi: 10.1109/OFC.2008.4528637.

[11] V. Lal *et al.*, “Extended C-Band Tunable Multi-Channel InP-Based Coherent Transmitter PICs,” *J. Light. Technol.*, vol. 35, no. 7, pp. 1320–1327, Apr. 2017.

[12] J. J. Coleman, “The development of the semiconductor laser diode after the first demonstration in 1962,” *Semicond. Sci. Technol.*, vol. 27, no. 9, p. 090207, Aug. 2012, doi: 10.1088/0268-1242/27/9/090207.

[13] H. Debrégeas, “Widely Tunable Laser Diodes,” in *Fibre Optic Communication: Key Devices*, H. Venghaus and N. Grote, Eds. Cham: Springer International Publishing, 2017, pp. 209–248. doi: 10.1007/978-3-319-42367-8_5.

[14] P. Abolghasem *et al.*, “Monolithically integrated L-band PICs and transceiver modules with 6λ x 200 Gbps (1.2 Tbps) for C + L band communication systems,” *Opt. Express*, vol. 27, no. 12, pp. 16483–16492, Jun. 2019, doi: 10.1364/OE.27.016483.

[15] M. C. Larson, “Narrow linewidth tunable DBR lasers,” in *2016 International Semiconductor Laser Conference (ISLC)*, Sep. 2016, pp. 1–2.

[16] S. C. Davies *et al.*, “Narrow linewidth, high power, high operating temperature digital supermode distributed Bragg reflector laser,” in *39th European Conference and Exhibition on Optical Communication (ECOC 2013)*, Sep. 2013, pp. 1–3. doi: 10.1049/cp.2013.1503.

[17] S. Andreou, K. A. Williams, and E. A. J. M. Bente, “Electro-Optic Tuning of a Monolithically Integrated Widely Tuneable InP Laser With Free-Running and Stabilized Operation,” *J. Light. Technol.*, vol. 38, no. 7, pp. 1887–1894, Apr. 2020, doi: 10.1109/JLT.2019.2952466.
[18] T. Komljenovic *et al.*, “Widely-Tunable Ring-Resonator Semiconductor Lasers,” *Appl. Sci.*, vol. 7, no. 7, Art. no. 7, Jul. 2017, doi: 10.3390/app7070732.
[19] K.-J. Boller *et al.*, “Hybrid Integrated Semiconductor Lasers with Silicon Nitride Feedback Circuits,” *Photonics*, vol. 7, no. 1, Art. no. 1, Mar. 2020, doi: 10.3390/photonics7010004.
[20] M. Tonouchi, “Cutting-edge terahertz technology,” *Nat. Photonics*, vol. 1, no. 2, pp. 97–105, Feb. 2007, doi: 10.1038/nphoton.2007.3.
[21] M. Theurer *et al.*, “Photonic-integrated circuit for continuous-wave THz generation,” *Opt. Lett.*, vol. 38, no. 19, pp. 3724–3726, Oct. 2013, doi: 10.1364/OL.38.003724.
[22] M. Sun *et al.*, “Integrated Four-Wavelength DFB Diode Laser Array for Continuous-Wave THz Generation,” *IEEE Photonics J.*, vol. 8, no. 4, pp. 1–8, Aug. 2016, doi: 10.1109/JPHOT.2016.2580940.
[23] J. Buus, M.-C. Amann, and D. J. Blumenthal, “Fundamental Laser Diode Characteristics,” in *Tunable Laser Diodes and Related Optical Sources*, 2nd edition., Hoboken, N.J: Wiley-IEEE Press, 2005.
[24] P. J. A. Thijs, L. F. Tiemeijer, P. I. Kuindersma, J. J. M. Binsma, and T. Van Dongen, “High-performance 1.5 mu m wavelength InGaAs-InGaAsP strained quantum well lasers and amplifiers,” *IEEE J. Quantum Electron.*, vol. 27, no. 6, pp. 1426–1439, Jun. 1991, doi: 10.1109/3.89960.
[25] T. J. Reid, C. A. Park, P. J. Williams, A. K. Wood, and J. Buus, “3.8nm continuous tuning range of a low threshold distributed bragg reflector laser,” presented at the 12th IEEE International Conference on Semiconductor Laser, Sep. 1990. doi: 10.1109/ISLC.1990.764510.
[26] J. Buus, M.-C. Amann, and D. J. Blumenthal, “Basic Concepts of Tunable Laser Diodes,” in *Tunable Laser Diodes and Related Optical Sources*, 2nd edition., Hoboken, N.J: Wiley-IEEE Press, 2005.
[27] E. Goebel, G. Luz, and E. Schlosser, “Optical gain spectra of InGaAsP/InP double heterostructures,” *IEEE J. Quantum Electron.*, vol. 15, no. 8, pp. 697–700, Aug. 1979, doi: 10.1109/JQE.1979.1070095.
[28] B. I. Miller, J. H. McFee, R. J. Martin, and P. K. Tien, “Room-temperature operation of lattice-matched InP/Ga0.47In0.53As/InP double-heterostructure lasers grown by MBE,” *Appl. Phys. Lett.*, vol. 33, no. 1, pp. 44–47, Jul. 1978, doi: 10.1063/1.90186.
[29] B. R. Bennett, R. A. Soref, and J. A. Del Alamo, “Carrier-induced change in refractive index of InP, GaAs and InGaAsP,” *IEEE J. Quantum Electron.*, vol. 26, no. 1, pp. 113–122, Jan. 1990, doi: 10.1109/3.44924.
[30] J.-P. Weber, “Optimization of the carrier-induced effective index change in InGaAsP waveguides-application to tunable Bragg filters,” *IEEE J. Quantum Electron.*, vol. 30, no. 8, pp. 1801–1816, Aug. 1994, doi: 10.1109/3.301645.
[31] T. H. Wood, C. A. Burrus, and D. A. B. Miller, “High-speed optical modulation with GaAs/GaAlAs quantum wells in a p-i-n diode structure,” *Appl Phys Lett*, vol. 44, p. 4, 1984.
[32] D. A. B. Miller *et al.*, “Band-Edge Electroabsorption in Quantum Well Structures: The Quantum-Confined Stark Effect,” *Phys. Rev. Lett.*, vol. 53, no. 22, pp. 2173–2176, Nov. 1984, doi: 10.1103/PhysRevLett.53.2173.

[33] P. Geng *et al.*, “Effects of temperature and redshift on the refractive index of semiconductors,” *J. Appl. Phys.*, vol. 124, no. 3, p. 035703, Jul. 2018, doi: 10.1063/1.5027771.

[34] S. Adachi, “Refractive indices of III–V compounds: Key properties of InGaAsP relevant to device design,” *J. Appl. Phys.*, vol. 53, no. 8, pp. 5863–5869, Aug. 1982, doi: 10.1063/1.331425.

[35] D. Melati, A. Waqas, A. Alippi, and A. Melloni, “Wavelength and composition dependence of the thermo-optic coefficient for InGaAsP-based integrated waveguides,” *J. Appl. Phys.*, vol. 120, no. 21, p. 213102, Dec. 2016, doi: 10.1063/1.4970937.

[36] M. A. Afromowitz, “Refractive index of Ga1−xAlxAs,” *Solid State Commun.*, vol. 15, no. 1, pp. 59–63, Jul. 1974, doi: 10.1016/0038-1098(74)90014-3.

[37] K. Utaka, K. Kobayashi, and Y. Suematsu, “Lasing characteristics of 1.5 - 1.6 μm GaInAsP/InP integrated twin-guide lasers with first-order distributed Bragg reflectors,” *IEEE J. Quantum Electron.*, vol. 17, no. 5, pp. 651–658, May 1981, doi: 10.1109/JQE.1981.1071156.

[38] S. H. Wemple and M. DiDomenico, “Behavior of the Electronic Dielectric Constant in Covalent and Ionic Materials,” *Phys. Rev. B*, vol. 3, no. 4, pp. 1338–1351, Feb. 1971, doi: 10.1103/PhysRevB.3.1338.

[39] K. Chinen *et al.*, “Low-threshold 1.55-μm InGaAsP/InP buried heterostructure distributed feedback lasers,” *Appl. Phys. Lett.*, vol. 51, no. 4, pp. 273–275, Jul. 1987, doi: 10.1063/1.98471.

[40] L. A. Coldren, “Monolithic tunable diode lasers,” *IEEE J. Sel. Top. Quantum Electron.*, vol. 6, no. 6, pp. 988–999, Nov. 2000, doi: 10.1109/2944.902147.

[41] F. Delorme, G. Terol, H. de Bailliencourt, S. Grosmaire, and P. Devoldere, “Long-term wavelength stability of 1.55-/spl mu/m tunable distributed Bragg reflector lasers,” *IEEE J. Sel. Top. Quantum Electron.*, vol. 5, no. 3, pp. 480–486, May 1999, doi: 10.1109/2944.788409.

[42] S. L. Woodward, U. Koren, B. I. Miller, M. G. Young, M. A. Newkirk, and C. A. Burrus, “A DBR laser tunable by resistive heating,” *IEEE Photonics Technol. Lett.*, vol. 4, no. 12, pp. 1330–1332, Dec. 1992, doi: 10.1109/68.180566.

[43] L. Yu *et al.*, “A Widely Tunable Directly Modulated DBR Laser With High Linearity,” *IEEE Photonics J.*, vol. 6, no. 4, pp. 1–8, Aug. 2014, doi: 10.1109/JPHOT.2014.2331247.

[44] V. Jayaraman, A. Mathur, L. A. Coldren, and P. D. Dapkus, “Extended tuning range in sampled grating DBR lasers,” *IEEE Photonics Technol. Lett.*, vol. 5, no. 5, pp. 489–491, May 1993, doi: 10.1109/68.215257.

[45] H. Ishii, Y. Tohmori, Y. Yoshikuni, T. Tamamura, and Y. Kondo, “Multiple-phase shift super structure grating DBR lasers for broad wavelength tuning,” *IEEE Photonics Technol. Lett.*, vol. 5, no. 6, pp. 613–615, Jun. 1993, doi: 10.1109/68.219686.

[46] H. Ishii, F. Kano, Y. Tohmori, Y. Kondo, T. Tamamura, and Y. Yoshikuni, “Narrow spectral linewidth under wavelength tuning in thermally tunable super-structure-grating (SSG) DBR lasers,” *IEEE J. Sel. Top. Quantum Electron.*, vol. 1, no. 2, pp. 401–407, Jun. 1995, doi: 10.1109/2944.401222.

[47] J.-O. Wesström, G. Sarlet, S. Hammerfeldt, L. Lundqvist, P. Szabo, and P.-J. Rigole, “State-of-the-art performance of widely tunable modulated grating Y-branch lasers,” in *Optical Fiber Communication Conference (2004), paper TuE2*, Feb. 2004, p. TuE2. Accessed: Jan. 12, 2022. [Online]. Available: https://www.osapublishing.org/abstract.cfm?uri=OFC-2004-TuE2

[48] J.-O. Wesstrom, S. Hammerfeldt, J. Buus, R. Siljan, R. Laroy, and H. de Vries, “Design of a widely tunable modulated grating Y-branch laser using the additive Vernier effect

for improved super-mode selection," in *IEEE 18th International Semiconductor Laser Conference*, Sep. 2002, pp. 99–100. doi: 10.1109/ISLC.2002.1041137.
[49] M. Oberg, S. Nilsson, K. Streubel, J. Wallin, L. Backbom, and T. Klinga, "74 nm wavelength tuning range of an InGaAsP/InP vertical grating assisted codirectional coupler laser with rear sampled grating reflector," *IEEE Photonics Technol. Lett.*, vol. 5, no. 7, pp. 735–737, Jul. 1993, doi: 10.1109/68.229789.
[50] R. Todt *et al.*, "Sampled grating tunable twin-guide laser diodes with over 40-nm electronic tuning range," *IEEE Photonics Technol. Lett.*, vol. 17, no. 12, pp. 2514–2516, Dec. 2005, doi: 10.1109/LPT.2005.859155.
[51] D. D'Agostino, D. Lenstra, H. P. M. M. Ambrosius, and M. K. Smit, "Coupled cavity laser based on anti-resonant imaging via multimode interference," *Opt. Lett.*, vol. 40, no. 4, pp. 653–656, Feb. 2015, doi: 10.1364/OL.40.000653.
[52] X. Xiong, Z. Hu, S. Zhang, X. Liao, and J. He, "Narrow linewidth tunable V-cavity laser using self-injection method," *Opt. Express*, vol. 25, no. 26, pp. 32957–32963, Dec. 2017, doi: 10.1364/OE.25.032957.
[53] S. Cheung, "High-Speed, Directly-Modulated Widely Tunable 1310 nm Coupled Cavity Laser Via Multimode Interference," *J. Light. Technol.*, vol. 37, no. 9, pp. 2133–2139, May 2019, doi: 10.1109/JLT.2019.2898832.
[54] S. Latkowski *et al.*, "Novel Widely Tunable Monolithically Integrated Laser Source," *IEEE Photonics J.*, vol. 7, no. 6, pp. 1–9, Dec. 2015, doi: 10.1109/JPHOT.2015.2493722.
[55] W. Bogaerts *et al.*, "Silicon microring resonators," *Laser Photonics Rev.*, vol. 6, no. 1, pp. 47–73, 2012, doi: 10.1002/lpor.201100017.
[56] M. A. Tran, D. Huang, and J. E. Bowers, "Tutorial on narrow linewidth tunable semiconductor lasers using Si/III-V heterogeneous integration," *APL Photonics*, vol. 4, no. 11, p. 111101, Nov. 2019, doi: 10.1063/1.5124254.
[57] M. A. Tran, D. Huang, T. Komljenovic, J. Peters, A. Malik, and J. E. Bowers, "Ultra-Low-Loss Silicon Waveguides for Heterogeneously Integrated Silicon/III-V Photonics," *Appl. Sci.*, vol. 8, no. 7, Art. no. 7, Jul. 2018, doi: 10.3390/app8071139.
[58] T. Segawa, T. Sato, R. Iga, S. Matsuo, and R. Takahashi, "A novel tunable laser with flat-output wideband tuning based on parallel ring resonators," in *2012 International Conference on Photonics in Switching (PS)*, Sep. 2012, pp. 1–3.
[59] M. A. Tran, D. Huang, J. Guo, T. Komljenovic, P. A. Morton, and J. E. Bowers, "Ring-Resonator Based Widely-Tunable Narrow-Linewidth Si/InP Integrated Lasers," *IEEE J. Sel. Top. Quantum Electron.*, vol. 26, no. 2, pp. 1–14, Mar. 2020, doi: 10.1109/JSTQE.2019.2935274.
[60] N. Grote, M. Baier, and F. Soares, "Photonic Integrated Circuits on InP," in *Fibre Optic Communication: Key Devices*, H. Venghaus and N. Grote, Eds. Cham: Springer International Publishing, 2017, pp. 799–840. doi: 10.1007/978-3-319-42367-8_16.
[61] M. Smit *et al.*, "An introduction to InP-based generic integration technology," *Semicond. Sci. Technol.*, vol. 29, no. 8, p. 083001, Jun. 2014, doi: 10.1088/0268-1242/29/8/083001.
[62] M.-H. Lee, F. Soares, M. Baier, M. Möhrle, W. Rehbein, and M. Schell, "53 nm sampled grating tunable lasers from an InP generic foundry platform," in *Semiconductor Lasers and Laser Dynamics IX*, Apr. 2020, vol. 11356, p. 1135605. doi: 10.1117/12.2554541.
[63] "Optical Waveguide Design Software - Lumerical MODE," *Lumerical*. https://www.lumerical.com/products/mode/ (accessed Jan. 19, 2022).
[64] R. J. Deri and E. Kapon, "Low-loss III-V semiconductor optical waveguides," *IEEE J. Quantum Electron.*, vol. 27, no. 3, pp. 626–640, Mar. 1991, doi: 10.1109/3.81372.

[65] V. Jayaraman, Z.-M. Chuang, and L. A. Coldren, “Theory, design, and performance of extended tuning range semiconductor lasers with sampled gratings,” *IEEE J. Quantum Electron.*, vol. 29, no. 6, pp. 1824–1834, Jun. 1993, doi: 10.1109/3.234440.
[66] L. A. Coldren, S. W. Corzine, and M. L. Mašanović, “Photonic Integrated Circuits,” in *Diode Lasers and Photonic Integrated Circuits*, John Wiley & Sons, Ltd, 2012, pp. 451–507. doi: 10.1002/9781118148167.ch8.
[67] J. Buus, M.-C. Amann, and D. J. Blumenthal, “Wavelength-Tunable Single-Mode Laser Diodes,” in *Tunable Laser Diodes and Related Optical Sources*, 2nd edition., Hoboken, N.J: Wiley-IEEE Press, 2005.
[68] J. Buus, M.-C. Amann, and D. J. Blumenthal, “Widely Tunable Monolithic Laser Diodes,” in *Tunable Laser Diodes and Related Optical Sources*, 2nd edition., Hoboken, N.J: Wiley-IEEE Press, 2005.
[69] Y. A. Akulova *et al.*, “Widely tunable electroabsorption-modulated sampled-grating DBR laser transmitter,” *IEEE J. Sel. Top. Quantum Electron.*, vol. 8, no. 6, pp. 1349–1357, Nov. 2002, doi: 10.1109/JSTQE.2002.806677.
[70] J. Buus, M.-C. Amann, and D. J. Blumenthal, “Single-Mode Laser Diodes,” in *Tunable Laser Diodes and Related Optical Sources*, 2nd edition., Hoboken, N.J: Wiley-IEEE Press, 2005.
[71] A. L. Schawlow and C. H. Townes, “Infrared and Optical Masers,” *Phys. Rev.*, vol. 112, no. 6, pp. 1940–1949, Dec. 1958, doi: 10.1103/PhysRev.112.1940.
[72] C. Henry, “Theory of the linewidth of semiconductor lasers,” *IEEE J. Quantum Electron.*, vol. 18, no. 2, pp. 259–264, Feb. 1982, doi: 10.1109/JQE.1982.1071522.
[73] J. Buus, M.-C. Amann, and D. J. Blumenthal, “Linewidth Broadening,” in *Tunable Laser Diodes and Related Optical Sources*, 2nd edition., Hoboken, N.J: Wiley-IEEE Press, 2005.
[74] M. Fukuda, T. Hirono, T. Kurosaki, and F. Kano, “1/f noise behavior in semiconductor laser degradation,” *IEEE Photonics Technol. Lett.*, vol. 5, no. 10, pp. 1165–1167, Oct. 1993, doi: 10.1109/68.248415.
[75] M. J. O’Mahony and I. D. Henning, “Semiconductor laser linewidth broadening due to 1/f carrier noise,” *Electron. Lett.*, vol. 19, no. 23, pp. 1000–1001, Nov. 1983, doi: 10.1049/el:19830679.
[76] G. M. Stéphan, T. T. Tam, S. Blin, P. Besnard, and M. Têtu, “Laser line shape and spectral density of frequency noise,” *Phys. Rev. A*, vol. 71, no. 4, p. 043809, Apr. 2005, doi: 10.1103/PhysRevA.71.043809.
[77] T. Okoshi, K. Kikuchi, and A. Nakayama, “Novel method for high resolution measurement of laser output spectrum,” *Electron. Lett.*, vol. 16, no. 16, pp. 630–631, Jul. 1980, doi: 10.1049/el:19800437.
[78] P. Horak and W. H. Loh, “On the delayed self-heterodyne interferometric technique for determining the linewidth of fiber lasers,” *Opt. Express*, vol. 14, no. 9, pp. 3923–3928, May 2006, doi: 10.1364/OE.14.003923.
[79] M. MÖHRLE and M.-H. Lee, “Dwdm intra-cavity laser device,” EP3840138A1, Jun. 23, 2021 Accessed: Apr. 29, 2022. [Online]. Available: https://patents.google.com/patent/EP3840138A1/de?inventor=moon-hyeok+lee&oq=moon-hyeok+lee
[80] “G.694.1 : Spectral grids for WDM applications: DWDM frequency grid.” https://www.itu.int/rec/T-REC-G.694.1 (accessed Mar. 09, 2022).
[81] T. Haber, K. Hsu, C. Miller, and Y. Bao, “Tunable erbium-doped fiber ring laser precisely locked to the 50-GHz ITU frequency grid,” *IEEE Photonics Technol. Lett.*, vol. 12, no. 11, pp. 1456–1458, Nov. 2000, doi: 10.1109/68.887659.

[82] B. Hammond, B. Su, J. Mathews, E. Chen, and E. Schwartz, "Integrated wavelength locker for tunable laser applications," in *The 15th Annual Meeting of the IEEE Lasers and Electro-Optics Society*, Nov. 2002, vol. 2, pp. 479–480 vol.2. doi: 10.1109/LEOS.2002.1159389.
[83] G. Sarlet, G. Morthier, and R. Baets, "Control of widely tunable SSG-DBR lasers for dense wavelength division multiplexing," *J. Light. Technol.*, 2000, doi: 10.1109/50.857759.
[84] S. Andreou, K. A. Williams, and E. A. J. M. Bente, "Radio-Frequency Signal Generation Using Actively Frequency Stabilised Monolithically Integrated InP-Based Lasers," in *2019 21st International Conference on Transparent Optical Networks (ICTON)*, Jul. 2019, pp. 1–4. doi: 10.1109/ICTON.2019.8840572.
[85] S. Andreou, K. A. Williams, and E. A. J. M. Bente, "Monolithically integrated InP-based DBR lasers with an intra-cavity ring resonator," *Opt. Express*, vol. 27, no. 19, pp. 26281–26294, Sep. 2019, doi: 10.1364/OE.27.026281.
[86] D. D'Agostino *et al.*, "Low-loss passive waveguides in a generic InP foundry process via local diffusion of zinc," *Opt. Express*, vol. 23, no. 19, pp. 25143–25157, Sep. 2015, doi: 10.1364/OE.23.025143.
[87] L. H. Spiekman, Y. S. Oei, E. G. Metaal, F. H. Green, I. Moerman, and M. K. Smit, "Extremely small multimode interference couplers and ultrashort bends on InP by deep etching," *IEEE Photonics Technol. Lett.*, vol. 6, no. 8, pp. 1008–1010, Aug. 1994, doi: 10.1109/68.313078.
[88] E. a. J. Marcatili, "Bends in Optical Dielectric Guides," *Bell Syst. Tech. J.*, vol. 48, no. 7, pp. 2103–2132, 1969, doi: 10.1002/j.1538-7305.1969.tb01167.x.
[89] M. Cherchi, S. Ylinen, M. Harjanne, M. Kapulainen, and T. Aalto, "Dramatic size reduction of waveguide bends on a micron-scale silicon photonic platform," *Opt. Express*, vol. 21, no. 15, pp. 17814–17823, Jul. 2013, doi: 10.1364/OE.21.017814.
[90] "Understanding the mode overlap calculation," *Lumerical Support*. https://support.lumerical.com/hc/en-us/articles/360034396834-Understanding-the-mode-overlap-calculation (accessed Apr. 05, 2022).
[91] F. Ladouceur and E. Labeye, "A new general approach to optical waveguide path design," *J. Light. Technol.*, vol. 13, no. 3, pp. 481–492, Mar. 1995, doi: 10.1109/50.372446.
[92] E. A. J. Marcatili, "Dielectric rectangular waveguide and directional coupler for integrated optics," *Bell Syst. Tech. J.*, vol. 48, no. 7, pp. 2071–2102, Sep. 1969, doi: 10.1002/j.1538-7305.1969.tb01166.x.
[93] M. Bachmann, P. A. Besse, and H. Melchior, "General self-imaging properties in N × N multimode interference couplers including phase relations," *Appl. Opt.*, vol. 33, no. 18, pp. 3905–3911, Jun. 1994, doi: 10.1364/AO.33.003905.
[94] L. B. Soldano and E. C. M. Pennings, "Optical multi-mode interference devices based on self-imaging: principles and applications," *J. Light. Technol.*, vol. 13, no. 4, pp. 615–627, Apr. 1995, doi: 10.1109/50.372474.
[95] O. Schwelb, "Transmission, group delay, and dispersion in single-ring optical resonators and add/drop filters-a tutorial overview," *J. Light. Technol.*, vol. 22, no. 5, pp. 1380–1394, May 2004, doi: 10.1109/JLT.2004.827666.
[96] E. Patzak, A. Sugimura, S. Saito, T. Mukai, and H. Olesen, "Semiconductor laser linewidth in optical feedback configurations," *Electron. Lett.*, vol. 19, no. 24, pp. 1026–1027, Nov. 1983, doi: 10.1049/el:19830695.
[97] B. Liu, A. Shakouri, and J. E. Bowers, "Passive microring-resonator-coupled lasers," *Appl. Phys. Lett.*, vol. 79, no. 22, pp. 3561–3563, Nov. 2001, doi: 10.1063/1.1420585.

[98] T. L. Koch and U. Koren, “Semiconductor lasers for coherent optical fiber communications,” *J. Light. Technol.*, vol. 8, no. 3, pp. 274–293, Mar. 1990, doi: 10.1109/50.50725.
[99] M.-H. Lee *et al.*, “Photonic integrated circuit with sampled grating lasers fabricated on generic foundry platform for broadband terahertz generation,” *Opt. Express*, Mar. 2022, doi: 10.1364/OE.454296.
[100] M.-H. Lee *et al.*, “InP integrated photonic circuit for terahertz spectroscopy up to 4.1 THz bandwidth based on sampled grating lasers,” in *2021 Conference on Lasers and Electro-Optics (CLEO)*, May 2021, pp. 1–2.
[101] S. S. Dhillon *et al.*, “The 2017 terahertz science and technology roadmap,” *J. Phys. Appl. Phys.*, vol. 50, no. 4, p. 043001, Jan. 2017, doi: 10.1088/1361-6463/50/4/043001.
[102] C. Weisenstein, D. Schaar, A. K. Wigger, H. Schäfer-Eberwein, A. K. Bosserhoff, and P. H. Bolívar, “Ultrasensitive THz biosensor for PCR-free cDNA detection based on frequency selective surfaces,” *Biomed. Opt. Express*, vol. 11, no. 1, pp. 448–460, Jan. 2020, doi: 10.1364/BOE.380818.
[103] A. I. McIntosh, B. Yang, S. M. Goldup, M. Watkinson, and R. S. Donnan, “Terahertz spectroscopy : a powerful new tool for the chemical sciences?,” *Chem. Soc. Rev.*, vol. 41, no. 6, pp. 2072–2082, 2012, doi: 10.1039/C1CS15277G.
[104] K. Sengupta, T. Nagatsuma, and D. M. Mittleman, “Terahertz integrated electronic and hybrid electronic–photonic systems,” *Nat. Electron.*, vol. 1, no. 12, pp. 622–635, Dec. 2018, doi: 10.1038/s41928-018-0173-2.
[105] P. u. Jepsen, D. g. Cooke, and M. Koch, “Terahertz spectroscopy and imaging – Modern techniques and applications,” *Laser Photonics Rev.*, vol. 5, no. 1, pp. 124–166, 2011, doi: 10.1002/lpor.201000011.
[106] T. Nagatsuma and G. Carpintero, “Recent Progress and Future Prospect of Photonics-Enabled Terahertz Communications Research,” *IEICE Trans. Electron.*, vol. E98-C, no. 12, pp. 1060–1070, Dec. 2015.
[107] G. Chattopadhyay, “Technology, Capabilities, and Performance of Low Power Terahertz Sources,” *IEEE Trans. Terahertz Sci. Technol.*, vol. 1, no. 1, pp. 33–53, Sep. 2011, doi: 10.1109/TTHZ.2011.2159561.
[108] M.-C. Lo, A. Zarzuelo, R. Guzmán, and G. Carpintero, “Monolithically Integrated Microwave Frequency Synthesizer on InP Generic Foundry Platform,” *J. Light. Technol.*, vol. 36, no. 19, pp. 4626–4632, Oct. 2018.
[109] F. van Dijk *et al.*, “Integrated InP Heterodyne Millimeter Wave Transmitter,” *IEEE Photonics Technol. Lett.*, vol. 26, no. 10, pp. 965–968, May 2014, doi: 10.1109/LPT.2014.2309353.
[110] G. Carpintero *et al.*, “Microwave Photonic Integrated Circuits for Millimeter-Wave Wireless Communications,” *J. Light. Technol.*, vol. 32, no. 20, pp. 3495–3501, Oct. 2014, doi: 10.1109/JLT.2014.2321573.
[111] N. Kim *et al.*, “Distributed feedback laser diode integrated with distributed Bragg reflector for continuous-wave terahertz generation,” *Opt. Express*, vol. 20, no. 16, pp. 17496–17502, Jul. 2012, doi: 10.1364/OE.20.017496.
[112] G. Carpintero, S. Hisatake, D. de Felipe, R. Guzman, T. Nagatsuma, and N. Keil, “Wireless Data Transmission at Terahertz Carrier Waves Generated from a Hybrid InP-Polymer Dual Tunable DBR Laser Photonic Integrated Circuit,” *Sci. Rep.*, vol. 8, no. 1, p. 3018, Feb. 2018, doi: 10.1038/s41598-018-21391-0.
[113] J. Hulme *et al.*, “Fully integrated microwave frequency synthesizer on heterogeneous silicon-III/V,” *Opt. Express*, vol. 25, no. 3, pp. 2422–2431, Feb. 2017, doi: 10.1364/OE.25.002422.

[114] M. Deumer *et al.*, “Continuous wave terahertz receivers with 4.5 THz bandwidth and 112 dB dynamic range,” *Opt. Express*, vol. 29, no. 25, pp. 41819–41826, Dec. 2021, doi: 10.1364/OE.443098.

[115] L. Liebermeister *et al.*, “Optoelectronic frequency-modulated continuous-wave terahertz spectroscopy with 4 THz bandwidth,” *Nat. Commun.*, vol. 12, no. 1, p. 1071, Feb. 2021, doi: 10.1038/s41467-021-21260-x.

[116] “Fraunhofer HHI Delivers InP Foundry Calibrated SOA Compact Model with Ansys Lumerical,” *Lumerical*. https://www.lumerical.com/customer-success/fraunhofer-hhi/ (accessed Feb. 27, 2022).

[117] A. J. Deninger, A. Roggenbuck, S. Schindler, and S. Preu, “2.75 THz tuning with a triple-DFB laser system at 1550 nm and InGaAs photomixers,” *J. Infrared Millim. Terahertz Waves*, vol. 36, no. 3, pp. 269–277, Mar. 2015, doi: 10.1007/s10762-014-0125-5.

[118] M. Naftaly, N. Vieweg, and A. Deninger, “Industrial Applications of Terahertz Sensing: State of Play,” *Sensors*, vol. 19, no. 19, Art. no. 19, Jan. 2019, doi: 10.3390/s19194203.

[119] S. Nellen *et al.*, “Experimental Comparison of UTC- and PIN-Photodiodes for Continuous-Wave Terahertz Generation,” *J. Infrared Millim. Terahertz Waves*, vol. 41, no. 4, pp. 343–354, Apr. 2020, doi: 10.1007/s10762-019-00638-5.

[120] S. Nellen *et al.*, “Radiation pattern of planar optoelectronic antennas for broadband continuous-wave terahertz emission,” *Opt. Express*, vol. 29, no. 6, pp. 8244–8257, Mar. 2021, doi: 10.1364/OE.416844.

[121] M. MÖHRLE and M.-H. Lee, “Thermally tunable laser and method for fabricating such laser,” EP3565068A1, Nov. 06, 2019 Accessed: Apr. 29, 2022. [Online]. Available: https://patents.google.com/patent/EP3565068A1/en?inventor=moon-hyeok+lee&oq=moon-hyeok+lee